1-1-2020

Nondestructive Evaluation Of Solid Cargo Inside Cylindrical Containers By Using Linear And Nonlinear Acoustic Resonance Spectroscopy

Kevin Yi-Wei Lin

NONDESTRUCTIVE EVALUATION OF SOLID CARGO INSIDE CYLINDRICAL CONTAINERS BY USING LINEAR AND NONLINEAR ACOUSTIC RESONANCE SPECTROSCOPY

A dissertation
presented in partial fulfillment of requirements
for the degree of Doctor of Philosophy
in the Department of Physics and Astronomy
The University of Mississippi

by

Kevin Yi-Wei Lin

May 2020

ABSTRACT

The Nondestructive Evaluation (NDE) of cylindrical containers is of critical importance because of their ubiquity in industrial applications. However, there is a paucity of research in the literature on NDE studies of solid cargo inside cylindrical containers. This dissertation consists of three connected projects investigating the application of linear and nonlinear Acoustic Resonance Spectroscopy (ARS) to the NDE of solid cargo inside sealed cylindrical containers. In these projects, the container of interest varied from extremely complicated to very simplified, and the studies extended from applied to basic physics problems. The first study was focused on an empty Transnuclear-32 (TN-32) nuclear cask for spent fuel (5.1 m in height and 2.5 m in diameter), the vibrational modes were measured and compared to Finite Element Analysis (FEA) of a TN-32 cask. The modal structural changes due to various loadings of spent fuel were also investigated through FEA. Because of the practical difficulties of introducing damage on the spent fuel inside a full-scale TN-32 cask, a 1:6 scaled lab cask was manufactured. First, modes of the lab cask were measured, simulated, and compared to the TN-32 cask. Second, ARS measurements were conducted on the lab cask with various configurations of mock-up fuel assemblies, debris, and empty state in each of the 32 basket slots. The integrity of the mock-up fuel assemblies can be estimated by the metrics developed in this work. However, the signatures of a damaged versus missing assembly were not clearly resolved. To further improve the sensitivity, Nonlinear ARS (NARS) was used to investigate the contact nonlinearity between the debris and the container. A 20 cm-tall cylinder loaded with various types of spheres was used as a simplified experimental

model. The NARS results showed unique characteristics than that has been reported in the literature. The experimental results were successfully modeled with a contact loss phenomenological model, which was then implemented in FEA. NARS was able to estimate the total mass of the spheres regardless of the material and radius. In summary, this dissertation demonstrates the feasibility of applying ARS and NARS on the NDE of solid cargo inside cylindrical containers.

DEDICATION

To my caring mother Shu-Mei Liang (梁淑玫)

LIST OF ABBREVIATIONS AND SYMBOLS

ABBREVIATIONS

ARS	Acoustic Resonance Spectroscopy
CAD	computer aided design
CAN	Contact Acoustic Nonlinearity
CW	continuous wave
FEA	Finite Element analysis
FFT	Fast Fourier Transform
LDV	laser Doppler vibrometer
NARS	Nonlinear ARS
NDE	nondestructive evaluation
NME	Nonlinear Mesoscopic Elasticity
NRC	Nuclear Regulatory Commission
NRUS	Nonlinear Resonance Ultrasound Spectroscopy
PCA	principle component analysis
S/N	signal-to-noise ratio
SNF	spent nuclear fuel
SSC	stress corrosion cracking
TN-32	Transnuclear-32

SYMBOLS

A	displacement amplitude
A_c	critical displacement amplitude for contact loss at the contact boundary
A_c^{top}	effective critical displacement for contact loss at the top surface of the container
M	total mass of the spheres
E^*	contact modulus
$\{F_m\}$	Taylor expansion coefficients for the contact force
$f^{\mathrm{NL}}(u)$	nonlinear contact force as a function of displacement
$\widetilde{f^{\mathrm{H}}}(\tilde{u})$	total Hertzian force
N	total number of spheres
Q	quality factor
R^*	reduced radius of curvature
R_s	radius of the sphere
S	contact boundary surface area
f	frequency
u	dynamic displacement
u_0	equilibrium displacement
$\tilde{u}$	total displacement

$z_n(t)$	temporal function of the n^{th} mode
α	hysteretic parameter
β, δ	the second and third order nonlinear parameters in the classical nonlinear stress-strain relation
γ	constant of proportionality for contact loss
$\varepsilon = \partial_x u$	strain
η	isotropic loss factor
ν	Poisson's ratio
ρ	density
σ	stress
$\sigma^{\mathrm{NC}}(\varepsilon, \dot{\varepsilon})$	non-classical stress-strain relation
$\psi_n(x)$	mode shape function of the n^{th} mode
ω_n	unperturbed resonance frequency of the n^{th} mode
Ω_n	perturbed resonance frequency of the n^{th} mode
Ω_n^{C}	perturbed resonance frequency of the n^{th} mode for contact loss

ACKNOWLEDGEMENTS

I'm grateful for all the people who have helped me along this amazing journey toward my PhD. First, I would like to thank my research advisor Dr. Joel Mobley who provides me the opportunities to be involved in various research projects and the freedom to pursue my research. I would also like to thank Dr. Wayne Prather for many crucial technical supports and discussions. A fair number of projects would not have been possible without Dr. Josh Gladden's leadership. I want to thank Dr. Zhiqu Lu for introducing me to nonlinear vibration, and Dr. Likun Zhang and Dr. Garth Frazier for not only serving as committee members but also many meaningful discussions.

Research could be much more difficult without the support from the National Center for Physical Acoustics. I'm thankful for the leadership from Dr. Josh Gladden and Dr. Craig Hickey, and the expertise from the staff, including Mrs. Sara Brown, Mr. John Anderson, Mrs. Debra Bos, Mrs. Latonya Weekly and Mrs. Marta Panickar. Mr. Paul Dakin and Mr. Ronnie Oswalt's assistance on constructions is very crucial. I'd like to thank the Department of Physics and Astronomy for the academic support, especially Dr. Luca Bombelli, Dr. Kevin Beach and Mr. Thomas Jamerson.

I would not have made it through without the emotional support from my sister and father, Peggy Lin and Foster Lin, and members of Taiwanese Student Association. I appreciate Dr. Adam Estes and Dr. Michael Worthy for the chance to keep playing in the jazz band. I enjoy the comradeship with Jonathan Herlan, Ashoka Karunarathne, Keegan Kurpakus, and all other fellow grads. I'm also very lucky to meet Yue-Jia Lee. Her support helped me through the hardest times.

TABLE OF CONTENTS

LIST OF TABLES

LIST OF FIGURES

1. BACKGROUND

As a child, I had the luxury of receiving Christmas presents from my parents. Impatient as I was, I always tried to guess what was inside the present box before I can open it on Christmas day. One thing I usually did was to shake the box. I tried to feel and listen to the vibration coming from the contents inside the box. Sometimes, I could have a pretty good guess of the size and shape of the present. Unknowingly, I was performing a type of acoustic Nondestructive Evaluation (NDE) on the contents of an enclosed box. It turns out later in my graduate research that the acoustic NDE of solid contents inside a sealed vessel, similar to my Christmas present problem, is still an important and growing field that requires further research. The aim of this dissertation is to contribute to this field of study from both applied and basic physics perspectives.

1.1. ACOUSTIC RESONANCE IN NONDESTRUCTIVE EVALUATION

The ability to identify damage non-invasively in the early stage of formation is of interest throughout civil, mechanical, aerospace engineering, and is especially critical in the nuclear power industry. An interdisciplinary field of study called Nondestructive Evaluation (NDE), or Nondestructive Testing (NDT), is dedicated to this effort. The American Society of Nondestructive Testing (ASNT) [1] defines NDE as “the process of inspecting, testing, or evaluating materials, components or assemblies for discontinuities, or differences in characteristics without destroying the serviceability of the part or system.” Traditional NDE methods involve either visual or localized inspections that use modalities such as ultrasound, magnetic fields, radiographs, eddy-

currents and thermal imaging. These methods all require *a prior* knowledge of the vicinity of the damage and direct accessibility to that area. These limitations precipitated the development of global examination methods by using linear acoustic resonance in the 1970s. Since resonance is a global behavior, the inaccessible components and inner structures will impact the vibrational response of the accessible exterior. These methods mainly focus on the change of modal structure, including resonant frequency, quality factor and mode shapes. Extensive and intensive studies of these techniques can be readily found in the literature [2–4]. Acoustic resonance NDE has been applied to various geometries, including plates, beams, trusses, shells, frames, bridges, offshore platforms, among others [2,5–7].

Of these structures, cylindrical containers are crucial due to their ubiquitous usage in storage applications. Some related lab studies on steel cylinders are listed below. In a carbon steel cylindrical shell, mode shapes were found to be more sensitive than changes of resonance frequencies to cracks on the shell [8]. A resonance frequency shift curve method was shown to locate the damage caused by an auxiliary mass attached externally on a steel cylindrical shell [9]. Liquid filled cylindrical containers have been studied. The resonance frequencies and modal shapes of a geometrically imperfect steel tank, under both water-filled and empty scenarios, have shown good agreement between large-amplitude theory and experiments [10]. Another example of this line of inquiry in the seismic community is the evaluation of vibrational interaction between the tank and the sloshing fluid inside [11–16].

However, vibrational or NDE studies on the solid materials loaded in cylindrical containers are rarely found in the literature. This dissertation aims to fill this gap by applying Acoustic Resonance Spectroscopy (ARS) [17], known as vibrational spectroscopy, to this type of systems.

ARS is capable of extracting material information from an enclosed structure. An early effort in the literature started from fluid chemical classification inside munitions by utilizing a database [18] for blind discrimination of liquid- and solid-filled munitions [19]. Subsequently, an ultrasonic interferometry technique was developed on containers of more general properties. This technique can noninvasively identify different fluid chemicals inside a rectangular glass cell and a cylindrical stainless-steel cell [20]. To extend the ARS work to the NDE of the solid cargo in cylindrical containers, in Chapter 2 of this dissertation, resonance modes were first identified to evaluate the feasibility of ARS on a full-scale Transnuclear-32 dry storage cask for spent fuel. In Chapter 3, vibrational metrics based on ARS were then developed for the NDE of mock-up fuel assemblies inside the lab-scale cask.

Nevertheless, it has been shown in the literature that linear resonance techniques (e.g. ARS) are not sensitive enough to extract sufficient information on smaller defects or interfaces for NDE purposes. Nonlinear aspects of acoustic NDE were initiated in 1980s. Nonlinear acoustic techniques were shown to be sensitive to interfaces [21,22] and the early stage of crack formation, including micro-cracks in concrete [23] and fatigue damage in metal [24] and bone [25]. The nonlinear acoustic techniques have been reviewed [26,27] in which several categories are listed here: higher (second [28]) harmonic generation, sub-harmonic generation, shift of resonance frequency/Nonlinear Ultrasound Resonant Spectroscopy (NRUS) [29], and mixed frequency response/Nonlinear Wave Modulation Spectroscopy [30]. Theoretical modelling of the above nonlinear techniques and the ultrasonic interactions with nonlinear cracks were reviewed by Broda *et al* [31].

Among these techniques, NRUS shares many commonalities with ARS. The nonlinearity inside a sample can be quantified by observing the resonance frequency shift of a mode while the sample is being driven at various amplitudes. NRUS has been used to quantify the nonlinearity caused by damage inside various samples, including cement slate [32], alkali-silica reaction damaged cement bar [33], carbon fiber reinforced plastics [34], thermal damaged concrete [23] and glass [35], cortical bone [25,36–38], stress corrosion cracking in stainless steel rods [39], and so on. The frequency shifts in the harmonics were also studied on micro-cracked glass and composites made of steel-titanium carbide or polymer [40]. There were also theoretical [41,42] and experimental [43,44] efforts on locating the source of defects with multi-mode NRUS. This can be achieved because the modes with defects located at their anti-nodes will exhibit higher nonlinearity. From another perspective, with proper choice of modes, the nonlinearity inside the system can be probed locally.

Since the application of NRUS in this dissertation is similar to the historical developments of ARS (i.e. evaluating the cargo using resonance in the audible frequency), this dissertation will refer to this particular use of NRUS as Nonlinear Acoustic Resonance Spectroscopy (NARS). It is expected that NARS can provide complementary information in addition to ARS on the contact interactions between the solid cargo and its container. In Chapter 4, this idea was pursued by studying the contact nonlinearity between a layer of spheres and its cylindrical container with NARS. Details on ARS and NARS will be presented in the next section.

1.2. LINEAR AND NONLINEAR ACOUSTIC RESONANCE SPECTROSCOPY

In this section, the basic ideas of ARS and NARS will be presented both in a simplified theoretical model and in a basic experimental setup. A 1-D longitudinally driven bar under free boundary condition [Figure 1.2.1] will be used to demonstrate the theoretical foundation of ARS and NARS. The stress-strain relation in this system is assumed to have this form:

$$\sigma = K(1 + \beta\varepsilon + \delta\varepsilon^2 + \cdots)\varepsilon + \sigma^{\mathrm{NC}}(\varepsilon, \dot{\varepsilon}) \tag{1.2.1}$$

where σ is the stress, $\varepsilon = \partial_x u$ is the strain, $u(x,t)$ is the displacement, K is the relevant linear elastic constant (e.g. Young's modulus for longitudinal strains in isotropic rods). The higher order terms in the expansion on the right-hand side represents the atomic anharmonicity of the material, and is labeled as "classical" nonlinearity, where β and δ are the second and third order nonlinear parameters. The $\sigma^{\mathrm{NC}}(\varepsilon, \dot{\varepsilon})$ term is a general expression on "non-classical" nonlinearity. It is model dependent and can be a function of the strain rate and even may have hysteretic features [45]. The equation of motion in this system can be written as:

$$\rho\partial_{tt}u = \partial_x\sigma - \rho\frac{\Omega}{Q}\partial_t u + F\delta(x) \tag{1.2.2}$$

where Ω is the driven angular frequency of the system, and Q is the quality factor of the mode. $\delta(x)$ is the Dirac delta function that imposes the driving force per unit area $F = A\cos(\Omega t)$ at the $x = 0$ surface with A as the excitation amplitude.

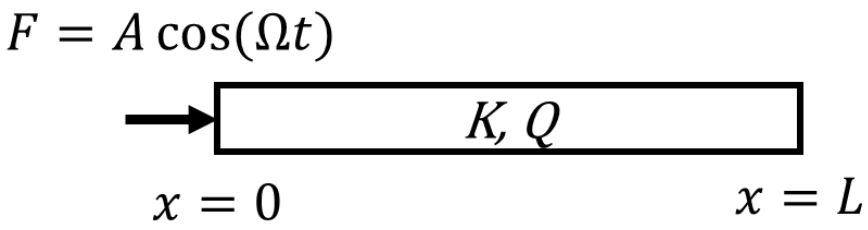

Figure 1.2.1. A 1-D longitudinal driven bar for demonstrating the basics of ARS.

Starting with the linear case ($\sigma^{\mathrm{NC}}(\varepsilon, \dot{\varepsilon}) = 0, \beta = \delta = 0$), $u(x,t)$ can be written as the summation of all the normal modes by using separation of variables:

$$u(x,t) = \sum_{j=1}^{\infty} \psi_j(x) z_j(t) \tag{1.2.3}$$

where $\psi_j(x) = \cos\left(\frac{n\pi x}{L}\right)$ and $z_j(t)$ are the mode shape and the temporal functions of the j^{th} mode respectively. Here the mode shape of the free-free boundary condition is used because the driving force is treated in the temporal part of the equation. With the orthogonality of the mode shape functions, the n^{th} mode can be picked out by multiplying the n^{th} mode shape function on both sides of the equation and integrating over the length of the bar L:

$$\partial_{tt} z_n = -{\omega_n}^2 z_n - \frac{\Omega}{Q} \partial_t z_n + \frac{2f}{L\rho} \tag{1.2.4}$$

where $\omega_n = \frac{n\pi}{L}\sqrt{\frac{K}{\rho}}$ is the natural frequency of the n^{th} mode. This equation has a solution in the following form:

$$z_n = A_n \cos(\Omega t + \phi_n) \tag{1.2.5}$$

$$A_n = \frac{2f}{L\rho} \sqrt{(\Omega^2 - {\omega_n}^2)^2 + (\Omega^2/Q)^2} \tag{1.2.6}$$

$$\tan \phi_n = -\frac{\Omega^2}{Q(\Omega^2 - {\omega_n}^2)} \tag{1.2.7}$$

Solving $\frac{dA_n}{d\Omega} = 0$ gives the resonance frequency Ω_{res}:

$$\Omega_{\mathrm{res}} = \frac{\omega_n}{\sqrt{1 + \frac{1}{Q^2}}} \tag{1.2.8}$$

By measuring the resonance frequencies and their associated quality factors of a system, information on how much the elastic properties and the attenuation have changed from a baseline can be extracted. By measuring the mode shapes, the changes in geometry and boundary condition can be acquired. All the above factors are related to the integrity of a structure and thus can be used for NDE purposes. For a full 3-D application, especially for the complexity of loaded containers, numerical methods are required for these inverse problems. Finite Element Analysis (FEA) is a matured tool for this purpose and is widely used in both academia and industry.

However, ARS has its limitation on detecting relatively small defects or interfaces. Fortunately, the nonlinear version of ARS has the potential to complement ARS in this area. Historically, NRUS/NARS was developed in the course of studying nonlinear mesoscopic elasticity (NME) in materials, like limestone, sandstone, marble and chalk [46]. This type of materials consists of multi-scale granules and exhibits hysteretic non-classical nonlinearity. The theoretical model of NME involves the use of Preisach-Mayergoyz space [47]. An approximated stress-strain relation for hysteretic nonlinearity can be written as:

$$\sigma^{\mathrm{hy}}(\varepsilon, \dot{\varepsilon}) = K\frac{\alpha}{2}[\mathrm{sign}(\partial_t \varepsilon)((\Delta\varepsilon)^2 - \varepsilon^2) - 2(\Delta\varepsilon)\varepsilon] \tag{1.2.9}$$

where α is the hysteretic parameter, and $\Delta\varepsilon$ is the local strain amplitude over the previous period ($\Delta\varepsilon = (\varepsilon_{max} - \varepsilon_{min})/2$ for a simple continuous sine excitation). It was later shown that α increases when a crack appears in a cement beam, and thus the approach was proved to be a viable NDE tool [32]. A 1-D theoretical model of NRUS on hysteretic nonlinearity can be developed similarly as ARS by plugging equation (1.2.9) into (1.2.5) as $\sigma^{\mathrm{NC}}(\varepsilon, \dot{\varepsilon})$. Detailed

derivation of NARS results with hysteretic and classical cubic nonlinearity can be found in this reference [41]. The results for hysteretic nonlinearity agreed with experiments in which the resonance frequency shift is almost a linear function of driving amplitude and the odd harmonics are predominant. Although not explicitly stated in the paper, this general formulation also suggested that NARS can be potentially applied to other types of nonlinearity. It may be possible to distinguish types of nonlinearity from the shape of the frequency shift versus amplitude curve. This idea is further explored in Chapter 4.

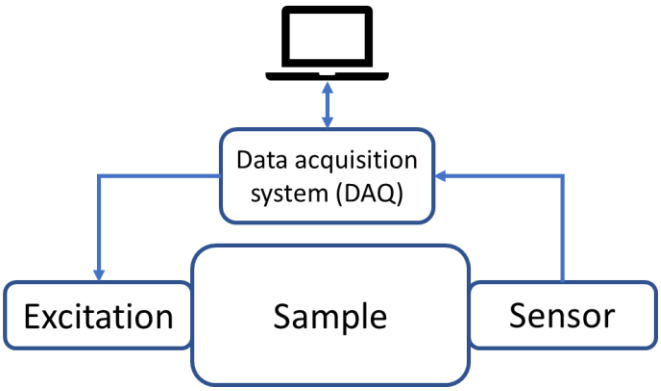

Figure 1.2.2. Basic setup for ARS/NARS study

An experimental setup of ARS and NARS can be very similar. A basic setup is sketched in Figure 1.2.2. The typical excitation source is a mechanical shaker, and an accelerometer or a laser Doppler vibrometers (LDV) can be used as a sensor. The data acquisition system can simply be a waveform recorder or preferably a lock-in amplifier for noise rejection. The excitation source couples a continuous sinusoidal wave into the sample whosefrequency is increased incrementally. Data collected by the sensor is analyzed by performing Fast Fourier Transforms (FFT) of the time-domain responses at each frequency step from which the linear frequency responses (amplitude

and phase) and higher harmonics are obtained [Figure 1.2.3]. A lock-in amplifier obtains the same results with better signal-to-noise ratio (S/N) by applying a low-pass filter after convolution operations between the measured and reference waveforms [48]. The resonance frequencies and associated quality factors are obtained by fitting the peaks in the linear spectrum with Lorentzian functions. For ARS, the resonance frequency and its associated quality factor from each mode are compared with baseline measurements or FEA.

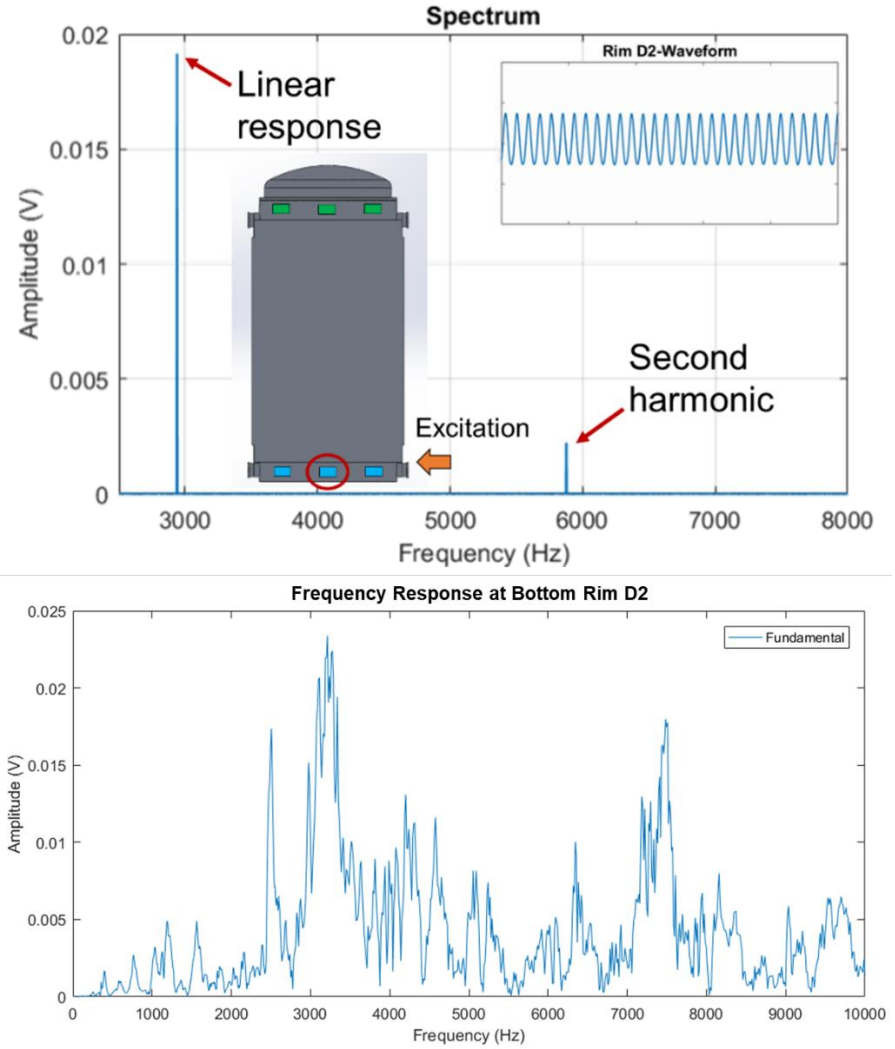

Figure 1.2.3. Example of obtaining frequency response by using ARS on a Transnuclear-32 nuclear cask. An accelerometer is located at the circled position on the cask. (top) The frequency spectra at a single frequency step. (bottom) The fundamental frequency response resulting from the frequency sweep.

For NARS, the sample is further driven with various excitation amplitudes. The resonance frequency shifts when the excitation strain is gradually increased in the strain range from 10^{-7} to 10^{-6}. For hysteretic non-classical nonlinearity [32],

$$\frac{f - f_0}{f_0} \propto \alpha\varepsilon \tag{1.2.10}$$

where f_0 is the linear resonant frequency (at the minimum practical excitation level), and f is the shifted resonant frequency due to higher strain. One of the goals of this dissertation is to show that this relation may not be linear for other types of nonlinearity. Regarding locating the region of nonlinearity in a sample, the coincidence of an anti-node and a localized nonlinearity will exhibit higher α (i.e larger frequency shift) [Figure 1.2.4]. Thus, the region of nonlinearity can be located by measuring multiple modes with NARS and comparing the mode shapes in which large frequency shifts are observed. For the goal of this dissertation, it is expected to attain higher NDE sensitivity by choosing an appropriate mode with large response at the contact surface between the cargo and the container.

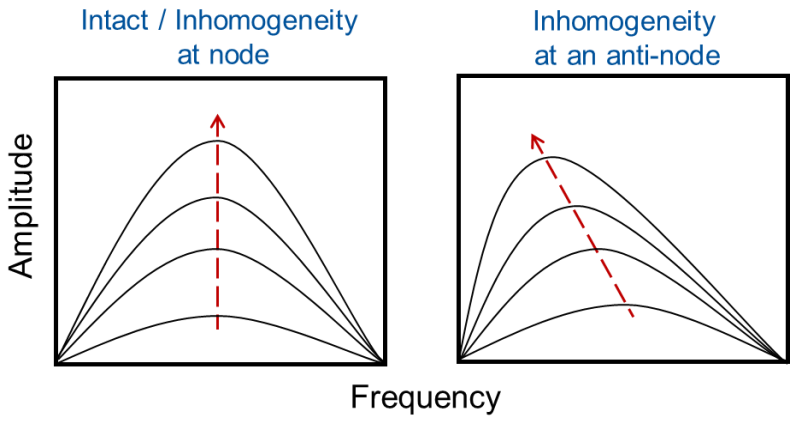

Figure 1.2.4. In NARS, different modes are sensitive to different locations in the sample. If the region of nonlinearity is at a node, minimum frequency shift will be measured. However, if it is at an anti-node, significant frequency shift will be measured.

1.3. CONTACT NONLINEARITY MODELS

Modeling of different types of crack/contact nonlinearity has been a difficult long-term task. Broda [31] has reviewed the models on crack-wave interaction based on ultrasound. In this dissertation, NARS is applied on the NDE of solid cargo inside a container. The decayed cargo in the container was modeled as identical spheres experimentally. The two types of contact nonlinearities that are relevant and will be investigated by using NARS are Bi-linear Stiffness and Hertzian Contact.

1.3.1. BI-LINEAR STIFFNESS

One of the most popular models for cracks, or unbonded surface contacts, is the bi-linear stiffness, also known as stiffness asymmetry. The assumption is that under tension and compression, the crack opens and closes. This is called a *breathing crack* or a *clapping mechanism.* When the crack is closed, the global stiffness is unaffected and when open the global stiffness is reduced. Solodov [49] proposed a model based on this assumption and coined the name *Contact Acoustic Nonlinearity* (CAN). The piece-wise stress-strain relation of CAN is written as:

$$\sigma^{\mathrm{CAN}} = K\,[1 - H(\varepsilon - \varepsilon_0)\frac{\Delta K}{K}\,]\varepsilon \qquad (1.3.1.1)$$

where $\Delta K = \left[K - \left(\frac{\partial \sigma}{\partial \varepsilon}\right)_{\varepsilon>0}\right]$, $H(\varepsilon)$ is the Heaviside step function, and ε_0 is the equilibrium contact strain. In compression ($\varepsilon < \varepsilon_0$), the linear elastic constant is restored. A sketch of this nonlinear stress-strain relation is plotted in Figure 1.3.1.1.

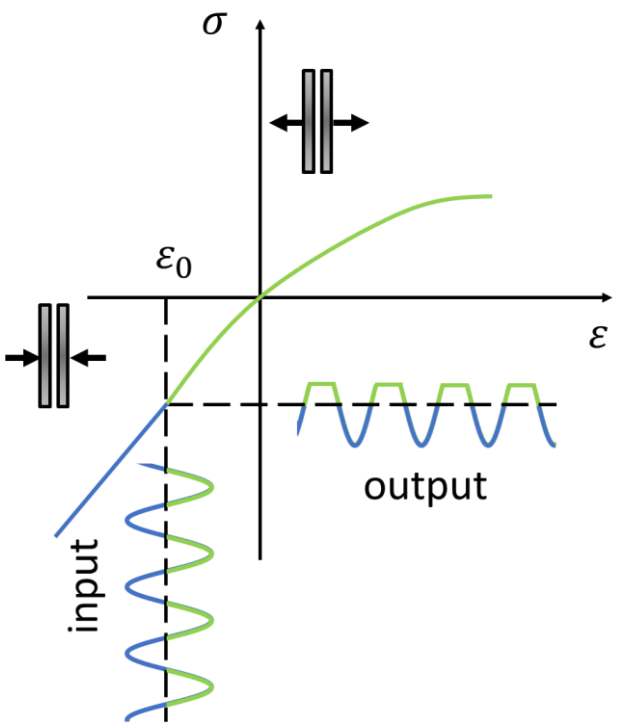

Figure 1.3.1.1. "Mechanical-diode" effect resulted from the piece-wise stress-strain relation of Contact Acoustic Nonlinearity (CAN). ε_0 is the equilibrium contact strain.

In the same paper, experiments were performed on a sample of glass and silicon interface using ultrasound at 25 kHz. The contact was optically polished. Right above a threshold excitation strain ($\varepsilon > \varepsilon_0$), the amplitude of 2nd to 4th harmonics are all found to follow a power law of the fundamental amplitude with an exponent of 1.3 ± 0.3. A threshold phenomenon due to the applied contact pressure was observed in an earlier paper on aluminum-aluminum contact [22]. With the increase of applied pressure ($\varepsilon_0 \uparrow$), the 2nd harmonic decreases eventually reaches a constant, where the strain is not large enough to induce CAN. It's noteworthy that filling the interfaces with glycerin eliminates the threshold effect. With glycerin present in the interface, the 2nd harmonic remains low even when the applied pressure is low ($\varepsilon_0 \downarrow$). This is likely due to the glycerin interfering with the closing of the contact. Besides harmonic generation, CAN may also be used to explain vibro-modulation phenomenon [50]. This dissertation will use the a single-

mode approximation of CAN [51] to model contact loss at the surface between the cargo and the container. This approximation has the following form:

$$\sigma^{\mathrm{CAN}} = \begin{cases} K\varepsilon & \text{when } \varepsilon > \varepsilon_0 \\ K'\varepsilon & \text{when } \varepsilon \leq \varepsilon_0 \end{cases} \tag{1.3.1.2}$$

where K and K' are elastic constants with different values.

1.3.2. HERTZIAN CONTACT

The Hertzian model describes the contact between two elastic, frictionless spheres [Figure 1.3.2.1]. It is also often used to describe the contact of rough surfaces. The Hertzian force law between two spheres of radius R_1 and R_2 is [52]:

$$\widetilde{f^{\mathrm{H}}} = -\frac{4E^*\sqrt{R^*}}{3}\tilde{u}^{\frac{3}{2}} \tag{1.3.2.1}$$

where $\widetilde{f^{\mathrm{H}}}$ is the total Hertzian force, $\tilde{u}$ is the total displacement, E^* is the contact modulus and R^* is the reduced radius of curvature. The latter two quantities are related to the physical properties of the two spheres:

$$\frac{1}{E^*} = \frac{1-{\nu_1}^2}{E_1} + \frac{1-{\nu_2}^2}{E_2} \tag{1.3.2.2}$$

$$\frac{1}{R^*} = \frac{1}{R_1} + \frac{1}{R_2} \tag{1.3.2.3}$$

With $E_1$and E_2 are the Young's modulus of the individual spheres, and ν_1 and ν_2 are the Poisson's ratios.

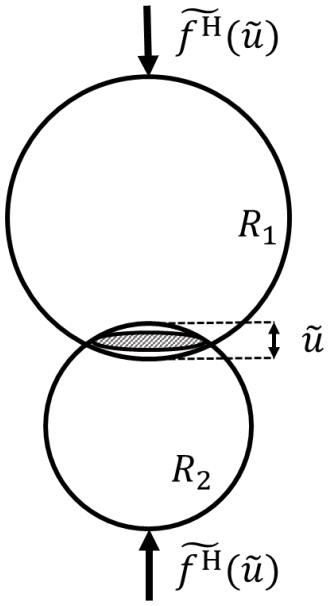

Figure 1.3.2.1. An illustration of the Hertzian contact between two spheres.

Some previous works on Hertzian contact are summarized below. Contact of nominally flat surfaces can be modeled as numerous small Hertzian contacts [53]. NRUS was applied to screw tightness-of-fit on an aluminum plate, and the coexistence of hysteretic and Hertzian contacts were suggested [54]. Changes in resonance properties due to various degree of glass bead compaction were studied [55]. A model of packed granular media (identical and spherical) was proposed by Belyaeva *et al* [56]. The stress-strain relation of cubic-packed elastic spheres is:

$$\sigma^{\mathrm{H}} = \frac{n(1-\zeta)E_s}{3\pi(1-\nu_s^2)}\varepsilon^{3/2} \tag{1.3.2.4}$$

where n is the average number of contacts per spherical particle, ζ is the packing porosity coefficient, and E_s, υ_s are the material's Young's modulus and Poisson coefficient, respectively. The derived power law for 2nd and 3rd harmonic generation are quadratic and cubic of the fundamental amplitude, respectively. In the following papers, experiments were performed on cubic [57] and non-ideal [58] packing of lead shot and plastic granules in a metallic cylindrical cup.

The shot in the cup was vibrated with direct contact to a piston. The power law of 2nd harmonics agrees with theory in both packing conditions, while the power law of 3rd harmonics does not agree with the theory under non-ideal packing. The 3rd harmonic for lead shot under non-ideal packing exhibits quadratic dependence while plastic granules exhibit a transition from cubic for small oscillations to quadratic at large amplitudes. The authors suspected that the deviation from theory is a result of competition between Hertzian and CAN mechanisms. Furthermore, a generalized Hertzian model, proposed by Sun *et al* [59], states that the stress-strain power law depends on the shape of the granules. This provides a theoretical foundation for determining the shape of granules using nonlinear techniques. In this dissertation, the decayed debris is modeled as identical spheres in experiments, and thus a sphere-plane Hertzian contact model is relevant. In related past efforts, resonance frequency shifts with Duffing-type jump phenomenon were observed in a single plane-sphere-plane contact excited by a normal load [60], and significant softening and noise caused by loss of contact were observed at a higher amplitude under a similar setup [61].

To emphasize the physics of interest, the stress-strain relations and the power law exponents of the harmonics for hysteretic, Hertzian and CAN model are summarized in Table 1.3.2.1. The Hertzian and CAN models will be investigated in this dissertation using the NRUS/NARS formalism [41]. The frequency shift power law dependences for both models will be derived theoretically and measured experimentally.

Table 1.3.2.1. Summary of the four types of nonlinearity discussed in text. The last two columns are the power law exponents for the amplitudes of 2nd and 3rd harmonics with respect to the fundamental amplitude.

Nonlinearity type	Stress-strain relation	2nd harmonic	3rd harmonic
Classical	$\sigma^{\mathrm{C}} = K(1 + \beta\varepsilon + \delta\varepsilon^2 + \cdots)\varepsilon$	Not generated	3
Hysteretic	$\sigma^{\mathrm{hy}} = K\frac{\alpha}{2}[\mathrm{sign}(\partial_t\varepsilon)((\Delta\varepsilon)^2 - \varepsilon^2) - 2(\Delta\varepsilon)\varepsilon]$	Not generated	2
Contact Acoustic Nonlinearity	$\sigma^{\mathrm{CAN}} = K\{1 - H(\varepsilon - \varepsilon_0)\frac{\Delta K}{K}\}\varepsilon$	~1.5	~1.5
Hertzian contact	$\sigma^{\mathrm{H}} = \frac{n(1-\zeta)E_s}{3\pi(1-\nu_s^2)}\varepsilon^{3/2}$	2	3

The following chapters cover three related projects on the NDE of solid cargo inside a cylindrical container. In Chapter 2, the feasibility of using ARS for the NDE of spent fuel assemblies inside a full-scale Transnuclear-32 dry storage cask is evaluated through vibration mode measurements and FEA. In Chapter 3, an NDE methodology based on ARS was developed for mock-up fuel assemblies inside a lab-scale dry storage cask. In Chapter 4, to further improve the sensitivity to detect debris, NARS was used to study the contact nonlinearity at the surface between a simple cylindrical container and spheres (to model debris) contained within. A dissertation conclusion is found in Chapter 5.

2. CHARACTERIZATION OF A FULL-SCALE TRANSNUCLEAR-32 DRY STORAGE CASK FOR SPENT NUCLEAR FUEL[1]

2.1. ACTIVE ACOUSTIC METHODS FOR NDE OF NUCLEAR DRY STORAGE CASKS

In the commercial nuclear power industry in the United States, dry storage casks are used to accommodate long-cooled dry spent nuclear fuel. With the cancelation of the Yucca Mountain Repository in 2010, the licenses of these dry casks must be extended for prolonged storage before the final relocation plan is agreed upon [62]. The Nuclear Regulatory Commission (NRC) has been looking into various NDE approaches to assess the long-term integrity of a variety of storage casks including CASTOR V/21 [63,64] as well as other models [64,65]. These NDE efforts include visual inspection, eddy current measurements, temperature monitoring, gamma ray scanning, and ultrasonic techniques. The limitation of these methods lies in the difficulty of extracting information from the interior of the casks, especially regarding the spent fuel. One of the central concerns about extended storage is that the spent fuel must remain below nuclear criticality during the relocation process after being loaded for more than a century. In a dry storage cask, subcriticality is maintained by suitable burnup credit, neutron absorbers, moderator exclusion, basket spacing and fuel configuration [66], with the last two factors being the focus of this chapter. The vibrational characterization described in this chapter is part of a collaborative effort to combine various radiological and non-radiological techniques to identify

[1] This chapter was published in Journal of Sound and Vibration [100].

catastrophic failures in the basket and fuel rod assemblies inside a specific cask type, the Transnuclear-32 (TN-32) [Figure 2.1.1]. The ultimate goal is to provide a set of tools for examining the basket and spent fuel in dry storage casks in order to detect potential criticality hazards during relocation and long-term storage.

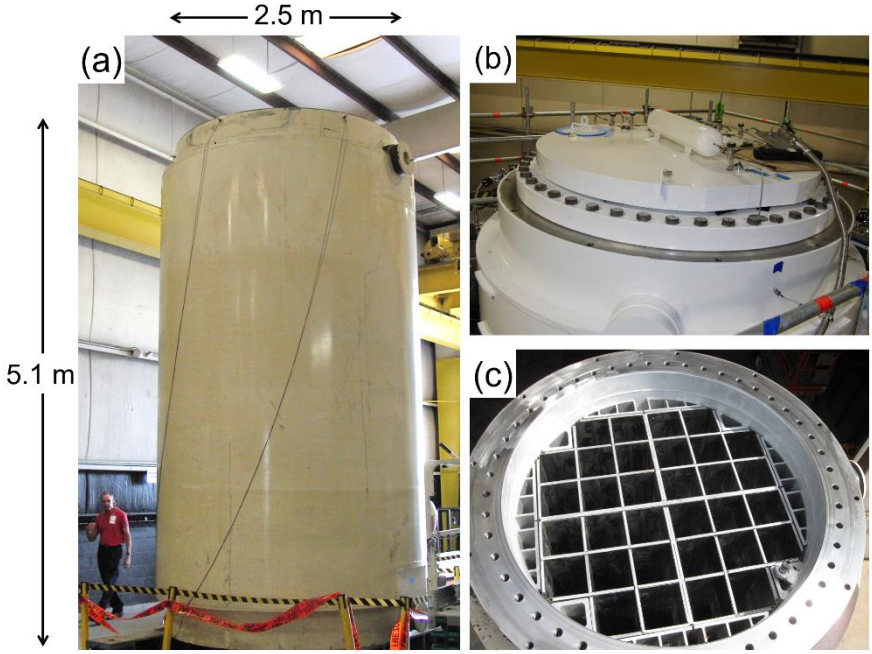

Figure 2.1.1. The Transnuclear-32 (TN-32) dry storage cask studied in this chapter. (a) Side view when the dome and the lid were removed. (b) View with the lid on when the dome was removed. (c) Top view of the basket in the cask.

In recent years, several active acoustic methods have been applied to the characterization of nuclear fuel storage vessels. Concrete has been one of the primary concerns due to its common usage in the pedestal and the biological shield walls of nuclear power plants and storage casks. Residual radiation damage in concrete is often studied in this context and is detectable using NRUS [23]. Another prevailing damage mechanism, the alkali-silica reaction, has been detected using second harmonic generation of Rayleigh waves in a reinforced concrete specimen which simulates conditions in nuclear power plants [67]. Another primary concern is the steel used for

the inner canister inside storage casks, which also constitutes most of the containing vessel for TN-32. Damage scenarios of steel that can be found in the nuclear energy industry have also been investigated. Second harmonic generation was applied to steel charpy samples simulating reactor pressure vessels under various levels of neutron damage [68] and annealing [69]. Stress corrosion cracking (SCC) on the inner steel canister of a storage cask [70] can be detected with Rayleigh waves by using electromagnetic ultrasonic transducers delivered with robotics [71–74], and also located with time-reversal and NRUS techniques [39,75–78]. Along with the mentioned work above, there have been some acoustic studies on commercially available dry storage casks. Ultrasonic tomography has been used to examine the welds in a dry storage cask (Patent RU 2500045) [79]. Ultrasound guided waves were utilized through acoustic emission and active propagation on the outer steel shell of a TN-32 cask [80]. However, studies evaluating the state of the internal structure of an enclosed cylinder using global acoustic/vibrational resonance are lacking.

In contrast to earlier work, this study is not concerned with the state of the containing vessel but in assessing the state of the cargo contained therein using only measurements made on the surface of the cask. With respect to the cargo of dry storage casks, the vibrational properties of fuel rod assemblies have been studied since the 1970s. However, most were studied in the context of fluid-structure interaction inside the power plant [81], while some others focused on the interaction with the supporting grid [82,83]. For fluid cargo, a tone-burst technique was proposed as a safeguard for fluid-based nuclear containers [84]. Instead, this work is concerned with cargo consisting of highly engineered solid structures which can exhibit complex vibrational characteristics. To the author's knowledge there was no previous reported

study on the integrity of such cargo in an enclosed cylinder through vibrational interactions, such as the contents of dry storage casks for high burn-up nuclear fuel.

Vibrational spectroscopy/ARS is a global active acoustics approach and therefore the inaccessible components and structures inside of the TN-32, including the basket and fuel assemblies, will impact the vibrational response of the exterior. A related idea has been proposed for containers for Special Nuclear Materials. Preliminary studies on tampered seals on empty 55-gallon drums were performed [85], however, no studies on cargo-container interaction were reported in the mentioned work. Moreover, no follow-up work has been reported regarding these efforts. The applications of linear vibrometry in this chapter primarily focus on modal frequencies and the associated mode shapes. The data reported in this chapter were acquired from one specific TN-32 cask under two different conditions. Vibrational modes of an unloaded TN-32 were identified through impulsive and continuous wave (CW) spectroscopic techniques, and a comparison of these two techniques is provided. In addition, FEA of complex structures has emerged as a valuable tool to assist damage identification from mode shape measurements [86]. FEA of an unloaded cask based on detailed schematics was used to confirm the identity of the modes measured experimentally. Through FEA, modes with large activity in the internal structure were identified. FEA was then undertaken on a loaded cask to explore the potential of these modes as a probe of the state of the internal cargo. As this is the first vibrational study for this type of system, the results reported here constitute a baseline for subsequent studies of the cask under a wider range of conditions.

The remaining portion of this chapter is organized as follows. In Section 2.2, the experimental details and methods are described. In Section 2.3, the experimental data is

presented along with the comparisons with FEA. Section 2.4 presents the results of the FEA of a loaded cask. The discussion is contained in Section 2.5, followed by a summary of this chapter in Section 2.6.

2.2. MATERIALS AND METHODS

2.2.1. TRANSNUCLEAR-32 (TN-32) DRY STORAGE CASK

A TN-32 cask is a steel dry storage cask that houses 32 high burn-up nuclear fuel assemblies. The cask is 5.1 m tall and 2.5 m in diameter and has a complex internal structure [Figure 2.1.1(c)]. It weighs more than 100 metric tons when fully-loaded with fuel rod assemblies. Each assembly consists of an array of 17 x 17 fuel rods, and each fuel rod is filled with enriched uranium pellets [Figure 2.2.1.1(a)]. Each fuel rod assembly slides into one of the slots in the basket inside the cask [Figure 2.2.1.1(b)]. A spring system in each fuel assembly pushes against the lid of the TN-32 cask so that the assemblies remain at a fixed position inside the basket. The multi-layered shell contains a heat conducting layer and a 12 cm neutron absorption layer. The neutron absorption layer encases the main cylinder and has inconsistent mechanical coupling to the interior; therefore, it is not an ideal acoustic pathway to probe the internal structure. For this reason, the top and bottom rims, and the trunnions are the only direct acoustic pathways into the interior of the cask. The bottom rim is of primary interest, since it is in the closest proximity to where the basket and fuel rod assemblies rest in the cask and thus where the mechanical coupling of the assemblies and cask occurs. Over the course of the project, data were taken from a specific TN-32 cask in four distinct configurations. The data from two specific configurations are

reported here, one with the cask in a storage configuration having vertical orientation (referred to as Study I), and one with the cask loaded onto a transportation skid in a horizontal configuration (referred to as Study II). In both cases, there were no fuel assemblies in the cask and the cask was sealed. In Study II, a protective dome was in place, while in Study I, the dome was not present.

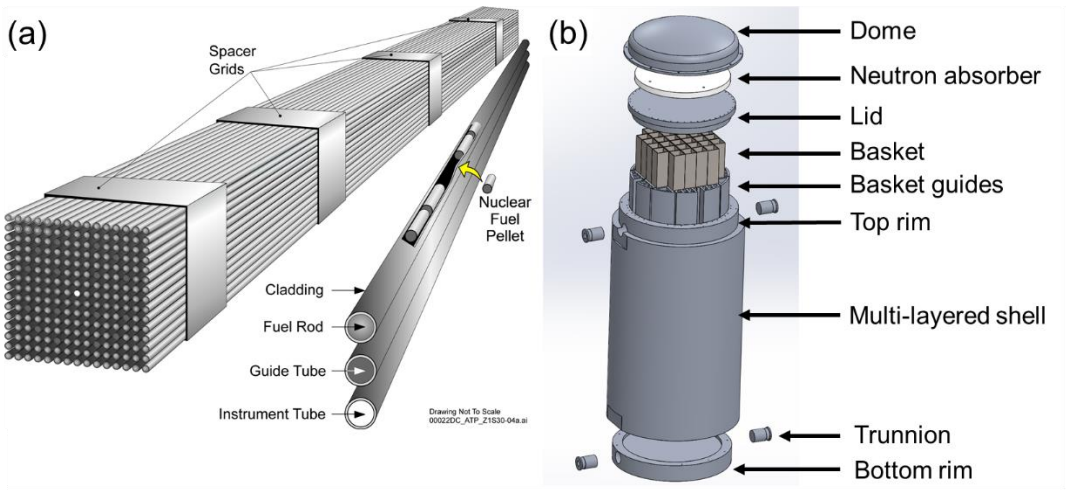

Figure 2.2.1.1. (a) Schematic of nuclear fuel rod assembly[2] (b) Simplified schematic of a TN-32

2.2.2. EXPERIMENTAL METHODS

Two excitation methods were used in this work, swept CW and impulsive. For the swept CW method, an electrodynamic shaker (Crowson T108SM) was mounted on one of the trunnions using a custom magnetic mount. The trunnions were used because they supplied a direct acoustic

[2] U.S. Department of Energy (Public domain). http://energy.gov/sites/prod/files/styles/borealis_photo_gallery_large respondxl2/public/fuel_assembly_for_production_of_nuclear_power.jpg.

path into the interior of the cask and provided for consistent coupling. The shaker was driven by a lock-in amplifier (Stanford Research System SR850) coupled with an audio amplifier (Stewart Audio World 600). For both studies, an array of seven single-axis PCB accelerometers (352C04, 10 mV/g) were deployed around the cask to collect signals. The sensor data were captured using two 4-channel digitizers (NI-9233, 50 kHz sampling rate) and the entire system was controlled using a custom LabVIEW interface [Figure 2.2.2.1]. For the impulse study, a custom metal pendulum and a dead blow hammer were used to provide high and low frequency stimuli, respectively. Only the data acquired from the dead blow hammer are reported for comparison with the CW method. The excitations were applied at the surfaces of the trunnions and the top and bottom rims. The impulse data were acquired to examine the feasibility of using this excitation method to identify the modes of the structure in a rapid fashion.

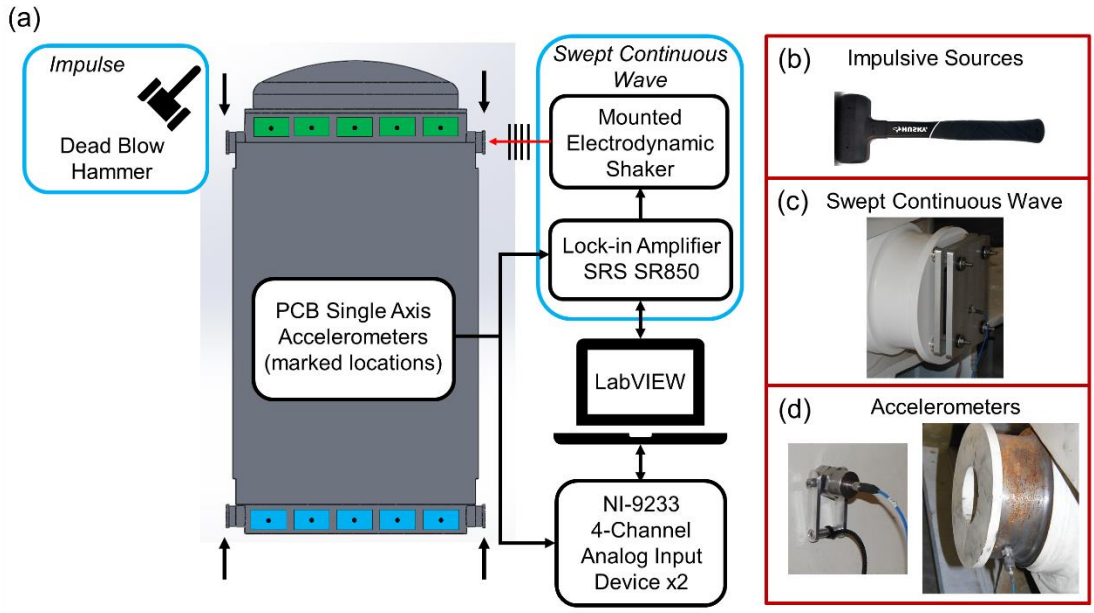

Figure 2.2.2.1. Experimental setup for the full-scale TN-32 studies. (a) Schematic diagram of the measurement system. (b) The dead blow hammer used as low-frequency impulsive excitation source. (c) Shaker mounted on a trunnion for continuous wave studies. (d) Accelerometers with magnetic mounts deployed at various locations.

Figure 2.2.2.2 shows examples of the experimental data analysis techniques. Data from the impulse studies were analyzed using a time-frequency approach (spectrogram). Modal frequencies can be determined by identifying the peaks which persist in time in the spectrogram [Figure 2.2.2.2(a)]. The quality factor (Q) of each mode was calculated by fitting the decay time of the signal amplitude at the corresponding frequency. The Q can be defined in the time domain as the number of periods for the amplitude to decay by a factor of $e^{-\pi}$ [Figure 2.2.2.2(b)]. In the CW study, vibrational spectra were generated by performing FFT's on the time-domain response at each frequency step and extracting the fundamental amplitudes [Figure 1.2.3]. In this case, the quality factor was obtained by fitting each peak in the linear spectrum with a Lorentzian function.

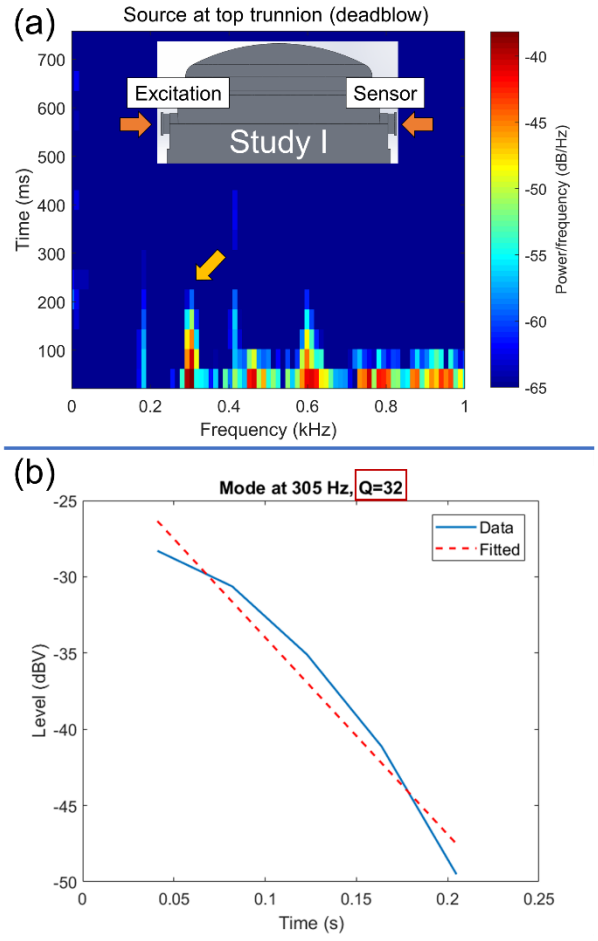

Figure 2.2.2.2. Examples of experimental data analysis techniques for the impulse method. (a) A representative spectrogram acquired by exciting with a dead blow hammer, and (b) Semi-log plot of the associated amplitude vs. time curve for the indicated mode from which quality factor is determined.

2.2.3. FINITE ELEMENT ANALYSIS

A SolidWorks CAD model was built based on the schematics of the TN-32 with practical simplifications [Figure 2.2.1.1(b)]. This CAD model was imported into COMSOL Multiphysics, where an eigenfrequency study was conducted using structural steel as the linear elastic material, with density $\rho = 7850\ \mathrm{kg/m^3}$, Youngs modulus $E = 200\ \mathrm{GPa}$, and Poisson's ratio $\nu = 0.3$. Exploiting symmetry, the geometry of the TN-32 was cut in half by the plane that goes through the centers of the trunnions. Only half of TN-32 was simulated with a symmetry boundary condition applied to the originally connected surface on the cut plane. This symmetry can be exploited due to the fact that the TN-32 was excited at the trunnions experimentally. For the rest of the model, the free boundary condition was used, as it provided the best-match to the experimental results compared to other boundary conditions. Fully-loaded scenarios were also simulated by introducing 32 square rods that were rigidly attached to the bottom of the cask but under free boundary conditions on all the other surfaces. Because of the complexity of simulating actual fuel assemblies consisting of a 17 x 17 array of fuel rods, the geometry of a simulated fuel assembly was simplified to a solid rod with square cross section. The main contacts between the fuel assemblies and the TN-32 are at the bottom, so they were modeled as rigidly attached for simplicity. The material for the square rods was mimicked by using the elastic property of zircalloy ($E = 99.3\ \mathrm{GPa}, \nu = 0.37$) and 50% of the density of uranium dioxide ($\rho = 5785\ kg/m^3$). This was based on the fact that the uranium pellets are mostly uranium dioxide encased in zircalloy, and the fuel rods are spatially separated by the grids.

2.3. EXPERIMENTAL RESULTS

2.3.1. MODAL IDENTIFICATION USING THE SWEPT CONTINUOUS-WAVE AND IMPULSE METHODS

The swept CW and impulse data shown in Figure 2.3.1.1 were acquired in Study I using similar sensor locations and excitation positions. Strong S/N (> 40 dB) and well-defined modal structures were observed with both methods. Table 2.3.1.1 lists the modal frequencies from both techniques and identifies their circumferential and axial mode numbers. There is a reasonable agreement for the 1st, 3rd, 5th and 6th measured modal frequencies in both techniques at this sensor location. For the 2nd identified mode, the impulse method lacked the resolution to observe it as there is a trade-off between frequency, time and S/N with the spectrogram analysis. For the CW method, the 2nd and 4th modes were only identifiable by sensors at other locations (see next paragraph and Section 2.3.1.). The associated Q's calculated were higher in the impulse method, but the relative relationships between those were conserved, with 6th mode as an exception.

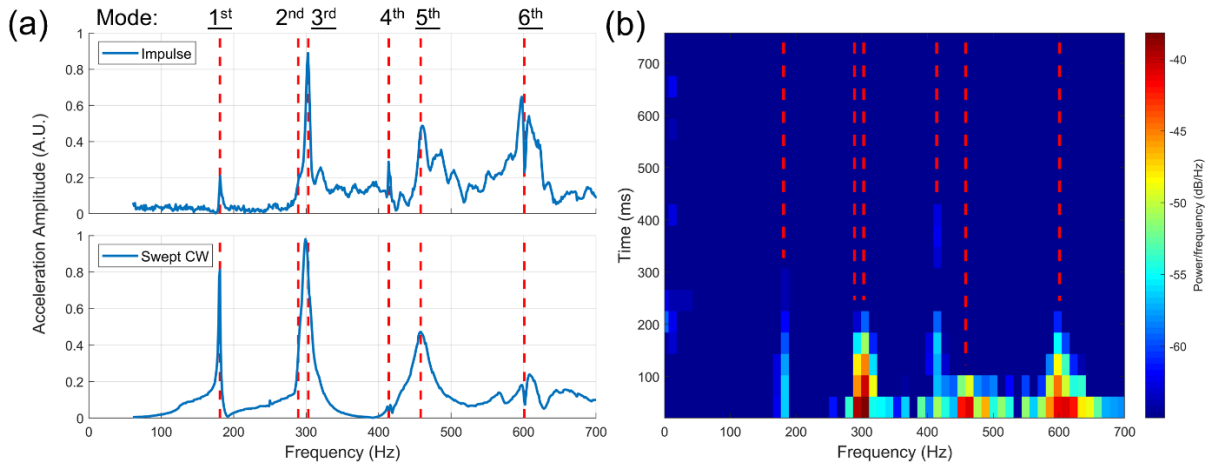

Figure 2.3.1.1. (a) Comparison between the frequency spectra from swept CW and impulse methods. These signals were taken with similar sensor locations (upper trunnion) and similar excitation locations (opposite upper trunnion) from Study I (see Figure 2.2.2.2(a) for schematic). The dashed lines mark the resonance frequencies identified with the CW method. The 1st, 3rd, 5th and 6th modes (underlined, see Table 2.3.1.1) are comparable between these two methods. The remaining two modes in the CW spectrum were identified through other sensor locations. The 2nd mode was not identified in the impulse method. (b) Comparison of the modes using the spectrogram from the impulse method.

Table 2.3.1.1. Comparison of modal frequencies and associated quality factors (Q) from the swept CW and impulse methods. The frequency resolution (12 Hz) of the impulse method cannot resolve the 2nd mode. For the 6th mode, the axial mode number was not determined.

Frequency / Q	**1st mode**	**2nd mode**	**3rd mode**	**4th mode**	**5th mode**	**6th mode**
Swept CW	181 Hz / 51	289 Hz / 28	303 Hz / 16	414 Hz / 191	458 Hz / 17	601 Hz / 76
Impulse	183 Hz / 68	-	305 Hz / 32	415 Hz / 200	464 Hz / 31	598 Hz / 67
Mode	(2, 0)	(1, 2)	(2, 1)	(1, 3)	(2, 2)	(4, x)

Mode shapes were identified by the CW method. In the storage configuration (Study I), seven sensors (including one at the excitation source) were deployed around the top rim. The six modes were determined using both the magnitude and phase information from the spectra. In Figure 2.3.1.2, the first five measured modes are compared with results from the FEA (animated versions are in **Error! Reference source not found.**). The modes are labeled by (*m*, *n*), the circumferential and axial mode numbers, respectively. The average surface displacement ratio of the bottom of the unloaded cask relative to a trunnion was calculated in FEA to quantify the ability to couple energy into interior due to excitation on the trunnion [Table 2.3.1.2]. The (1, 2) and (1, 3) global bending modes show the largest displacement ratios and activity in the basket [Figure 2.3.1.2(b) and (d)], while the other modes show less activity in those locations [Figure 2.3.1.2(a), (c) and (e)]. In particular, the displacement ratio for the (1, 2) mode is 3 to 10 times larger compared to the other identified modes. FEA provided good predictions on experimental results, however, there are still disagreements between them. For example, the (1, 2) and (1, 3) mode shapes from the experiments are more complicated than simple sloshing motions predicted by FEA (see animated modes). The (3, 0) pure radial mode and (3, 1) radial motion with shearing mode were numerically predicted to appear between the 3rd and 4th mode, but they were not identified experimentally. The FEA predicted resonance frequency started to deviate more significantly at the 5th mode [Figure 2.3.1.2(e)], and FEA failed to predict the observed 6th mode, which is a 4th order circumferential mode.

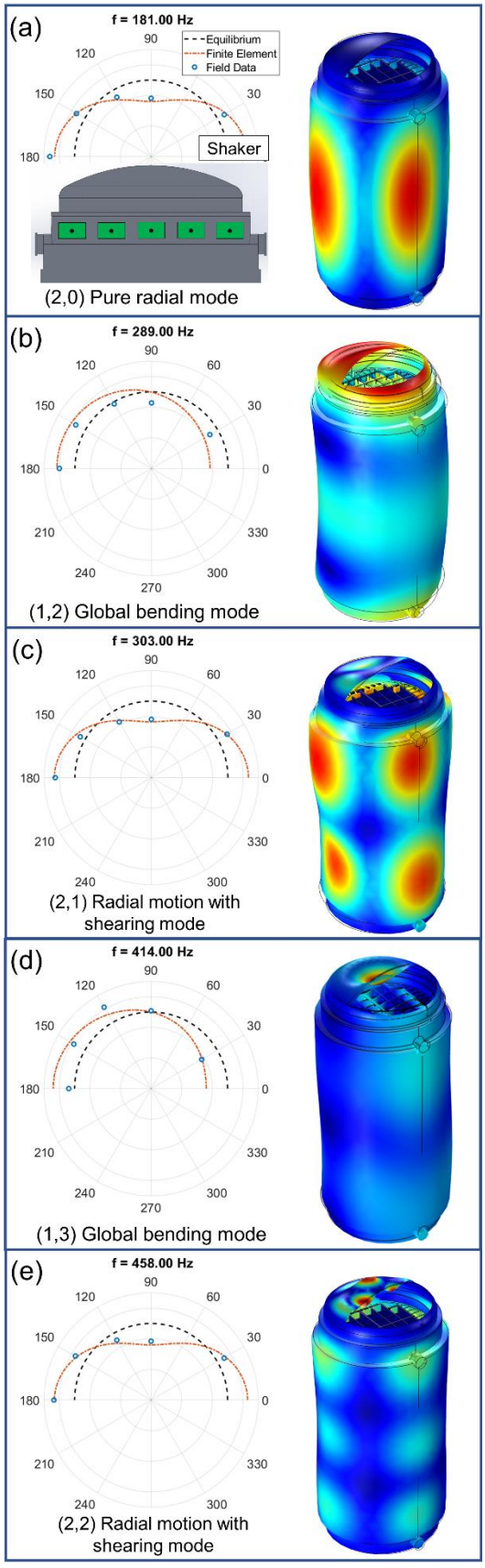

Figure 2.3.1.2. Mode shapes along the top rim experimentally identified from the vertical configuration (left) and the corresponding modes (a - e) from finite element simulations (right). The boxes on the cask show five of the measurement points on the top rim of the TN-32. Along with one on the opposite trunnion and one on the excitation source, there were a total of 7 measurement points on the TN-32. The polar plot represents a top-down view of the TN-32 with the shaker at 0° and the other trunnion at 180°. The dashed line indicates the equilibrium position; the dash-dot line indicates the FE simulation results; the circles indicate the responses from each sensor locations. The sensor at 60° was not phase referenced to the other sensors as it was run through a lock-in amplifier instead of the NI-5532, thus, it is not shown. Both the field data and simulations were normalized to their individual root mean square value. (b) and (d) are the (1,2) and (1,3) global bending modes which exhibit large responses in the basket and at the bottom of the cask. (Animated versions are in **Error! Reference source not found.**)

Table 2.3.1.2. Predictions from FE simulations on TN-32 with and without rods of square cross section as surrogate fuel assemblies. The listed modes are the ones that correspond to Figure 2.3.1.2. The bottom/trunnion displacement ratio is the average displacement ratio of the bottom of an unloaded TN-32 to the surface of a trunnion. The cargo/trunnion energy is the average vibrational energy ratio of fuel rod array in a fully-loaded TN-32 to the surface of a trunnion. The 2nd and 4th modes have larger displacement and energy ratios and changes in resonance frequency.

Mode	Unloaded (Hz)	Loaded (Hz)	% change	Bottom/trunnion displacement ratio	Cargo/trunnion energy ratio
1st / (2, 0)	199.31	198.27	-0.5%	0.09	0.02
2nd / (1, 2)	310.36	316.99	2.0%	1.03	0.44
3rd / (2, 1)	347.14	344.90	-0.6%	0.13	0.02
4th / (1, 3)	447.21	443.68	-0.8%	0.32	0.46
5th / (2, 2)	536.72	534.79	-0.4%	0.23	0.03

2.3.2. COMPARISON OF STORAGE AND TRANSPORTATION CONFIGURATIONS

When a TN-32 is being transported, it is mounted horizontally on a transportation skid and loaded on a truck [Figure 2.3.2.1(bottom right)]. The contacts between the cask and the skid happen at the top rim and bottom trunnions. These contacts are buffered with rubber. In this configuration, the acquired spectra show that the modal frequencies are shifted to lower values in the region below 800 Hz relative to the storage configuration [Figure 2.3.2.1(top)]. This suggests a mass loading effect due to the skid predominates below 800 Hz. The mass loading effect of the dome was eliminated as a cause because FEA did not predict a significant frequency shift. Above 800 Hz, the spectra from the two configurations are markedly different. The implication of this result will be addressed in Section 2.5.

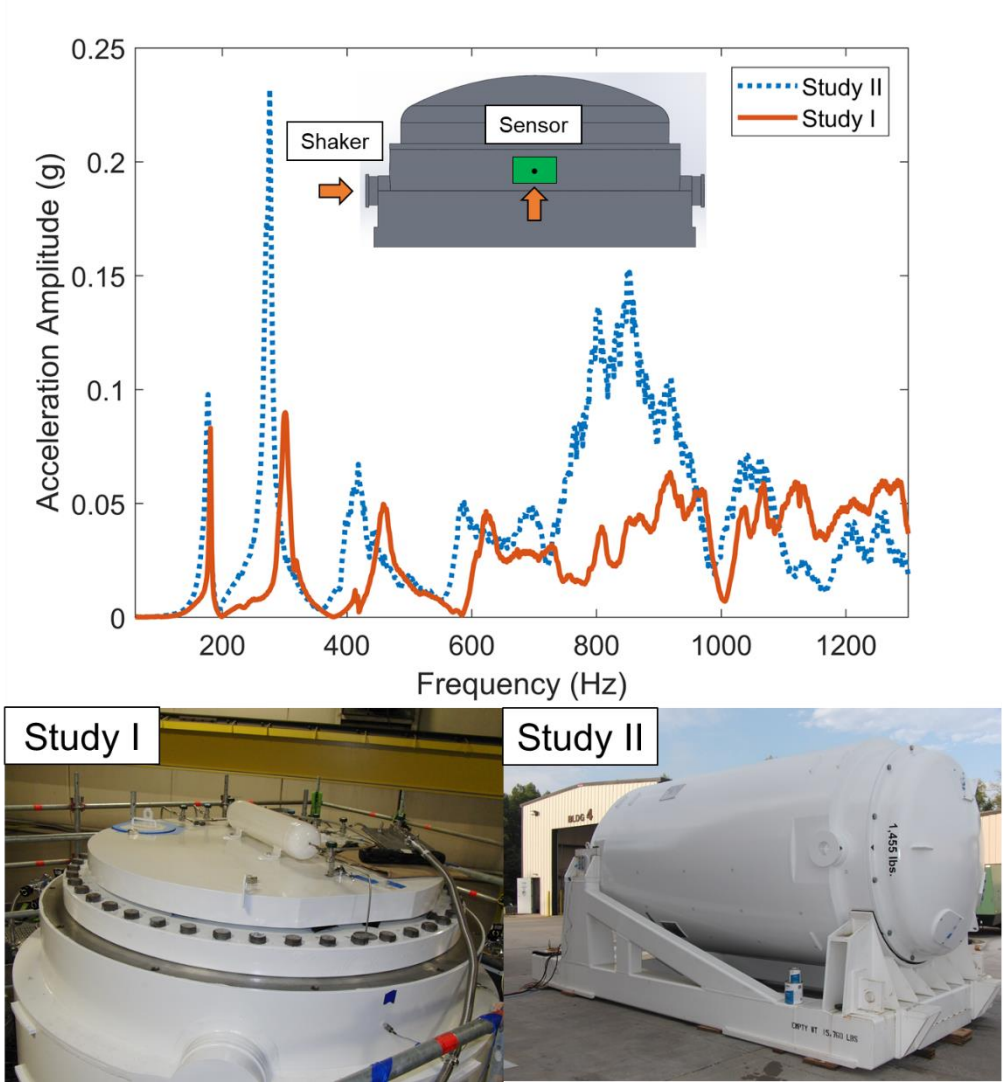

Figure 2.3.2.1. Comparison between the spectra from storage and transportation configurations. The spectra are similar to each other below 800 Hz. Pictures of these two configurations are shown at the bottom.

2.4. FINITE ELEMENT ANALYSIS OF A FULLY-LOADED TN-32

To examine the impact of cargo on the cask modes, FEA was performed using rods (square in cross section) as surrogate fuel assemblies inside the TN-32 cask. The rods were rigidly attached to the bottom of the cask but under free boundary conditions on the other surfaces. Additional modes appeared due to the extra degrees of freedom contributed by the rods. Most of these are internal modes that have large vibrational energy ratio (10^2 – 10^5) between the

response of the rods to the response of the trunnion on the exterior. These modes are harder to excite from the exterior and thus of little relevance to this study. This is supported by the field measurements in which identifying the internal modes involving the basket was difficult. Still, there are modes with small internal-to-external response ratios which have clear correspondences with the modes identified in the field [Table 2.3.1.2 & Figure 2.4.1]. Although the FEA model constructed in this work is idealized for the coupling between exterior and interior, energy is expected to propagate into the fuel rod assemblies via the same modes identified in the field, and thus it is possible to probe internal conditions. Especially for the (1, 2) and (1, 3) modes, about 20 times more energy can be coupled into the fuel assemblies than with other identified modes. These two modes also have larger percentage changes in frequency after being loaded with the surrogate rods [Table 2.3.1.2]. The larger modal displacements on the off-centered fuel rods suggest that the sensitivity of vibrometry will be higher for damage occurring at these locations [Figure 2.4.1]. The results of these simulations support the hypothesis on the global bending modes being more sensitive to the condition of the fuel assemblies.

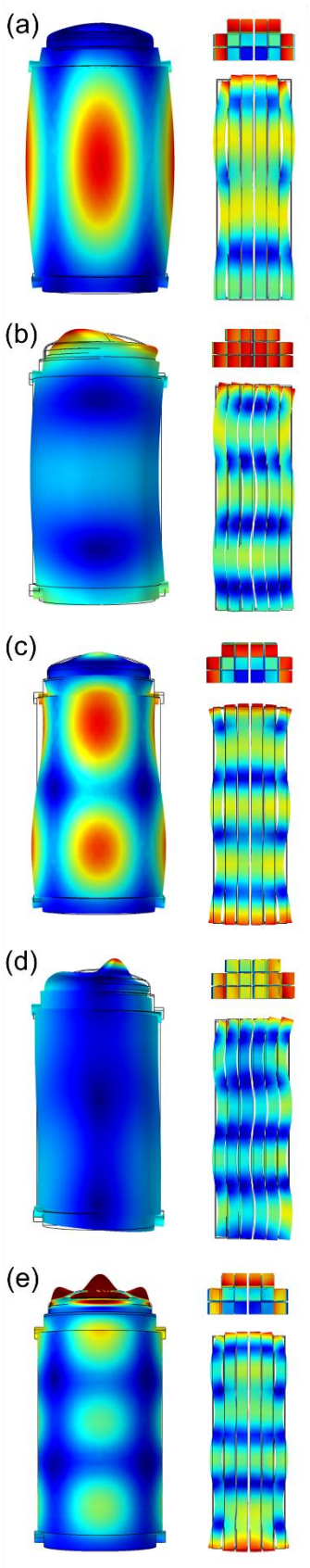

Figure 2.4.1. FE simulations of a fully-loaded TN-32. The mode shapes of the cask shell, with side and top views of surrogate fuel rod assemblies are shown. The modes shown in (a-e) correspond with those shown in Figure 2.3.1.2. The rods on the edge experience larger modal displacement in most cases.

2.5. DISCUSSION

Both the impulse and swept CW methods gave consistent results in the modal frequencies and the associated quality factors. The quality factor obtained by the impulse method was higher than the swept CW method in general, which indicates a possible dependence on excitation amplitude. The dependency on external factors makes the quality factor a poor metric for characterizing internal damage in the field. Although the impulse method is fast from a setup and acquisition perspective, there are many reasons to prefer the swept CW method. Excitation by a shaker can be precisely controlled while the impulse approach is more subject to variations, such as excitation location and amplitude. The spectral resolution is generally lower in the impulse method because of the trade-off between the time and frequency resolution of the spectrogram. Moreover, the CW method is less susceptible to noise, especially with the phase sensitive lock-in amplifier. Lastly, the CW method allows for the acquisition of harmonic spectra which is not possible in the impulse approach.

One of the challenges of this work has been to identify mode shapes for direct comparison with those predicted by FEA. Ideally, deploying an array of sensors evenly around the cask will yield sufficient information on the mode shapes. However, poor acoustic coupling between the neutron absorber and the primary wall prohibits mounting sensors on the shell of a TN-32 cask. Trunnions and top/bottom rims are the only locations that allow for reliable and consistent distributed measurements. Due to time constraints and the limited number of sensors in the field, data were acquired with source and sensors all at the top rim or all at the bottom rim. Because of this, the relative phase between motions detected at top and bottom rims was not directly measured and the correspondence between the measurements and mode shapes were not

completely determined. Taken together with the FEA results, however, the first five among the six measured modes were clearly identifiable. Among these five modes, two were harder to identify. The (1, 2) mode [Figure 2.3.1.2(b)] exhibited some overlap with the (2, 1) mode [Figure 2.3.1.2(c)] and likewise the (1, 3) mode [Figure 2.3.1.2(d)] with the (2, 2) mode [Figure 2.3.1.2(e)]. The sensors at 30° and 60° on the top rim were more sensitive to those modes. Because of these modal overlaps, the measured shapes of (1, 2) and (1, 3) modes show some breathing motions on top of sloshing motions (see supplementary files). The (1, 2) and (1, 3) global bending modes can be exploited to probe the conditions of the internal cargo due to their large response in the basket structure and at the bottom of the cask, where the basket and fuel rod assemblies are in direct contact. The FEA on a fully-loaded cask also show a larger response from the surrogate fuel assemblies in these two modes than in the other identified ones.

Based on the results from the transportation configuration, the shape of the frequency spectrum below 800 Hz is very similar to the one from the storage configuration with a frequency offset, despite the differences in boundary conditions. Therefore, the five modes identified in the storage configuration, which are below 800 Hz, are also expected to be identified in the transportation configuration. This, along with the consistent mechanical coupling provided by the spring system in each of the fuel assemblies, potentially allows the simulation results of a fully-loaded cask under the storage configuration to be applied to the transportation scheme. Further studies will be required to confirm this. With this assumption, one of the potential applications is for monitoring during different stages of transportation. Accelerometers can be mounted to the cask to obtain spectra before, during and after transport. If unusual changes are

observed in the spectra, more involved radiometric and charged particle methods (e.g. gamma ray tomography, muon imaging) can be applied.

2.6. SUMMARY

This chapter evaluates the feasibility of applying ARS on the NDE of TN-32 by acquiring the vibrometric data on an intact and unloaded TN-32 cask. The first few modes identified from impulse and swept CW methods agree reasonably well with each other, and also match with FEA. In particular, two global bending modes with larger responses in the basket and at the bottom of the cask were identified. FEA on a TN-32 cask loaded with surrogate fuel assemblies also show a larger response from the fuel assemblies in these two modes. Thus, the hypothesis is that it is possible to probe the conditions of the fuel assemblies with these two modes from measurements made on the exterior of the cask. These results also provide a knowledge base for further studies involving the detection of abnormalities and structural changes in internal configuration of dry storage casks. Subsequent studies will allow the comparison of these baseline measurements with the spectra from other casks with a focus on the five identified modes. Spectra acquired in both transportation and storage configurations also suggest that the five identified modes are rather robust to changes in orientation and structural support, so these modes can be useful for monitoring the cask during transportation. To realize such an application, a means of studying different internal conditions in a TN-32 would be ideal. Therefore, a 1:6 scale model of the TN-32 was manufactured for laboratory studies. The down-scaled cask permits the acquisition of data under various internal test configurations (e.g., damage scenarios) that are not possible with an actual TN-32. The vibrometric data from the TN-32 will be compared with

the scaled cask to better understand the changes in modes resulting from changes in the integrity of internal components and structures in the next chapter.

3. VIBRATIONAL METRICS FOR THE INTERNAL STRUCTURAL INTEGRITY IN A LAB-SCALE CASK

3.1. POSSIBLE DAMAGE SCENARIOS ON THE ENCLOSED SPENT FUEL ASSEMBLIES

Due to various issues in countries that include the USA, Japan and South Korea, spent nuclear fuel (SNF) has been stored inside dry storage casks beyond their current licensed service lives as final repositories are yet to be chosen and constructed [62]. Because of the extended storage burden, concerns have been raised about the integrity of the dry storage casks and the SNF inside, which were not of concern for operation within the standard service life [87]. Both SNF and internal structures of the cask itself are subject to various degradation mechanisms which have been reviewed in earlier work [62,88]. The prioritization of these potential problems for extended storage varies from country to country. To aggregate the knowledge pertaining to this complex problem, a report from the Extended Storage Collaboration Program [89] identified several technical data gaps of high priority, including hydride effects on fuel cladding, retrievability of fuel after storage, general canister corrosion and stress corrosion cracking (SCC) of closure welds, degradation of bolts and seals, and concrete degradation. These mechanisms have raised technical and public concerns for the storage and transportation of casks under extended storage conditions. One of the central concerns is nuclear criticality resulting from accidents during the transportation of degraded casks [90]. Various possible transportation accident scenarios have been studied [91–93], and past accidents have been reviewed [94]. In a dry storage cask, subcriticality is maintained by appropriate burnup credit, neutron absorbers,

moderator exclusion, basket spacing and fuel configuration [90]. It is desirable to have a set of rapid NDE tools available to monitor the integrity of these components inside dry storage casks given the possibility of such transportation accidents during extended storage.

The focus of this chapter is on developing NDE techniques for evaluating the state of contents and internal structures of the casks. Some active acoustic NDE methods were reviewed in Section 1.1. Currently, there are no fielded monitoring methods for the internal structures, but two techniques are being developed for near-term field deployment [64]: Changes in the thermal and γ images of the cask can be used to detect fuel relocation, and speed of sound measurements across canister gas space with a pitch-catch method can be used to detect fuel failure. The latter relies on Xenon and Krypton release from the fuel rod cladding failure, which will change the average speed of sound of the helium fill gas. The main restriction of the pitch-catch technique is in the requirement of an unobstructed path for sound to propagate across canister gas space, which is not the case for all dry storage casks. There are a few other acoustic NDE techniques focusing on the Zircalloy cladding that are further away from field deployment [95–97], and all of them require direct access to the cladding.

Vibrational spectroscopy, also referred as Acoustic Resonance Spectroscopy (ARS) [17], is a global technique. Since the vibrational response at any location can be influenced by the entire system, the inaccessible components and structures inside of the dry storage casks, including the basket and fuel assemblies, can impact the vibrational response of the exterior. This approach may provide an alternative method to extract information on the fuel assemblies. Contrary to the pitch-catch technique, the only requirement is the coupling of vibrational energy from the exterior of the cask to the fuel assemblies, which is possible in all dry storage casks. To apply ARS

to the NDE of the fuel assemblies, the knowledge of the mechanical aspects of the cargo-container interactions is crucial. Relevant work has been reviewed in Section 1.1 and Section 2.1.

In a Chapter 2, five vibrational modes of a full-scale TN-32 cask in the field are identified and the applicability of vibrational spectroscopy in both the storage and transportation scenarios is evaluated. However, internal damage scenarios cannot be introduced on a full-scale TN-32 cask for practical reasons, therefore a 1:6 scaled model based closely on the design of the TN-32 was fabricated for study in the lab. This chapter first presents the modal correspondence between a full-scale TN-32 [Figure 3.1.1(right)] and a 1:6 scaled lab cask [Figure 3.1.1(left)], and then introduces a vibrational NDE technique to assess the condition of surrogate fuel assemblies inside the lab cask. The main goal of this chapter is to develop metrics derived from vibrational spectra that have the capability to predict the state and configuration of cargo in the cask. A two-point measurement approach was developed in order to establish a technique that would be straightforward to apply in the field. The metrics were derived from the amplitude and phase information from spectra captured at two locations of the cask.

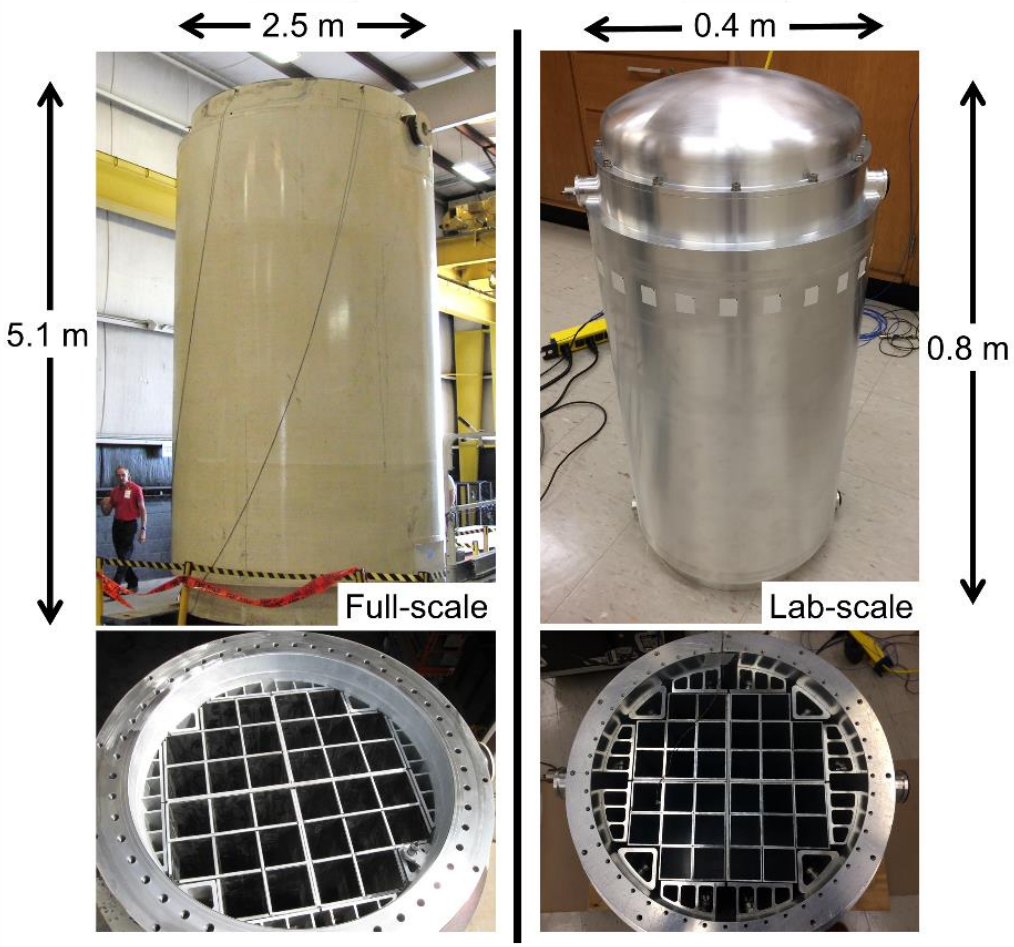

Figure 3.1.1. The Transnuclear-32 (TN-32) (top left) and 1:6 lab-scale model (top right) cask studied during the project. Top view of the basket structures for the TN-32 (bottom left) and the lab cask (bottom right).

The remainder of this chapter is organized as follows. In Section 3.2, the determination of the vibrational modes of the scaled lab cask via comparisons between experiments and FEA is presented. In Section 3.3, the vibrational metrics are described, and their sensitivity to the configurations of the cargo in the sealed lab cask are evaluated. This is followed by the discussion in Section 3.4, and a summary in Section 3.5.

3.2. VIBRATIONAL MODE IDENTIFICATION

3.2.1. LABORATORY SCALE DRY STORAGE CASK

To study the abnormality in the internal structure of the TN-32 in a controlled manner, a 1:6 scaled cask was fabricated in-house with a design based on an original schematic of the TN-32. The details on the original TN-32 can be found in Section 2.2.1. There were three important structural differences between the lab cask and the TN-32 cask. First, due to cost and weight issues, the lab cask was made from Aluminum 6061-T6 instead of steel. Second, the lab cask did not have a polymer-type neutron absorption layer and the associated thin external shell around the main cylindrical body of the cask. Third, the cylindrical body was made from a single piece of material as opposed to being multi-layered.

Based on the previous studies of the TN-32 cask and knowledge of its structure, the chosen points of excitation and measurements were on the trunnions and the top and bottom rims [Figure 2.2.1.1(b)]. These points provide the only direct pathways into the interior of the TN-32, since its sidewall is encased in a neutron absorption layer with inconsistent mechanical coupling to the main cylinder. With the lab cask, the rims and trunnions were consequently the primary measurement points, with the exception of the mode mapping studies from the main shell using a laser Doppler vibrometer (LDV). The response of the bottom rim was of particular interest as it is part of the base plate where the fuel assemblies rest. Thus, the bottom rim provides direct access to the points of mechanical contact between the cask and assemblies.

3.2.2. EXPERIMENTAL METHODS

A shaker (Dayton Audio DAEX32U-4 exciter speaker, 4Ω, 40W) was glue-mounted on a bottom trunnion and driven at 0.25 W by a power amplifier (TECHRON Model 5507) which was connected to a lock-in amplifier (Stanford Research System SR850). For the mode shape acquisitions, the lid and dome were in place, but the basket was not included. The data were acquired using an LDV (Polytec PDV-100) mounted on a custom scanning track. The LDV was connected to the lock-in amplifier which was controlled by a custom LabView interface. Due to the symmetry through the plane of trunnions, only half of the cask was mapped. The measurement grid consisted of 56 total points (seven circumferential by eight vertical points on the shell) [Figure 3.3.2.1]. The amplitudes and phases of the fundamental spectra were obtained from the lock-in amplifier.

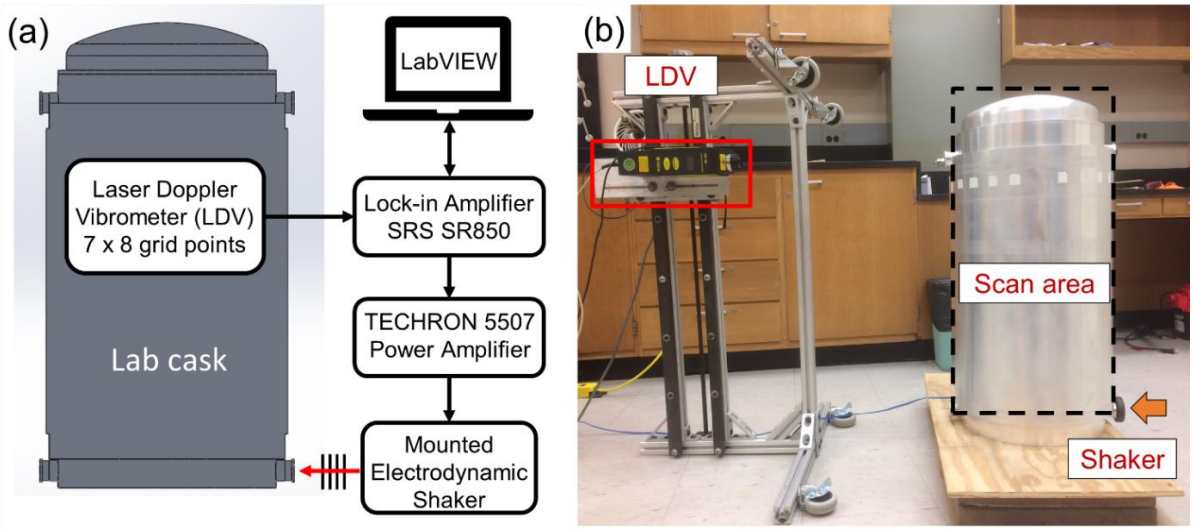

Figure 3.2.2.1. (a) A schematic diagram and (b) a photo of the experimental setup for the mode shape measurements on the laboratory cask. The LDV was scanned across the shell of the lab cask with 7 points in the circumferential direction and 8 points in the vertical direction on the shell.

3.2.3. FINITE ELEMENT ANALYSIS

A SolidWorks CAD model was built based on the schematics of the TN-32 cask, with practical simplifications [Figure 2.2.1.1(b)]. This 1:6 scaled CAD model was imported into COMSOL Multiphysics with aluminum assigned as the linear elastic material, with $\rho = 2700\ \mathrm{kg/m^3}$, $E = 69\ \mathrm{GPa}$, and $\nu = 0.33$. Eigenfrequency studies were then conducted on the model. Simulations of the system with the dome and lid installed without the basket were performed to compare with the mode shape measurements of the lab cask with the same configuration. The free boundary condition was used, as it provided the best match compared to other boundary conditions, which was the same for the full-scale TN-32.

3.2.4. RESULTS

Using the LDV data from the 56 measurement points, three modes and their associated mode shapes were identified. These shapes were then compared with those predicted by FEA. The modes were labeled with (m, n), where m is the circumferential mode number, and n is the axial mode number. Comparing these results with the field data from the TN-32 cask, a one-to-one correspondence can be found in the (2, 0), (1, 2) and (2, 1) modes between the lab cask and the TN-32 cask [Figure 3.2.4.1] (Animated versions are in **Error! Reference source not found.**). From a vibrational standpoint, this validates the lab cask as a reasonable representation of the TN-32. Of those identified modes, the (1, 2) global bending mode [Figure 3.2.4.1(b)] is of particular interest as it has a larger response at the base of the cask compared to other identified modes. A scan of the interior side of the base using the LDV also agreed with the simulation. The

(1, 2) mode is expected to be efficient in coupling energy into the basket and fuel assemblies; thus, it was used to develop the metrics for internal conditions.

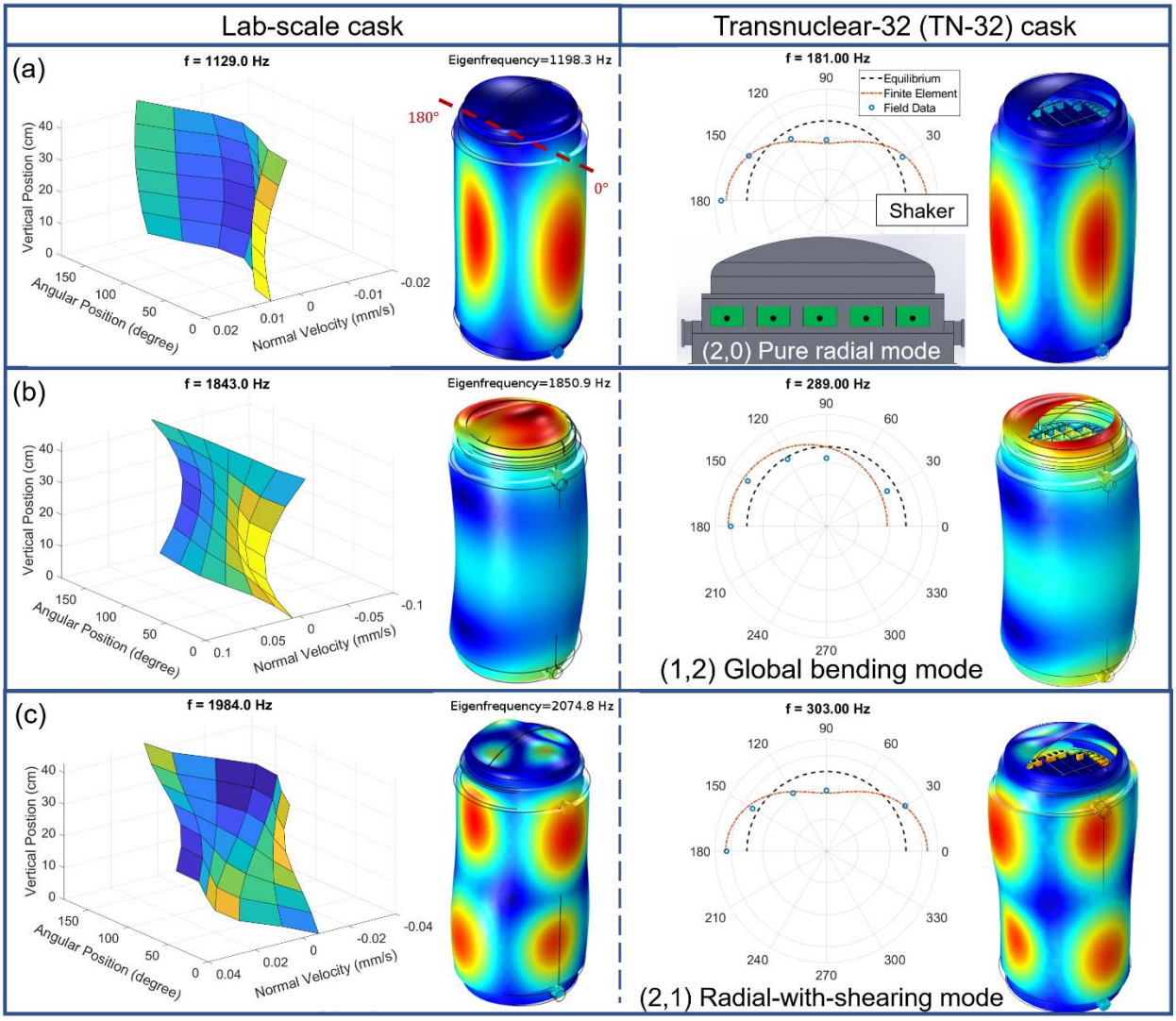

Figure 3.2.4.1. Measured and corresponding FE simulated mode shapes (a), (b) and (c) for the lab cask (left), and a full-scale TN-32 cask (right). For the TN-32 measurements, the mode shapes are shown in a top-down view, and each circle represents the positions of the accelerometers. In the schematic, the green boxes show five of the measurement points on the TN-32, in addition to another one on the trunnion. For the lab cask measurements with the LDV, the scan grid encompassing half of the cask shell is unwrapped to a planar projection. (b) The (1, 2) global bending mode with large response at the bottom was identified in both the lab and the field. (Animated versions are in **Error! Reference source not found.**)

3.3. QUANTIFICATION OF INTERNAL DAMAGE SCENARIOS

3.3.1. MATERIALS AND EXPERIMENTAL METHODS

The experimental setup is shown in Figure 3.3.1.1. In order to examine the vibrational effects due to damaged cargo inside the sealed lab cask, each of the 32 slots in the basket was configured in one of three ways: (1) with a rod bundle ("surrogate fuel assembly") in place, (2) partially filled with steel shot ("debris") or (3) empty. A rod bundle consisted of four steel rods, which were held in direct contact with each other by heat shrink tubing. Each steel rod was 1.5 cm in diameter and 55.5 cm in height. The bundles were used as surrogates for fuel assemblies which could not be practically scaled down due to their complexity. The catastrophic failure of the assembly was mimicked with steel shot of diameter in the range of 1.78 - 2.54 mm (SHS780C, Ballistic Products) and is referred to as "debris." Each slot of the basket is 2.54 cm x 2.54 cm in cross section and 66.5 cm in height. A debris slot was filled with an amount of steel shot that has the same mass as a rod bundle, and the shot extended about 95% of the height of the slot. The empty state represents a missing fuel assembly or an originally unloaded slot [Figure 3.3.1.1(b) and (c)]. In this study, two single-axis accelerometers (PCB 352C04, 10 mV/g) were used as sensors. These were glued with cyanoacrylate adhesives to the lab cask. One accelerometer was placed on the face of the top trunnion on the side opposite to the shaker. The second accelerometer was placed on the top rim at 90° from the trunnion. These two accelerometers were each connected to a signal conditioner (Kistler Dual Mode Charge Amplifiers Type 5010), and then to their individual lock-in amplifiers (Stanford Research System SR850 or SR830) which were both phase-locked to the drive signal [Figure 3.3.1.1(a)]. The rest of the instrumentation was similar to that described in Section 3.2.2 except that the shaker was driven at 3.5 W at the

bottom trunnion. The frequency range of interest was chosen to range from 1.6 to 2.1 kHz so that the identified (1, 2) global bending and the (2, 1) radial-with-shearing modes [Figure 3.2.4.1(b) and (c)] fall in range for all the different configurations. The frequency sweeps for each configuration were repeated continuously over an initial settling period until the frequency spectra became stable.

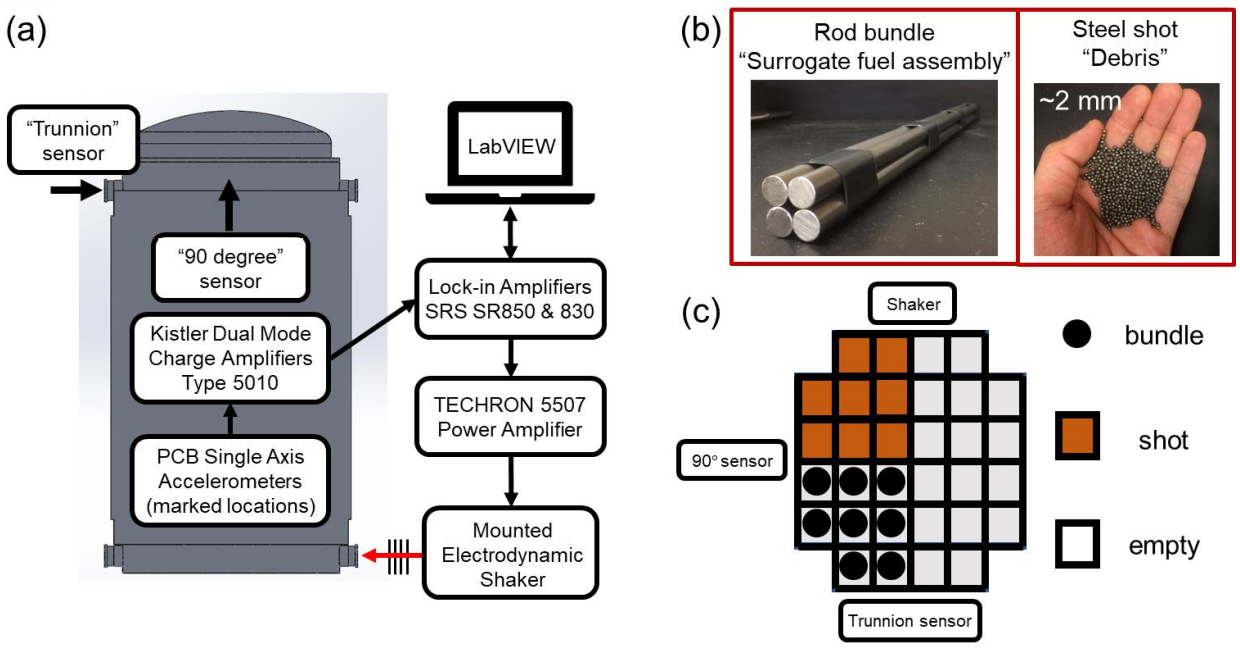

Figure 3.3.1.1. (a) The experimental setup for the dual internal cargo configuration study on the lab cask. (b) A surrogate fuel assembly consisted of 4 steel rods bundled with heat shrink. The complete structural failure of a bundle was mimicked by steel shot that has equal mass as a bundle. (c) A schematic diagram of an internal configuration defining the symbols. In subsequent figures, this type of diagram will be used as a label for the specific configurations.

In the study of the sensitivity of the metrics (Section 3.3.3.2), measurements with different configurations were conducted in a way that minimized the changes in the contact between the cargo and the bottom of the cask. Each series of measurements started with each of the 32 slots in the filled bundle state. Each subsequent configuration was achieved by the

removal of bundles so that the remaining bundles maintained their original state of contact with the cask. The frequency range analyzed in this study was from 1.5 to 2.1 kHz.

3.3.2. METRICS FOR THE INTERNAL CONFIGURATION

To quantify the conditions of the internal structure, two categories of metrics based on amplitude and phase were derived from the fundamental spectra. The amplitude metrics were derived from the amplitude spectrum from each individual sensor. The phase metrics were derived from the relative phase between the two sensors. The first amplitude metric was referred to as the *total energy* per unit mass, which was calculated by first squaring the velocity spectrum (calculated by dividing the acceleration spectrum by angular velocities) at one sensor and summing over the frequency range of interest [Figure 3.3.2.1(a)]. The second amplitude metric was referred to as the *second moment* of the amplitude spectrum, which was calculated from the normalized amplitude spectrum with respect to the weighted average frequency [Figure 3.3.2.1(b)]. The *total energy* metric quantified how much energy can be measured from the external surface of the lab cask at the positions of the accelerometers. The *second moment* quantified the separation between the (1, 2) and (2, 1) modes in frequency and was also influenced by the complexity of the spectra. The (1, 2) global bending mode is expected to be more sensitive to the interior based on its mode shape (see Section 3.2.4), while the (2, 1) radial-with-shearing mode is expected to be less sensitive, and the two will respond to internal structural changes in different ways.

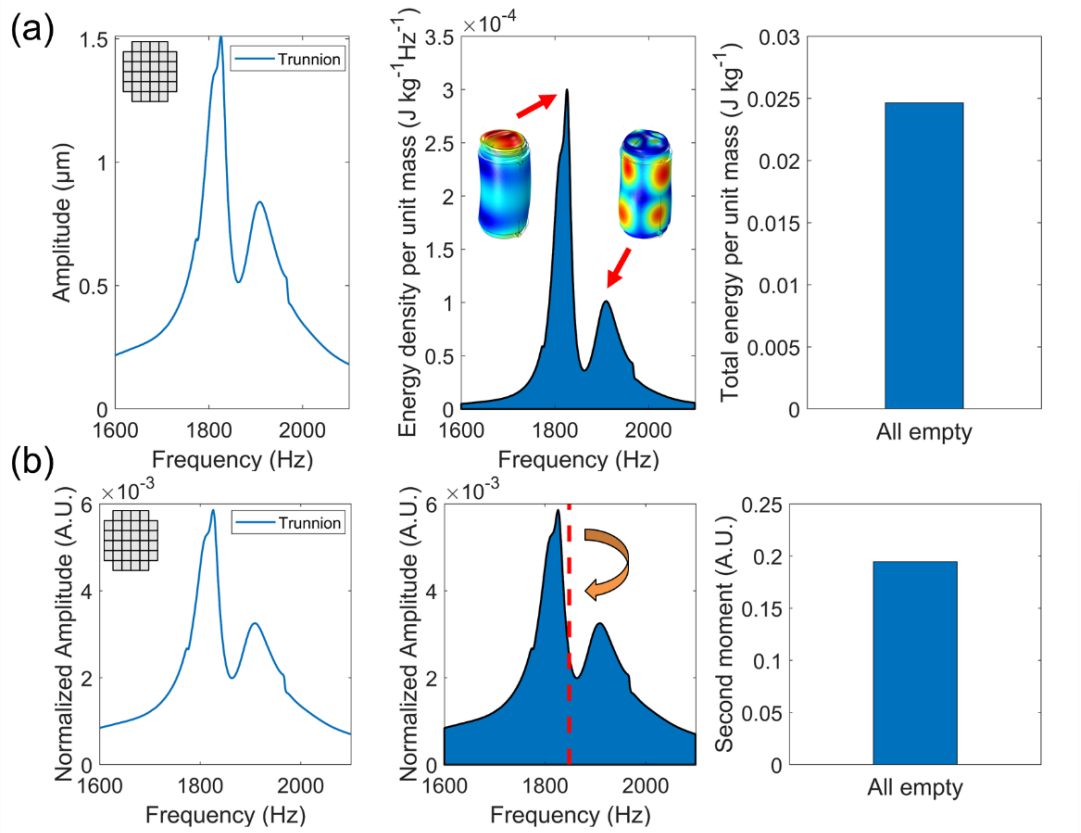

Figure 3.3.2.1. An example of calculating amplitude metrics. (a) The *total energy* per unit mass metric was calculated by first squaring the velocity spectrum at one sensor and summing over the frequency range of interest. (b) The *second moment* of the amplitude spectrum was calculated from the normalized amplitude spectrum with respect to the weighted average frequency.

The second category of metrics was based on the relative phase between the two sensors. The idea was to quantify the changes of mode shape from their phase differences in order to capture the sub-modal variations to which the amplitude metrics are much less sensitive [Figure 3.3.2.2(top) and (middle)]. Twelve metrics were calculated from the phases of the spectra acquired at the trunnion and the 90° sensors. At every frequency step, a phase modulated normalized displacement can be defined. The normalized displacements of the trunnion and 90° sensors is assumed to vary as

$$x_1(t) = \cos\left(2\pi f t + \frac{\theta(f)}{2}\right), \quad x_2(t) = \cos\left(2\pi f t - \frac{\theta(f)}{2}\right) \qquad (3.3.2.1)$$

where f is the excitation frequency, t is the time, and θ is the frequency-dependent phase difference between these two sensors. The resulting plot is a Lissajous figure with same amplitude and frequency for both axes. The figure has a general shape of an ellipse which is symmetrical about the 45° and 135° lines [98]. The enclosed area of the ellipse is calculated using the formula:

$$A = \pm\pi ab, \quad \text{where } ab = \sqrt{2\cos^2\frac{\theta(f)}{2}}\sqrt{2\sin^2\frac{\theta(f)}{2}} = |\sin\theta(f)| \qquad (3.3.2.2)$$

where a and b are the major and minor axes along 45° and 135° lines. The sign of the enclosed area was assigned by which sensor was leading in the unwrapped phase. For each frequency step, the enclosed positive or negative area in the phase ellipse was summed separately over the 1st or the 2nd half of the frequency range of interest, which corresponded to the (1, 2) or (2, 1) mode respectively [Figure 3.3.2.2(bottom)]. Four basic components, consisting of the negative and positive area of each half. These four components were then used to generate twelve phase-based metrics.

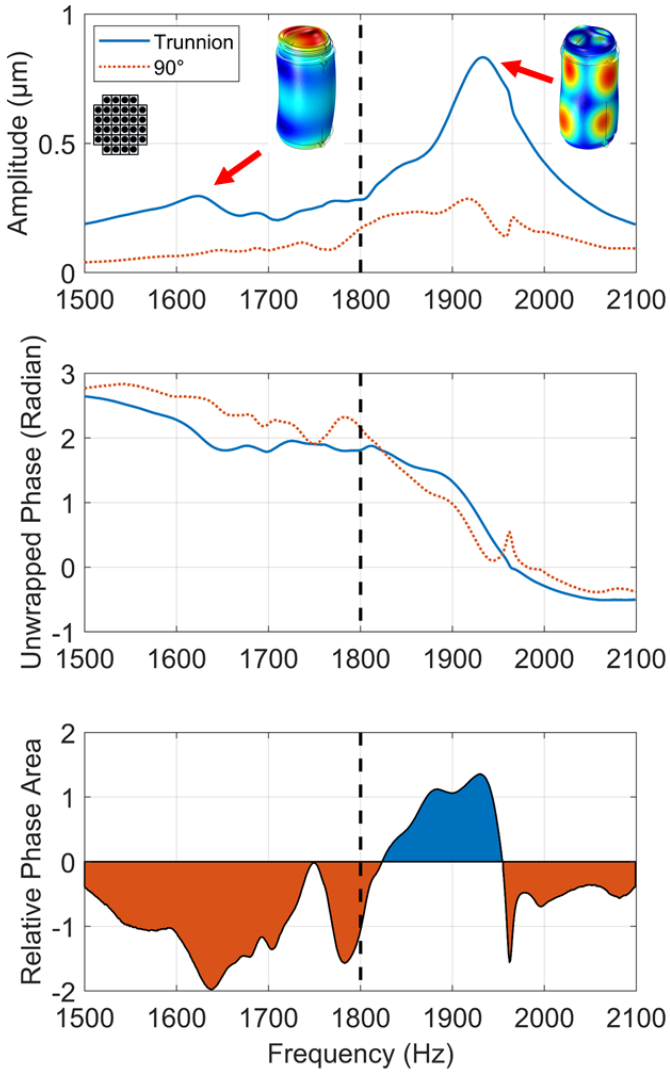

Figure 3.3.2.2. An example of phase metric calculation, shown in this case for the all-bundle configuration. (top) The amplitude spectrum with the two modes of interest identified. (middle) The corresponding phase spectra. The relative phase quantifies the changes of mode shape and is more sensitive to the variations that are less pronounced in the amplitude spectra. (bottom) The phase metrics are calculated by first summing over the enclosed signed Lissajous phase area over the 1st and 2nd half of the frequency spectrum. These are then combined in various ways to produce the different phase metrics.

In the sensitivity study (Section 3.3.3.2) both the amplitude and phase metrics were normalized to the all-bundle case, which was acquired before any removal of bundles in each series of measurements. The amplitude spectra were normalized by dividing that of each

configuration by the all-bundle spectra in each series before the amplitude metrics were calculated. Similarly, the phase spectra were normalized by subtracting that of the all-bundle case in each series before the phase metrics were calculated. Overall, this process helped eliminate the effects from inconsistent bundle-base contacts in between each series of measurements, which enabled statistics to be applied across all the measurements. In particular, the sensitivity of phase metrics was substantially enhanced by normalization, as discussed in more detail in Section 3.4.

3.3.3. RESULTS

3.3.3.1. THE EFFECTS OF INTERNAL CONFIGURATION ON THE AMPLITUDE METRICS

The first study conducted was focused on the effects of different locations and combinations of debris, bundles and empty states. A visual description of the various test configurations can be seen below each horizontal axes of Figure 3.3.3.1.1, as defined in Figure 3.3.1.1(c). The results are from the unnormalized amplitude metrics derived from the trunnion sensor spectra and sorted by the number of intact bundles inside the basket. Several general trends were observed in these metrics. The most significant factor impacting the metrics was the number of bundles. With more intact bundles, less *total energy* and higher *second moments* were measured. On the other hand, the impacts on the metrics of empty slots versus debris filled slots were less prominent than the number of bundles. Similarly, the arrangement of the three states in each configuration had less of an impact on the metrics.

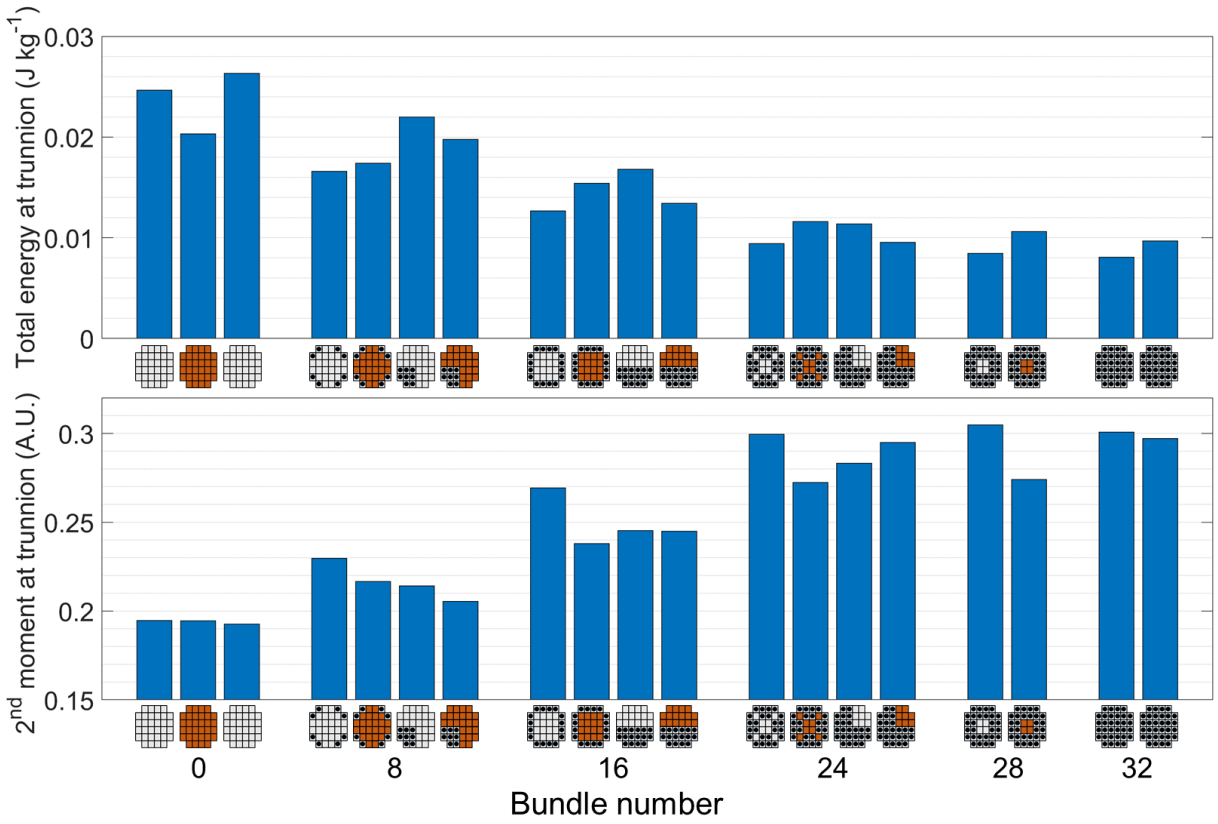

Figure 3.3.3.1.1. The results for the amplitude metrics for the various internal configurations. The configurations are shown below in the horizontal axis and sorted by the number of intact bundles inside the basket. (See Figure 3.3.1.1(c) to interpret the configuration drawings.) The duplicated configurations represent separate measurements. The results are described by the amplitude metrics measured at the trunnion sensor without normalization. With more intact bundles, the *total energy* metric got smaller (top), while the *second moment* metric grew larger (bottom).

In order to provide perspective on how the amplitude metrics correspond to the raw data, the individual amplitude spectra of the symmetrical configurations are shown in Figure 3.3.3.1.2. The area under each curve is an indicator of the measured vibrational energy. The area was observed to decrease in general as the number of bundle-filled slots increased, regardless of whether the rest of slots were filled with debris or empty. The *total energy* metric result in Figure 3.3.3.1.1 reasonably quantified this observation. Compared with the all empty case, the (1, 2) mode shifted down in frequency significantly only when there was an increase in the number of bundles in the basket, while the (2, 1) mode did not shift as significantly in any of the

configurations. The spectra also became much more complex with higher number of bundles. The *second moment* metric result in Figure 3.3.3.1.1 reasonably quantified these observations and agreed with the previous assumption based on the mode shapes that the (1, 2) global bending mode is more sensitive to internal structural change while the (2, 1) radial-with-shearing mode is less sensitive, as far as the amplitude metrics are concerned. However, the *second moment* metric was not sensitive enough to discriminate between the less structured spectra in the debris cases.

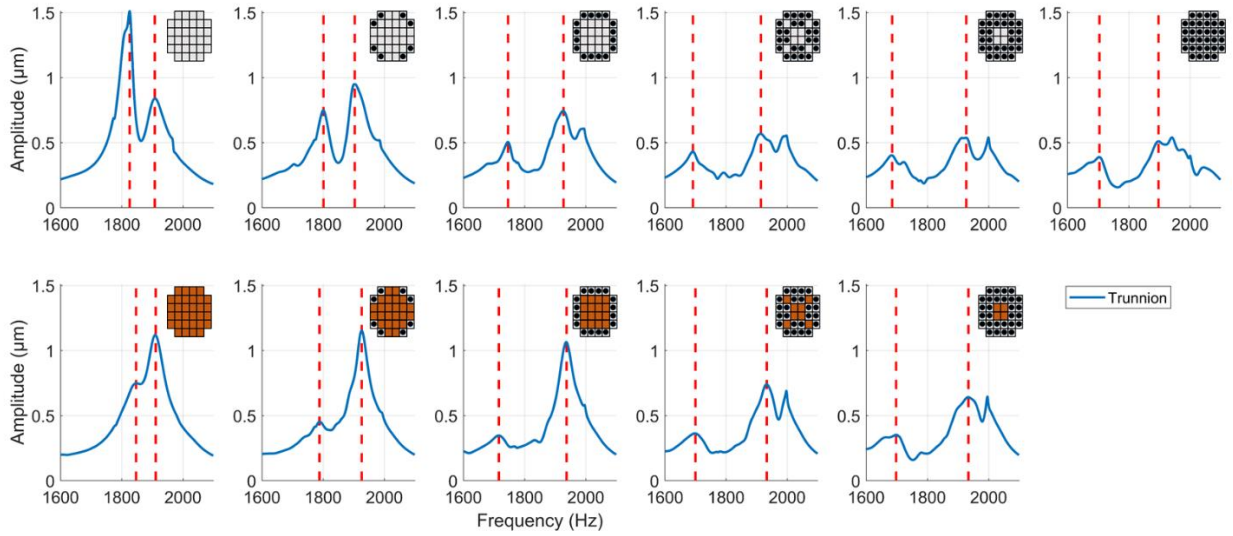

Figure 3.3.3.1.2. The individual amplitude spectra of symmetric configurations measured by the trunnion sensor. The (1, 2) global bending mode, which is lower in frequency, and the (2, 1) radial-with-shearing mode are marked with dashed lines in the spectra. The first row shows the cases with bundles and empty slots, while the second row shows the cases with bundles and debris filled slots.

3.3.3.2. SENSITIVITY OF THE NORMALIZED METRICS

An additional study was conducted to determine the sensitivity of the metrics to the internal configurations in the lab cask. Seven configurations were examined, and they are shown below the horizontal axis in Figure 3.3.3.2.1. This study did not include debris filled cases, focusing

on the single bundle missing cases or otherwise four-fold symmetric configurations. This was explored because it was observed that the metrics were not sensitive to location nor the difference between debris and empty slots, at least for the current methodology. In order to determine the sensitivity of the methodology cases with only a single empty slot were examined. The empty slot was moved around in the bottom-left quadrant with a total of 8 possible locations. However, they did not show significant differences between these locations, so the results of these eight configurations were grouped into one in the figures below. Measurements for each of configurations were performed five times and normalized to the all-bundle case from each individual series as described in the earlier section. In this way, the uncertainties of the all-bundle cases were absorbed into the results for each of the configurations. The resulting normalized amplitude metrics are shown in Figure 3.3.3.2.1. The metrics from both the trunnion and the 90° sensor follow the same general trend as before, except for the 24-missing case in the *second moment* at the 90° sensor. Taking the uncertainties into account, the larger separation of the amplitude metrics when there are more empty slots illustrates that the sensitivity of amplitude metrics is higher in these types of configurations. This agrees with the FEA of the five identified modes of the TN-32 cask loaded with surrogate fuel rods [Section 2.4], in which the rods on the edge of the basket exhibited larger modal amplitudes than the inner rods, thus the enhanced the sensitivity in these locations.

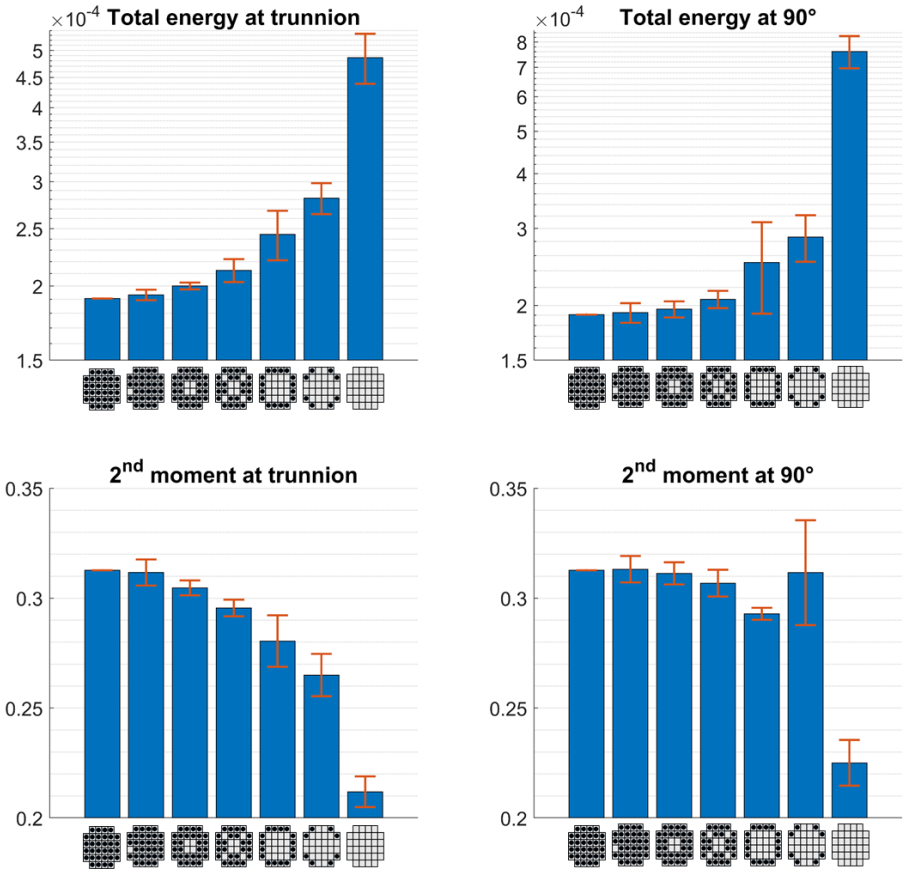

Figure 3.3.3.2.1. The amplitude metrics derived from the sensitivity study normalized by the all-bundle cases. The second configuration in each graph represents all eight single missing bundle cases combined into a single result. Each of the measurements was performed 5 times. The bars represent the average of these measurements and the error bars are the standard deviation. The total energy is plotted in logarithmic scale for visual clarity.

The normalized phase metrics were also calculated for the same configurations. Twelve phase metrics were generated using different combinations of four basic components, the positive or negative summed area in the 1st or 2nd half of the frequency spectrum. There are eight phase metrics which share a similar trend as the amplitude metrics, as shown in Figure 3.3.3.2.2. With the trends observed in metrics involving solely the 1st or 2nd half of the phase spectra, this shows that both the (1, 2) and (2, 1) modes are affected by the internal conditions when considering phase. In particular, four of the phase metrics show a higher sensitivity when there are only a few empty slots (first row of Figure 3.3.3.2.2).

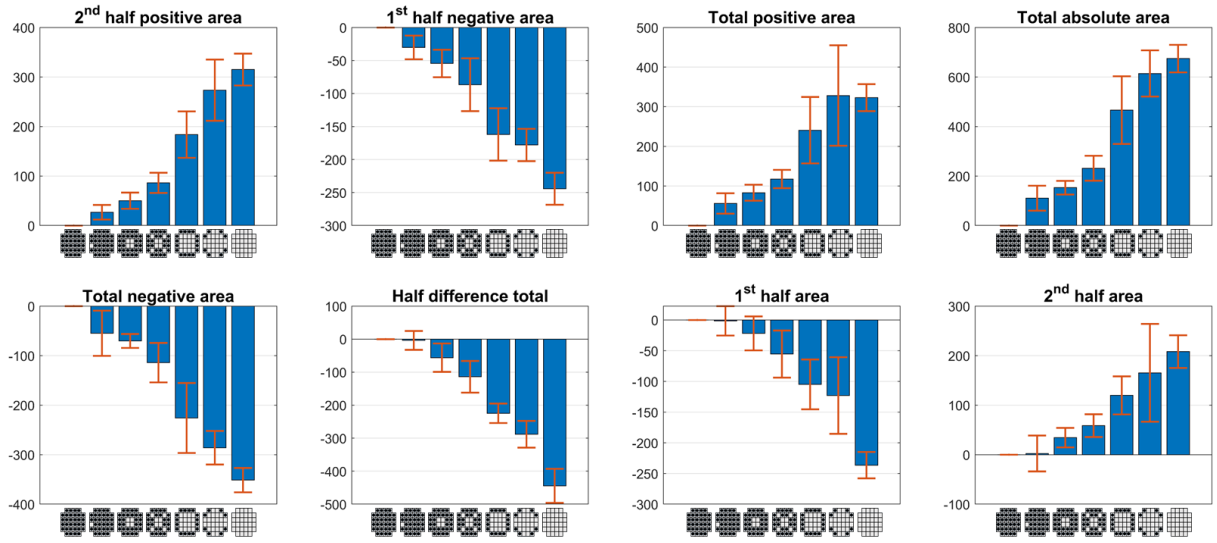

Figure 3.3.3.2.2. The normalized phase metrics derived from the sensitivity study. The positive and negative sums under the phase area curves (see Figure 3.3.2.2(bottom)) were determined over the 1st and 2nd half of the spectra. These four parameters were combined in various ways to produce the eight phase metrics shown above. The same general trend as in the amplitude metrics was observed in these metrics. The four metrics in the top row show higher sensitivity when there are few bundles missing.

Finally, the normalized amplitude can be combined with the four phase metrics into a total of twelve metrics, which are then used to generate a single parameter by Principle Component Analysis (PCA). PCA seeks a linear combination of variables such that the maximum variance is achieved. Then, it seeks a second linear combination which maximize the remaining variance, and so on. These twelve metrics were rescaled to vary between ± 1 before applying PCA. Scores derived from the primary eigenvector in PCA provide the best distinction of the seven scenarios [Figure 3.3.3.2.3]. The coefficients of each metrics for this eigenvector are provided in Table 3.3.3.2.1. With the similarity between the acoustic responses of debris and empty slots, this result shows the proposed methodology has the potential to detect a single empty slot or a bundle that has completely decayed into debris.

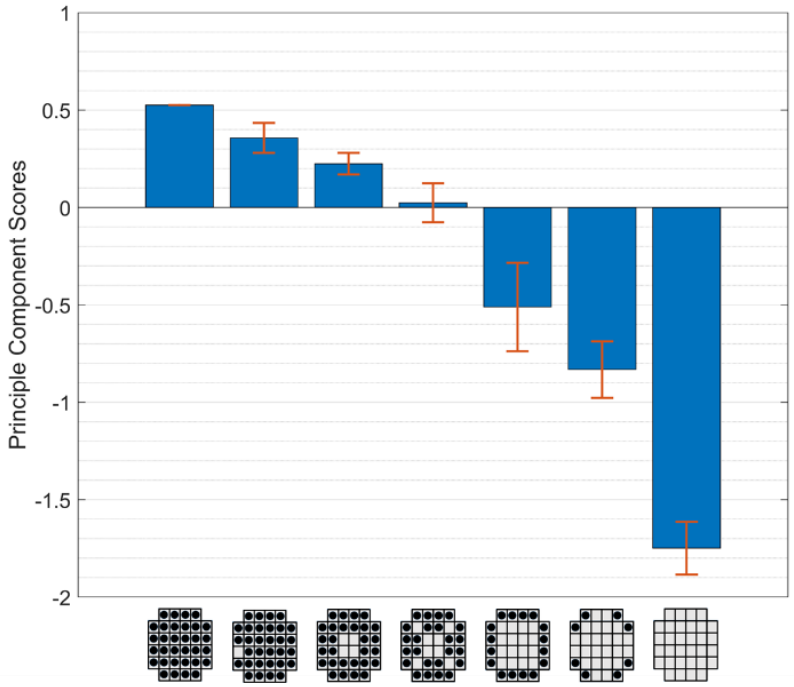

Figure 3.3.3.2.3. The parameter for internal damage based on PCA of the amplitude metrics and four of the phase metrics. This result shows that this approach potentially has sufficient sensitivity to detect variations at the single slot level.

Table 3.3.3.2.1. Coefficients for principle component analysis

Metric	Coefficient
Total energy - sensor 1[3]	0.3299
Total energy - sensor 2	0.3271
2nd moment - sensor 1	-0.382
2nd moment - sensor 2	-0.2434
2nd half positive phase area	0.4161
1st half negative phase area	-0.3891
Total positive phase area	0.2976
Total absolute phase area	0.4073

[3]Sensor 1 refers to the trunnion sensor while sensor 2 refers to the 90° sensor

3.4. DISCUSSION

In the sensitivity study, the amplitude metrics showed higher sensitivity with fewer bundles in the basket, while the phase metrics showed higher sensitivity when the basket is nearly full of bundles. These two independent sets of metrics appear to be complimentary to each other. It is believed that the amplitude metrics describe the modal structure change in the cask modes, while the phase metrics describe the small modulations in the amplitude spectra caused by modal interactions between the cargo and the cask. These modulations are typically largely reflected in the phase spectra. To quantify this feature, the phase metrics were devised based on the variations inside the Lissajous figures. The fact that the enclosed area is proportional to the sine of the relative phase is advantageous in this study. In the frequency range near the (1, 2) and (2, 1) modes, the relative phase between the two sensors will be close to either 0 or π based on their mode shapes. Any deviation from that will result in a non-zero area which is extremized at a quadrature phase. For this reason, the small modulations in the amplitude spectra can be easily picked up. (e.g. the small but sharp peak at around 1980 Hz in the spectrum of the 90° sensor in Figure 3.3.2.2) Similarly, the normalization process can help the phase metrics to further pick up any phase deviation from the all-bundle case. This method is in principle the same as measuring the changes in the mode shapes, so it is expected that the sensitivity of the phase metrics can be further improved by deploying more sensors around the cask.

In Section 3.3.3.1, three general trends were observed. First, when there are more intact bundles in the basket, the *total energy* measured is lower and the *second moment* is higher. Second, the acoustic response is similar regardless of whether slots are filled with debris or empty. Third, the geometric arrangement of the states has minimal impact on the metrics. For the first

two observations, the hypothesis is that only an intact rod bundle inside the basket can be excited acoustically while debris cannot. Intact structures, such as the bundles, will vibrate and thus retain part of the vibrational energy, and the sensors on the outer shell will measure less energy. On the other hand, since the debris or empty slots do not retain significant vibrational energy, there will be more energy remaining on the shell of the cask. For the *second moment*, the (1, 2) mode decreases significantly in resonance frequency only when an intact structure is present in a slot. Therefore, an intact structure can be seen as an effective mass-loading to the (1, 2) mode from a vibrational standpoint. The extra modal structure in the bundle also adds to the complexity of the spectra resulting in an increase in the *second moment*. Regarding the similarity in the acoustic response between configurations in which slots are debris-filled or empty, one can reasonably argue that the debris can still vibrate near the bottom of the cask, and thus is differentiable from an empty slot in theory. It is supposed that the contact area is very small due the aspect ratio of the basket slots so that the actual volume of vibrating shot is negligible compared to the rest of the shot that lies above. Regarding the third observation, although the results did not show significant sensitivity to spatial configuration, it is believed that locations of different states will affect the mode shapes differently and thus with additional sensors, they can still be distinguished by the phase metrics. A plausible explanation for why the data does not show significant distinctions between the response for different locations is that the setup lacks enough spatial resolution in terms of the number and distribution of sensors for the changes of mode shape to be quantified. It is expected that these limitations can be overcome by improving the experimental setup with more sensors and more consistent contacts between the bundles and the base of the cask.

The final parameter for describing the internal condition of the cask was derived from four amplitude and four phase metrics by using PCA. The primary set of PCA scores have a clear trend across all the configurations, and it is the only set that maintains a trend when accounting for uncertainties. The fact that the magnitudes of the primary PCA coefficients [Table 3.3.3.2.1] are comparable for each metric implies that the metrics may be linearly co-dependent. This suggests that the physical origins of the metrics are related. A second dimension of the PCA might be introduced by nonlinear acoustics techniques to differentiate the surface contacts created by the debris case, no contact for the empty case, or even damaged bundles. Some nonlinear acoustics techniques were also attempted in this work. However, the results were inconclusive because the nonlinear effects caused by the structure and junctions of the lab cask elements cannot be eliminated as sources. Extensive studies of the shaker and sensors indicated that the majority of the nonlinearity observed does not come from the measurement system but comes from the cask itself through some unidentified means.

Since the correspondence of the vibrational modes between the TN-32 and lab cask was verified as shown in Section 3.2.4, it is expected that the NDE methodology developed for the lab cask can be potentially applicable on a TN-32 cask. As an example, the acoustic fingerprints of a TN-32 cask, acquired by calculating the metrics, can be established immediately before and after loading with spent fuel assemblies. These fingerprints are crucial for the sensitivity of the metrics as the slight changes in the frequency spectra due to the reassembly of the bottom cask plate between the two internal condition studies were observed. In the extended storage scenario, regular checks can be performed efficiently with a compact and mobile acquisition system consisting of accelerometers, which can be mounted to the TN-32 cask magnetically. If the values

for the metrics fall inside the established bounds for a cask before and after loading, the degree of internal failure can be estimated, and a more sophisticated method can be applied (e.g. neutron tomography). Section 2.3.2 demonstrated the possibility of applying a vibrometric NDE method developed for the storage (vertical) configuration to the transportation (horizontal) configuration. In a TN-32 cask, the fuel assemblies each have their own spring system that rigidly holds the fuel assembly in place against the lid of the cask; therefore, the contacts between the assemblies and the base of the cask are maintained in the horizontal orientation. Thus, the NDE scheme in this work could also be applied to monitor SNF during transportation, which can be more suitable than radiological methods due to the rapidity and compactness of acoustic techniques. Lastly, the sensitivity of the current method is approximately at the level of a complete structural failure of a single bundle. Although further studies on the sensitivity have not been conducted as a part of this study, the current results suggest the potential to detect partial assembly failures. The current sensitivity level may be able to detect a catastrophic fuel assembly damage event during transportation after extended storage, which could potentially lead to nuclear criticality [90]. This approach may provide the basis for a novel tool to address the criticality concern in the transportation of spent fuel assemblies in the extended storage scenario. Moreover, it is expected the same principle can be applied to the NDE of solid cargo in other types of sealed vessels.

3.5. SUMMARY

This chapter describes the efforts to develop an acoustic NDE method that can identify catastrophic failure in the spent fuel assemblies inside a nuclear dry storage cask. A 1:6 scaled

laboratory cask was constructed, and the measured modes agree with those observed in a full-scale TN-32 cask. The (1, 2) global bending and the (2, 1) radial-with-shearing modes were the primary focus of this effort. Three possible states were introduced to each slot of the basket in the cask: an intact bundle, debris or an empty slot. Experiments for different internal configurations were conducted using two accelerometers attached to the cask. Amplitude and phase metrics were developed to assess the internal conditions. The amplitude metrics are related to the measured vibrational energy and its spectral distribution, while the phase metrics quantifies the changes of mode shapes by comparing the relative phases between the two accelerometer signals. The results suggest that an intact bundle will have a complicated modal response, while a debris-filled or empty slot does not extract significant vibrational energy from the cask structure. For the amplitude metrics, the (1, 2) mode is shown to be sensitive to the internal structural integrity, while the (2, 1) mode is relatively insensitive. With the phase metrics, the overall increased complexity in the frequency spectra, which contain both modes, can be further quantified. These metrics can be combined by using PCA, and the derived relation suggests that this methodology has the potential to detect when a single bundle completely decays into debris. This general methodology is expected to be further developed for the use in monitoring for situations that could lead to the nuclear criticality during the transportation of a TN-32 cask. It is possible with more sensors that an even greater sensitivity could be achieved. Furthermore, this method may also be applied to the NDE of solid cargo inside other types of sealed vessels. However, it has limited ability to discern between empty slots and debris-filled slots. To further increase the NDE sensitivity, the efforts for tackling this problem by using nonlinear ARS will be presented in the next chapter.

4. CHARATERIZATION OF SPHERE-PLANE CONTACT LOSS NONLINEARITY

4.1. INTRODUCTION

In the last chapter, metrics were developed to estimate the structural integrity of the mock-up fuel assemblies inside a simplified lab-scale cask using sensors located strictly on the outside surface. For a fully-loaded lab cask with 32 surrogate fuel assemblies, the metrics were capable of detecting decay down to the single assembly level. However, the signatures of a damaged versus missing assembly were not clearly resolved. We expect the contact between the container and the decayed debris will result in nonlinear resonance responses while the absent case will not, which can be exploited to achieve a large increase in sensitivity.

Nonlinear acoustic techniques for NDE have been actively studied in the past few decades. Among these techniques, Nonlinear Resonance Ultrasound Spectroscopy (NRUS) shares many commonalities with ARS. Relevant work of NRUS was reviewed in Section 1.2. However, these efforts only dealt with micro-cracks inside samples. No previous reported NRUS study has been applied to the NDE of solid cargo inside a container. In this case, the main source of nonlinearity will come from the contact between the cargo and the container. Serendipitously, a 1-D NRUS perturbation model developed by Van Den Abeele [41] suggests that NRUS can be potentially applied to other types of nonlinearity. It may also be able to distinguish types of nonlinearity from the shape of the frequency shift versus amplitude curve. Since the application of NRUS in this chapter is similar to the historical development of ARS, we will refer to our particular use of

NRUS as Nonlinear Acoustic Resonance Spectroscopy (NARS), since it is applied to the NDE of the cargo in the audible frequency range.

Contact nonlinearity is also a rich field that has been widely studied for decades under various contexts. This dissertation aims to study the contact nonlinearity between the inner bottom of a cylindrical container and the decayed solid cargo inside, which is simplified to a single layer of identical spheres. Under this premise, the most relevant contact model is the Hertzian model, which describes the force law between two spherical surfaces. Compared to the works reviewed in Section 1.3.2 [60,61], this system consists of a single layer of spheres evenly distributed at the bottom of an open cylinder. These multiple sphere-plane contacts are not imposed by any static pressure other than their own weight, and the mass of the spheres are small compared to the cylinder. Therefore, these contacts can be treated as perturbation to the resonance modes of the cylinder. Consequently, the resonance behavior in this system is expected to be different from the literature. In this scenario, contact loss immediately happens with excitations, and it can lead to a *clapping mechanism*. Contact Acoustic Nonlinearity (CAN) was proposed to model *breathing cracks* and *clapping mechanism* and is reviewed in Section 1.3.1. A single-mode approximation of CAN [51] was used in this chapter to model the contact loss.

This chapter aims to provide basic knowledge for differentiating between an empty container and a debris-filled one by using NARS. The simplified system in this chapter is an open-end cylinder made from a single piece of aluminum to eliminate any extra nonlinearity due to assembly. The cylinder was evenly filled with a single layer of identical spheres of various compositions and radii to simulate decayed solid cargo. The sphere-plane contact nonlinearity

was characterized by NARS with an excitation source and a sensor located at the outer surface on the opposite sides of the cylinder. The mode of choice is the (1, 2) global bending mode. Since it has relatively large response at the contact surface compared to nearby modes, this mode is expected to achieve better sensitivity. Based on the experiment results, a phenomenological model was proposed by combining the 1-D NRUS formalism and contact models, and then it was implemented in FEA to compare with the experimental results.

The remainder of this chapter is organized as follows. In Section 4.2, 1-D phenomenological NARS models on Hertzian contact and contact loss are derived, and the latter was proposed based on the experimental observations. In Section 4.3, the materials, the NARS experimental technique and the associated data analysis are presented. In Section 4.4, the details on the implementation of the proposed NARS model in FEA are described. In Section 4.5, the experimental results are presented and compared to FEA. This is followed by the discussion in Section 4.6, and a summary in Section 0.

4.2. 1-D NONLINEAR ACOUSTIC RESONANCE SPECTROSCOPY MODEL FOR CONTACTS

Following the 1-D NRUS formalism given by Van Den Abeele [41], we can expand the formalism to an arbitrary type of nonlinear model as long as it has a converging Taylor expansion and is small compared to the internal elastic force in the material. To give a quantitative description, a free 1-D bar with length L [Figure 4.2.1] is a good starting point for its simplicity. A nonlinear contact is introduced as a boundary condition at the top of the bar. The boundary

condition is treated as a perturbation to the free-free longitudinal bar solution. Assume the equation of motion has this form:

$$\rho\partial_{tt}u = K\partial_{xx}u + \delta(x)\frac{f^{\mathrm{NL}}(u)}{S} = K\partial_{xx}u + \frac{\delta(x)}{S}\sum_{m=1}^{\infty} F_m u^m \qquad (4.2.1)$$

where $u(x,t)$ is the dynamic displacement, K is the relevant elastic constant (Young's modulus in this case), S is the contact boundary surface area (cross-section of the bar in this case), and $\delta(x)$ is the Dirac delta function that imposes the nonlinear dynamic force $f^{\mathrm{NL}}(u)$ at the $x = 0$ surface.

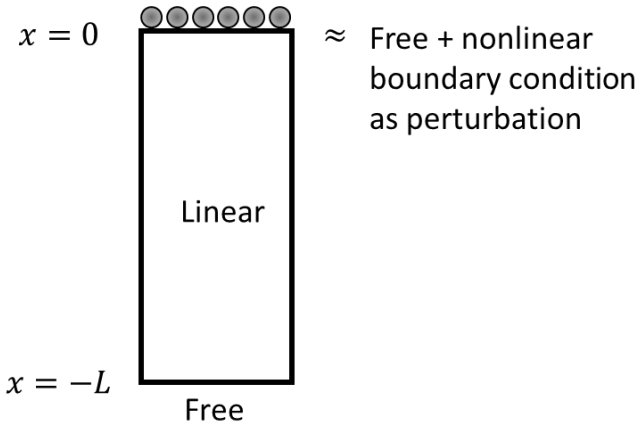

Figure 4.2.1. Schematic of a simplified 1-D theoretical model of NARS for contact nonlinearity. The contact nonlinearity is modeled as a perturbative boundary condition applied on the longitudinal vibration of a linear elastic bar.

The function $f^{\mathrm{NL}}(u)$ is of arbitrary nonlinear type that is simplified to be only a function of the dynamic displacement. It is assumed to be small compared to the internal elastic force in the material. The Taylor expansion coefficients of $f^{\mathrm{NL}}(u)$ are $\{F_m\}$ and the static terms are set to zero. Assuming the system is driven at a single frequency close to the n^{th} mode, $u(x,t)$ is expressed using the n^{th} normal mode of the unperturbed wave equation ($\{F_m\} = \{0\}$):

$$u(x,t) = \psi_n(x) z_n(t) \tag{4.2.2}$$

Where $\psi_n(x) = \cos\left(\frac{n\pi x}{L}\right)$ and $z_n(t)$ are mode shape and temporal functions of the n^{th} mode respectively. Substituting Eq. (4.2.2) into the equation of motion in Eq. (4.2.1), multiplying both sides with $\psi_n(x)$, and integrating over the length of the bar L yields:

$$\partial_{tt} z_n + {\omega_n}^2 z_n = \sum_{m=1}^{\infty} \frac{2F_m}{\rho L S} {z_n}^m \tag{4.2.3}$$

where $\omega_n = \frac{n\pi}{L}\sqrt{\frac{K}{\rho}}$ is the unperturbed resonance frequency, and the mode shape function $\psi_n(0) = 1$ is used. For each of the perturbation terms, only the 1st order terms resulting from the fundamental of the n^{th} mode are kept. Next, it is assumed the temporal function $z_n(t)$ is reasonably close to an unperturbed solution:

$$z_n(t) = A\cos(\Omega_n \mathrm{t}) \tag{4.2.4}$$

where Ω_n is the perturbed resonance frequency. The term ${z_n}^m$ is expressed as a Fourier series in order to find the contribution to the n^{th} fundamental mode:

$$\begin{aligned} {z_n}^m &= A^m \cos^m(\Omega_n \mathrm{t}) \\ &= \begin{cases} \dfrac{A^m}{2^{m-1}} \displaystyle\sum_{k=(m+1)/2}^{m} \binom{m}{k} \cos[(2k - m)\Omega_n t] & \text{for odd } m \\ \dfrac{A^m}{2^{m-1}} \binom{m}{\frac{m}{2}} + \dfrac{A^m}{2^{m-1}} \displaystyle\sum_{k=\frac{m}{2}+1}^{m} \binom{m}{k} \cos[(2k - m)\Omega_n t] & \text{for even } m \end{cases} \end{aligned} \tag{4.2.5}$$

The cosines with integer multiples of the resonance frequency show that the nonlinearity generates harmonics. Since cosines are orthogonal functions, the higher harmonic terms can be discarded as they will not affect the fundamental terms. Note that the Fourier series of even

power cosines does not have a contribution to the fundamental term. Rewriting Eq. (4.2.5) with only the fundamental contributions from the nonlinear terms:

$$-{\Omega_n}^2 + \left({\omega_n}^2 - \frac{2F_1}{\rho LS}\right) = \sum_{m=3,5,7\ldots}^{\infty} \frac{F_m}{2^{m-2}\rho LS}\left(\frac{m}{\frac{(m+1)}{2}}\right)A^{m-1} \tag{4.2.6}$$

The perturbed resonance frequency can be written as:

$$\begin{aligned}\Omega_n &= \sqrt{{\omega_n}^2 - \frac{2F_1}{\rho LS} - \sum_{m=3,5,7\ldots}^{\infty} \frac{F_m}{2^{m-2}\rho LS}\left(\frac{m}{\frac{(m+1)}{2}}\right)A^{m-1}} \\ &\approx \sqrt{{\omega_n}^2 - \frac{2F_1}{\rho LS}}\left\{1 - \frac{1}{{\omega_n}^2 + \frac{2F_1}{\rho LS}} \sum_{m=3,5,7\ldots}^{\infty} \frac{F_m}{2^{m-1}\rho LS}\left(\frac{m}{\frac{(m+1)}{2}}\right)A^{m-1}\right\}\end{aligned} \tag{4.2.7}$$

When $A = 0$ (linear), the resonance frequency is changed due to the 1st order term from the arbitrary nonlinear function $f^{\mathrm{NL}}(u)$. When $A > 0$ (nonlinear), each term in the Taylor expansion of $f^{\mathrm{NL}}(u)$ affects the frequency shift by different powers of the displacement amplitude at the contact surface. Theoretically, we can measure the resonance frequency shift due to increasing amplitude and quantify the shape of the resonance frequency versus amplitude curve by fitting it with a polynomial. With the relative ratio between the polynomial coefficients, we may be able to discern a different type of nonlinearity introduced in the same resonant system by the shape of frequency shift curve. This can potentially be used as an NDE technique, although determining the local displacement amplitude A will require a full 3-D solution. This can be solved numerically through FE simulations.

In this chapter, the interest is in the contact nonlinearity between the spherical payload and the container. The Hertzian contact model is an appropriate candidate for the nonlinear

boundary condition and will be studied first (See Section 1.3.2 for an extensive review). The Hertzian force-displacement law for a sphere-sphere contact gives:

$$\widetilde{f^{\mathrm{H}}}(\tilde{u}) = -\frac{4E^*\sqrt{R^*}}{3}\tilde{u}^{\frac{3}{2}} \tag{4.2.8}$$

where $\widetilde{f^{\mathrm{H}}}(\tilde{u})$ is the total Hertzian force, $\tilde{u}$ is the total displacement, E^* is the contact modulus and R^* is the reduced radius of curvature. These two quantities are related to the physical properties of the two spheres:

$$\frac{1}{E^*} = \frac{1-{\nu_1}^2}{E_1} + \frac{1-{\nu_2}^2}{E_2}, \tag{4.2.9}$$

$$\frac{1}{R^*} = \frac{1}{R_1} + \frac{1}{R_2} \tag{4.2.10}$$

where E_1 and E_2 are the Young's modulus, and ν_1 and ν_2 are the Poisson's ratios for the individual spheres. For a sphere-plane contact, $R_2 = 0$, so $R^* = R_1 \equiv R_s$. For multiple spheres at the contact surface, they can be treated as parallel nonlinear springs. Assuming the spheres in the single layer are packed in a hexagonal lattice, the total Hertzian force at the boundary is:

$$\widetilde{f^{\mathrm{H}}}(\tilde{u}) = -N\frac{4E^*\sqrt{R_s}}{3}\tilde{u}^{\frac{3}{2}} \approx -\frac{S\sqrt{3}}{2{R_s}^2}\frac{4E^*\sqrt{R_s}}{3}\tilde{u}^{\frac{3}{2}} = -\frac{2SE^*}{\sqrt{3}{R_s}^{3/2}}\tilde{u}^{\frac{3}{2}} \tag{4.2.11}$$

where N is the number of spheres and S equals to the surface area of the inner bottom of the container in this case. To use the NARS formalism, a Taylor expansion needs to be applied for small oscillations around an equilibrium displacement [99]. Because there is no other external static force besides gravity on the spheres, the equilibrium displacement u_0 can be calculated by equating the weight and Hertzian force on a single sphere:

$$\frac{4}{3}\pi {R_s}^3 \rho_s g = \frac{4E^*\sqrt{R_s}}{3} {u_0}^{\frac{3}{2}} \quad \Longrightarrow \quad u_0 = \left(\frac{\rho_s g \pi}{E^*}\right)^{\frac{2}{3}} {R_s}^{\frac{5}{3}} \tag{4.2.12}$$

where ρ_s is the density of the sphere. Expanding Eq. (4.2.11) around u_0 yields:

$$\begin{aligned}
\widetilde{f^{\mathrm{H}}}(\tilde{u}) &= -\frac{2SE^*}{\sqrt{3}{R_s}^{\frac{3}{2}}}(u_0+u)^{\frac{3}{2}} \\
&= -\frac{2SE^*}{\sqrt{3}{R_s}^{\frac{3}{2}}} {u_0}^{\frac{3}{2}} \left[1 + \sum_{p=1}^{\infty} \frac{1}{p!}\left(\frac{3}{2}\cdot\frac{1}{2}\cdot\frac{-1}{2}\cdots\frac{(5-2p)}{2}\right)\left(\frac{u}{u_0}\right)^p\right] \\
&= -\frac{2SE^*}{\sqrt{3}{R_s}^{3/2}} {u_0}^{\frac{3}{2}} \left[1 + \sum_{p=1}^{\infty} \frac{1}{p!}\left(\frac{u}{2u_0}\right)^p \prod_{j=1}^{p}(5-2j)\right]
\end{aligned} \tag{4.2.13}$$

Taking the dynamic term and using the definition in Eq. (4.2.1) yields:

$$\begin{aligned}
F_m^{\mathrm{H}} &= -\frac{SE^* {u_0}^{\frac{3}{2}-m}}{m!\, 2^{m-1}\sqrt{3}{R_s}^{\frac{3}{2}}} \prod_{j=1}^{m}(5-2j) \\
&= -\frac{S\rho_s g\pi}{m!\, 2^{m-1}\sqrt{3}} \left(\frac{E^*}{\rho_s g\pi}\right)^{\frac{2m}{3}} {R_s}^{1-\frac{5m}{3}} \prod_{j=1}^{m}(5-2j)
\end{aligned} \tag{4.2.14}$$

where Eq. (4.2.12) is used to substitute u_0 in order to obtain the last expression. Plugging these Hertzian contact expansion coefficients into Eq. (4.2.7) will yield the NARS frequency shift expression for Hertzian contact. Despite the intimidating expression, there are two important characteristics. First, the odd terms of F_m^{H} for $m > 3$ are all positive, so the Hertzian frequency shift monotonically decreases as shown in Figure 4.2.2(left), and this feature qualitatively agrees with the literature in which a prestressed plane-sphere-plane experimental setup was used [61]. Second, the same terms are inversely proportional to R_s of different powers. These two characteristics will be compared with the experiment results.

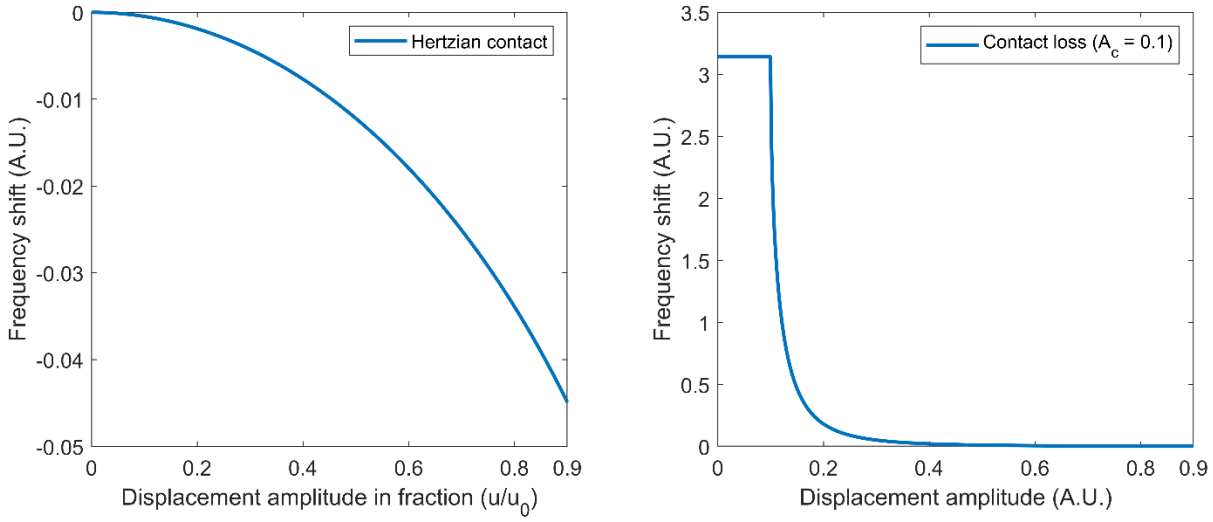

Figure 4.2.2. The numerical results from a 1-D (left) Hertzian contact model and (right) a contact loss model. The Hertzian model result is plotted with the first ten non-zero terms in the Taylor expansion, and the value diverges when the displacement amplitude approaches the static displacement.

Intuitively, Hertzian sphere-plane contact model should be appropriate to describe our system of interest. However, according to FEA, even the smallest practical excitation level in the experiments induce acceleration larger than the acceleration due to gravity at the contact surface, and thus the spheres will experience contact loss, which cannot be described by the above model. Here, we propose a phenomenological model that can sufficiently explain our experimental results, although the exact physical picture of the model is still unclear. Based on the experimental results, the condition at the boundary can be modeled as an effective restoring force $f^{\mathrm{C}}(u)$ that is proportional to the total mass M of the spheres inside. This approach is motivated by the contact loss of an *added mass* boundary condition. In this case, however, the effective mass is negative mathematically, so it's more natural to write it in terms of effective stiffness. Using the single-mode approximation of CAN [51], the contact loss will happen during part of the vibration cycle when the displacement u goes beyond a critical amplitude A_{c}.

$$f^{\mathrm{C}}(u) \equiv \begin{cases} -\gamma(-M)a(u) = -\gamma M {\Omega_n^{\mathrm{C}}}^2 u & \text{when } |u| \le A_c \\ 0 & \text{when } |u| > A_c \end{cases} \tag{4.2.15}$$

where γ is a constant of proportionality, Ω_n^{C} is the perturbed resonance frequency for contact loss and $a(u)$ is the acceleration. Since this expression is linear in u, the fundamental Fourier coefficient from the nonlinear contribution only involves F_1^{C}. However, it is required to be recalculated due to the incomplete vibration cycles by the definition of F_1^{C} in Eq. (4.2.1):

$$\begin{aligned} F_1^{\mathrm{C}} &= \frac{\Omega_n^{\mathrm{C}}}{\pi} \int_0^{\frac{2\pi}{\Omega_n}} \frac{f^{\mathrm{C}}(u(0,t))}{A} \cos \Omega_n t \, dt \\ &= \frac{-\gamma M {\Omega_n^{\mathrm{C}}}^2}{\pi} 2 \int_{\arccos\left(\frac{A_c}{A}\right)}^{\pi - \arccos\left(\frac{A_c}{A}\right)} (\cos t')^2 \, dt' \end{aligned} \tag{4.2.16}$$

where change of variable $t' \equiv \Omega_n^{\mathrm{C}} t$ was used. Evaluating the integral yields:

$$F_1^{\mathrm{C}} = \frac{-\gamma M {\Omega_n^{\mathrm{C}}}^2}{\pi} (\pi - 2\theta_c - 2\cos\theta_c \sin\theta_c) \tag{4.2.17}$$

$$\text{where } \theta_c \equiv \begin{cases} \arccos\left(\frac{A_c}{A}\right) & \text{when } A > A_c \\ 0 & \text{when } A \le A_c \end{cases}$$

Replacing F_1^{C} in Eq. (4.2.7) with Eq. (4.2.17), the perturbed resonance frequency for contact loss Ω_n^{C} becomes:

$$\begin{aligned} \Omega_n^{\mathrm{C}} &= \sqrt{{\omega_n}^2 - \frac{2F_1^{\mathrm{C}}}{\rho L S}} \approx \omega_n \left(1 - \frac{F_1^{\mathrm{C}}}{\rho L S {\omega_n}^2}\right) \\ &= \omega_n \left(1 + \frac{\gamma M}{\pi \rho L S} \frac{{\Omega_n^{\mathrm{C}}}^2}{{\omega_n}^2} (\pi - 2\theta_c - 2\cos\theta_c \sin\theta_c)\right) \end{aligned}$$

$$\approx \omega_n \left(1 + \frac{\gamma M}{\pi \rho L S} (\pi - 2\theta_c - 2\cos\theta_c \sin\theta_c) \right) \qquad (4.2.18)$$

The numerical resonance frequency shift curve of a contact loss 1-D model is plotted in Figure 4.2.2(right) above.

4.3. MATERIALS AND EXPERIMENTAL METHODS

Experiments were conducted to study the contact nonlinearity between the decayed cargo and its container. The experimental setup is shown in Figure 4.3.1. A cylindrical aluminum container, which is closed at one end, was machined as a single piece to eliminate any inherent contact nonlinearity due to assembly (OD: 4", ID: 3", height: 7.4", bottom thickness: 0.5", mass: 1.8 kg). The container with the payload was placed on a piece of packaging foam (5 cm thickness) to reduce contact nonlinearity between the table and the container. Two cuts on the top opposite sides of the container were made to facilitate the mounting of an excitation source and a sensor. A shaker (Dayton DAEX32U-4, 40W, 8Ω) was glued with the pre-attached 3M VHB adhesive on one side, and a single-axis accelerometer (Kistler Type 8614A1000M1) was attached with cyanoacrylate adhesives on the other side. The shaker was connected to a power amplifier (TECHRON Model 5507) which was connected to the sine-out port of the lock-in amplifier (Stanford Research Systems SR850). The accelerometer was connected through a signal amplifier (Kistler Dual Mode Charge Amplifier Type 5010) to the input of the lock-in amplifier. To monitor the temperature of the container, a thermocouple (OMEGA Type E) was attached to the outer surface of the container with electrical tape and was connected to a digital multimeter (Keithley

2700). The lock-in amplifier and the multimeter were controlled using a laptop with a custom LabVIEW interface.

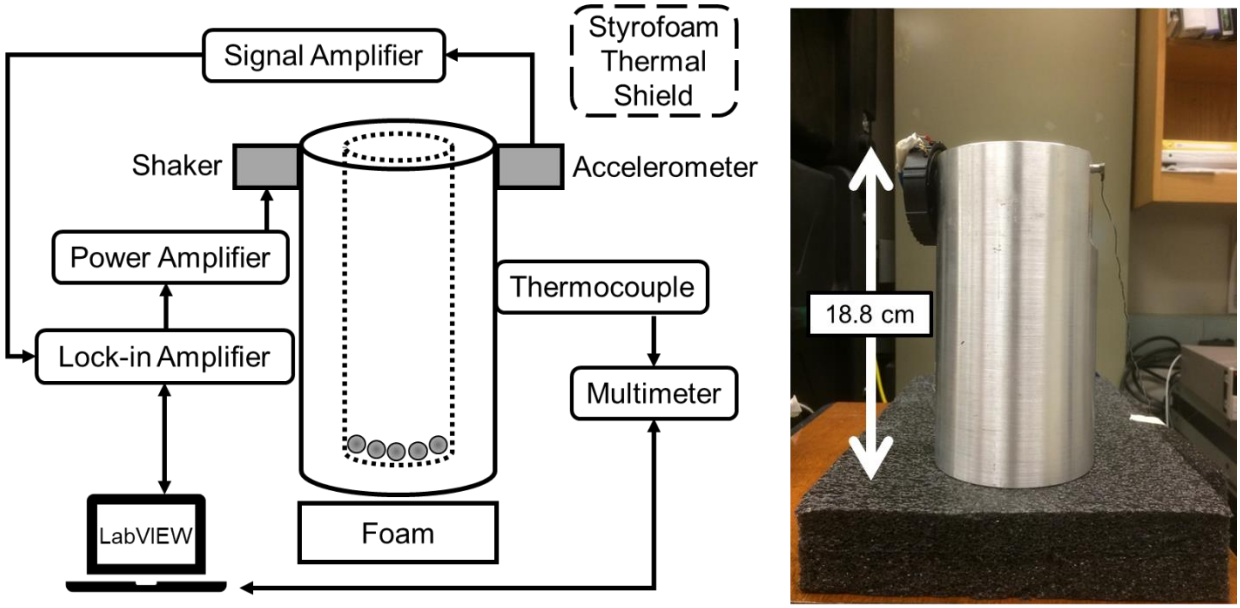

Figure 4.3.1. (a) A schematic diagram and (b) a photograph of the NARS experimental setup.

The inner bottom of the container was evenly sanded with 600-grit sandpaper on a spinning disk. Spheres of different diameters and materials were introduced in a single layer to mimic debris at the bottom of the container. Table 4.3.1 lists the materials, radii and total masses of the single layer spheres at the bottom of the container. By shaking the container manually, the spheres nearly filled up of the bottom area of the cylinder in a hexagonal pattern without creating horizontal stress between the spheres. The number of spheres was maintained each time they were repositioned. This study is sensitive to gradual changes in temperature as it introduces a systematic error in the resonance frequency shift. A Styrofoam box was used to cover the container to provide a layer of insulation from thermal fluctuations in the room. The temperature of the container was found to fluctuate less than 0.5 °C during one data acquisition with the layer

of insulation in place. Measurements were also spread out during different times of the day to average out the systematic error due to gradual cooling and heating inside the laboratory.

Table 4.3.1. List of materials, radii and total masses of a single layer of spheres at the bottom of the container

Material	Diameter (mm)	Total mass (g)
440C stainless steel ball (McMaster-Carr)	2.0	41.0
	3.0	60.8
	4.0	79.7
	6.0	112.6
Zinc-plated steel BB (Daisy)	4.5	88.5
Copper-plated lead shot	3.0	86.9
Glass bead	5.0	31.2

The shaker was driven using sine wave input linearly swept in increasing frequency. The resonance mode of interest is the (1, 2) global bending mode which was identified with guidance from FEA using COMSOL Multiphysics simulation package. The (1, 2) mode was chosen because its shape has a relatively large amplitude at the bottom of the container with respect to other nearby modes [inset of Figure 4.3.2] as discovered in a similar system in Section 2.4. This mode shape also has minimum local bending near where the shaker was mounted, so this mode is expected to introduce minimum contact nonlinearity at the surface between the shaker and the container while achieving maximum sensitivity for the contact nonlinearity at inner bottom surface of the cylinder. The frequency sweeps were repeated with different shaker driving voltages from 0.2 V to 0.4 V in 0.02 V increments and from 0.4 V to 2.0 V in 0.2 V increments.

These amplitude ranges were chosen so that the spectra were stable and had reasonable amplitude resolution in the lower driving amplitude range where the resonance frequency changed rapidly. For each driving amplitude, the frequency sweep was repeated three times to stabilize the system, and the last frequency spectrum was recorded for offline signal processing. The payload was repositioned a total of 5 times to get the statistics on the contact consistency. The recorded spectra were fit to a Lorentzian function to extract resonance frequencies and their amplitudes. The resonance frequency versus amplitude was plotted for each driving amplitude and then fit to a model-derived equation [Figure 4.3.2]. The experimental resonance frequency versus resonance amplitude data exhibited shallower transition than the phenomenological model described in the last part of Section 4.2. Using only the first nonlinear term in the model, the following equation gives the best fit:

$$f_{\mathrm{res}} = a(\pi - 2\theta_c) + bA + c \tag{4.3.1}$$

$$\text{where } \theta_c \equiv \begin{cases} \arccos\left(\dfrac{A_c^{\mathrm{top}}}{A}\right) & \text{when } A > A_c^{\mathrm{top}} \\ 0 & \text{when } A \le A_c^{\mathrm{top}} \end{cases}, \qquad A_c^{\mathrm{top}} \equiv 10\ nm$$

where f_{res} is the resonance frequency for contact loss, and $\{a, b, c\}$ are the fitting parameters. Note that A_c^{top} is the effective critical displacement based on the measurements at the cut on the top side surface of the cylinder, which is simply assumed to be proportional to the critical displacement at the contact surface at the bottom of the cylinder. In addition, it was derived from a phenomenological model, so it is not meant to be treated as an actual physical displacement. The choice of A_c^{top} was fit by hand to provide the best-match to all results from the various

spheres. The higher harmonics are not reported here because the harmonic spectra lack a well-defined modal structure.

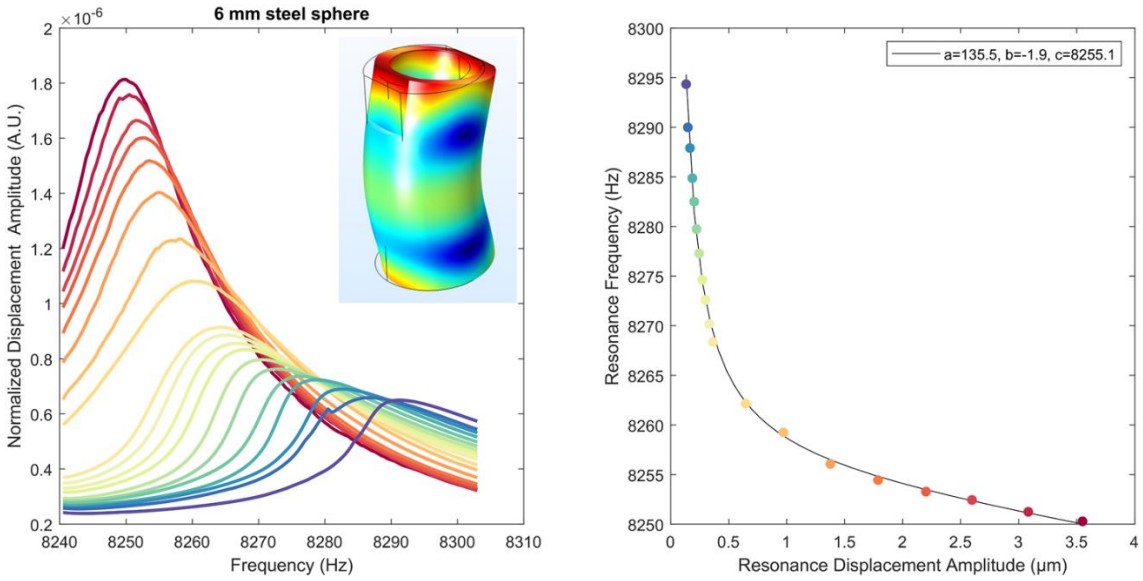

Figure 4.3.2. An example of data processing for the 6 mm sphere data. (left) The normalized frequency spectra on the left-hand side are fit with a Lorentzian function and (right) the resonance frequency versus resonance amplitude data are fit with an equation derived from the phenomenological NARS contact loss model. The frequency spectra are normalized with respect to the individual driving voltage for visual clearance.

4.4. FINITE ELEMENT SIMULATIONS

Frequency sweeps of the contact loss nonlinearity can be simulated using FEA. The geometry of the aluminum container was imported to the COMSOL Multiphysics software package. The contact was modeled at the inner bottom boundary using the *spring foundation* boundary condition. The nonlinear contact force law derived in Eq. (4.2.17) was implemented as a total spring constant k_z and it is assumed to act only in the normal direction,

$$k_z(x, y, z_0) = |F_1^C| = \frac{\gamma M \Omega_n^{C\,2}}{\pi}(\pi - 2\theta_c - 2\cos\theta_c \sin\theta_c) \tag{4.4.1}$$

$$\text{where } \theta_c \equiv \begin{cases} \arccos\left(\frac{A_c}{A_z}\right) & \text{when } A_z > A_c \\ 0 & \text{when } A_z \leq A_c \end{cases}, \quad A_c \equiv 0.05\ \mu m$$

where $A_z(x, y, z_0)$ is the local normal displacement amplitude at the contact boundary surface $z = z_0$. The total mass of the spheres M were directly measured and the physical properties of the container were taken from the material datasheet for Aluminum 6063-T83 ($\rho = 2700\ \mathrm{kg/m^3}$, $E = 69\ \mathrm{GPa}$, $\nu = 0.33$, and isotropic loss factor $\eta = 0.02$). The effective critical amplitude A_c was chosen so that the simulations give the best-match with the experiments. Frequency sweeps were simulated with various driving forces which result in similar normal acceleration ranges as measured in the experiments. This corresponds to normal strain levels between 10^{-7} and 10^{-6} at the contact surface, estimated by the simulations. The recorded spectra were fit to a Lorentzian function to extract resonance frequencies and their amplitudes. The simulated resonance frequency versus resonance amplitude curve was then acquired.

4.5. RESULTS

For all types of spheres used in this work, a common behavior of the resonance shift was observed. At low driving amplitude, the resonance frequencies of the loaded cases were significantly higher than the unloaded (i.e. unperturbed) case. With increasing driving amplitude, the resonance frequencies of the loaded cases rapidly decreased at first and then slowly approached the resonance frequencies of the unloaded case as the driving amplitude continued to rise to large levels [Figure 4.3.2]. This phenomenon was modeled as an effective contact loss stiffness at the boundary with the stiffness approaching zero when the driving amplitude is high. The comparison between FEA and experiments is shown in Figure 4.5.1(right). Because there is a

mismatch between the experimental and simulated unperturbed resonance frequencies, frequency shift curves were used, which were calculated by using the resonance frequency difference referenced to the highest driving amplitude. This example was simulated to match the total frequency shift of the 6 mm steel sphere data shown in the Figure 4.3.2, and γ was identified to be 3.2 in this case. The resemblance between the FEA and experimental frequency shift curves show that a simple NARS contact loss phenomenological model is able to match the experiments to a reasonable degree. There are two major experimental observations for which the model does not give satisfying descriptions. First, the normalized frequency spectra for the experimental case had significant changes in the shape with different amplitudes [Figure 4.3.2 (left)], while the simulated ones remained similar [Figure 4.5.1(left)]. Second, the simulated frequency shift curve shows much steeper transition than the experimental curve fit [Figure 4.5.1(right)].

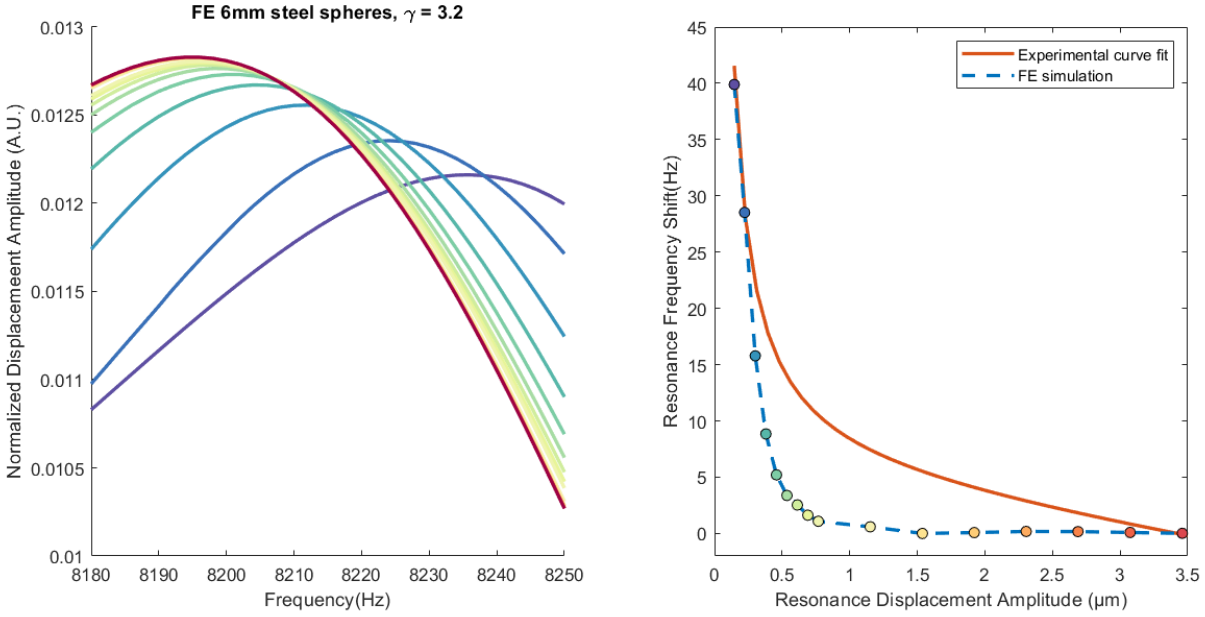

Figure 4.5.1. FE simulation of 6mm steel sphere case. (left) The normalized frequency spectra on the left-hand side are fit with a Lorentzian function and (right) the simulated resonance frequency versus resonance amplitude data are compared to the fit in Figure 4.3.2.

The changes of nonlinear resonance of the container due to the materials and radii of the spheres were studied. The frequency shift curves were calculated for each case and are shown in Figures Figure *4.5.2* and Figure *4.5.3*. By doing this, resonance frequency offsets due to reconfiguring and temperature changes can be eliminated, which enables comparisons between the studies. The uncertainties can be estimated solely using the fitting parameters between different runs. This is because the predominant cause of uncertainty was identified to be the repositioning of the spheres inside the container. Comparatively, the uncertainties from the data collection system and data analysis are negligible. The frequency shifts for the spheres are significantly larger than the empty configuration, so the inherent nonlinear effects from the data collection system can be ruled out as the main contributor.

To examine the effect of sphere size on the nonlinear response, the frequency shift curves for the 400C stainless-steel sphere of four different diameters are plotted in Figure 4.5.2. The curves for each diameter can be normalized by dividing the curve by the total mass of the spheres contained. The resulting normalized curves collapse into the same curve within the bounds of uncertainty except for the 2 mm case. In order to study the effects of material type on the nonlinear response, spheres of four different materials were tested. The frequency shift curves for spheres made of 400C stainless-steel, lead, BB and glass are plotted in Figure 4.5.3. Although the diameters between spheres of various materials are different, the total masses are similar with the exception of the glass beads [Table 4.3.1]. With the normalization to total mass, the frequency shift curves again collapse into a single curve within the uncertainty limits. To match the simulated frequency shift curves with the experimental average curves for all materials and diameters excluding 2mm steel spheres, γ falls in the range between 2.4 and 2.9.

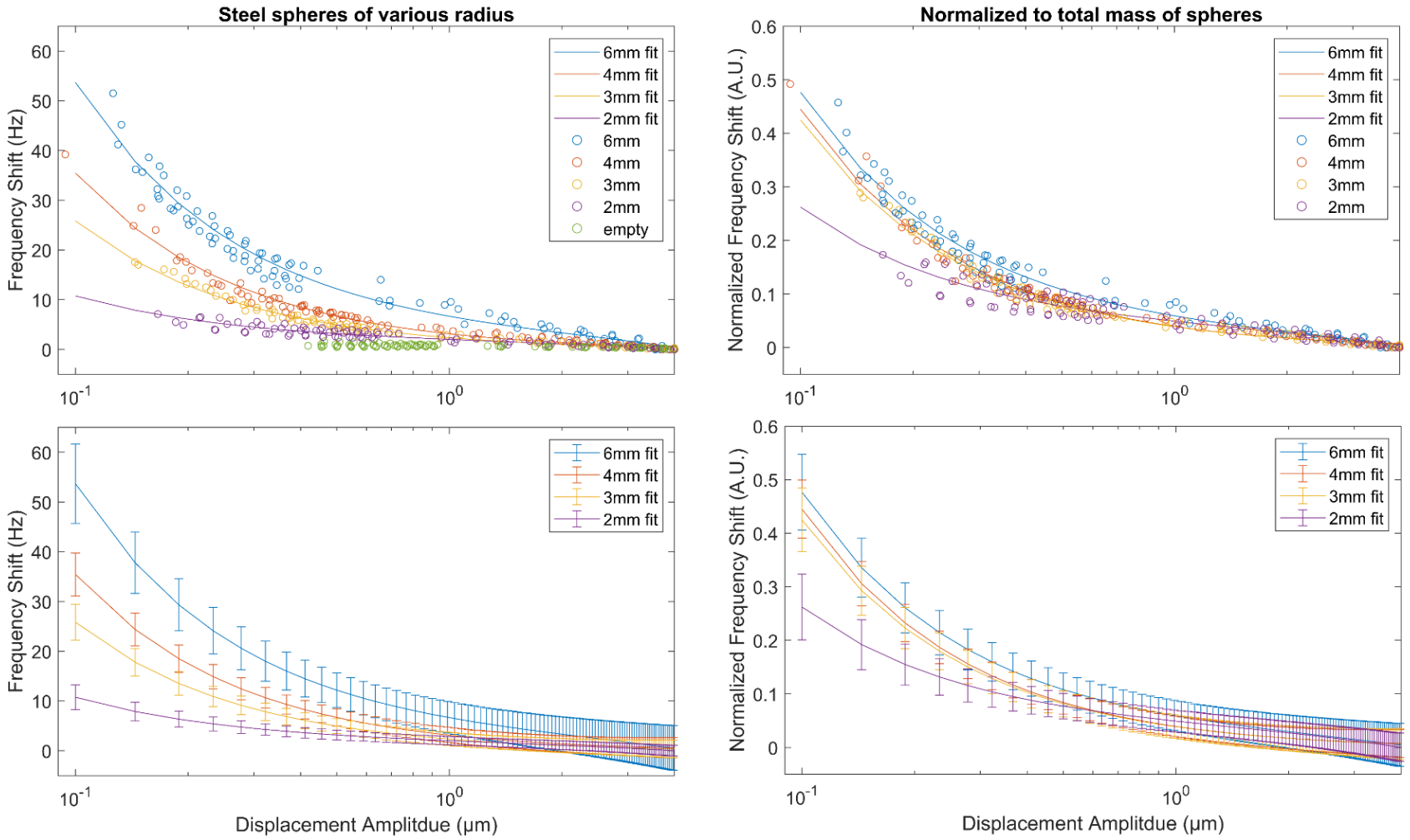

Figure 4.5.2. Comparison of the frequency shift curves between spheres of same material (400C stainless steel) but different diameters. The right plots are normalized to the total mass of the spheres in the container, while the left plots are unnormalized. The top plots are the scatter plots from all five runs for each diameter, and the fitted curves are plotted using the mean parameters from the five individual fits. The bottom plots are the fitted curves plotted with error bars. The error bars are the upper and lower bounds of the fitted curve values calculated by using the mean parameter values plus or minus one standard deviation. The empty case is plotted in the top left plot for reference. The frequency axis is plotted on a logarithmic scale for clarity.

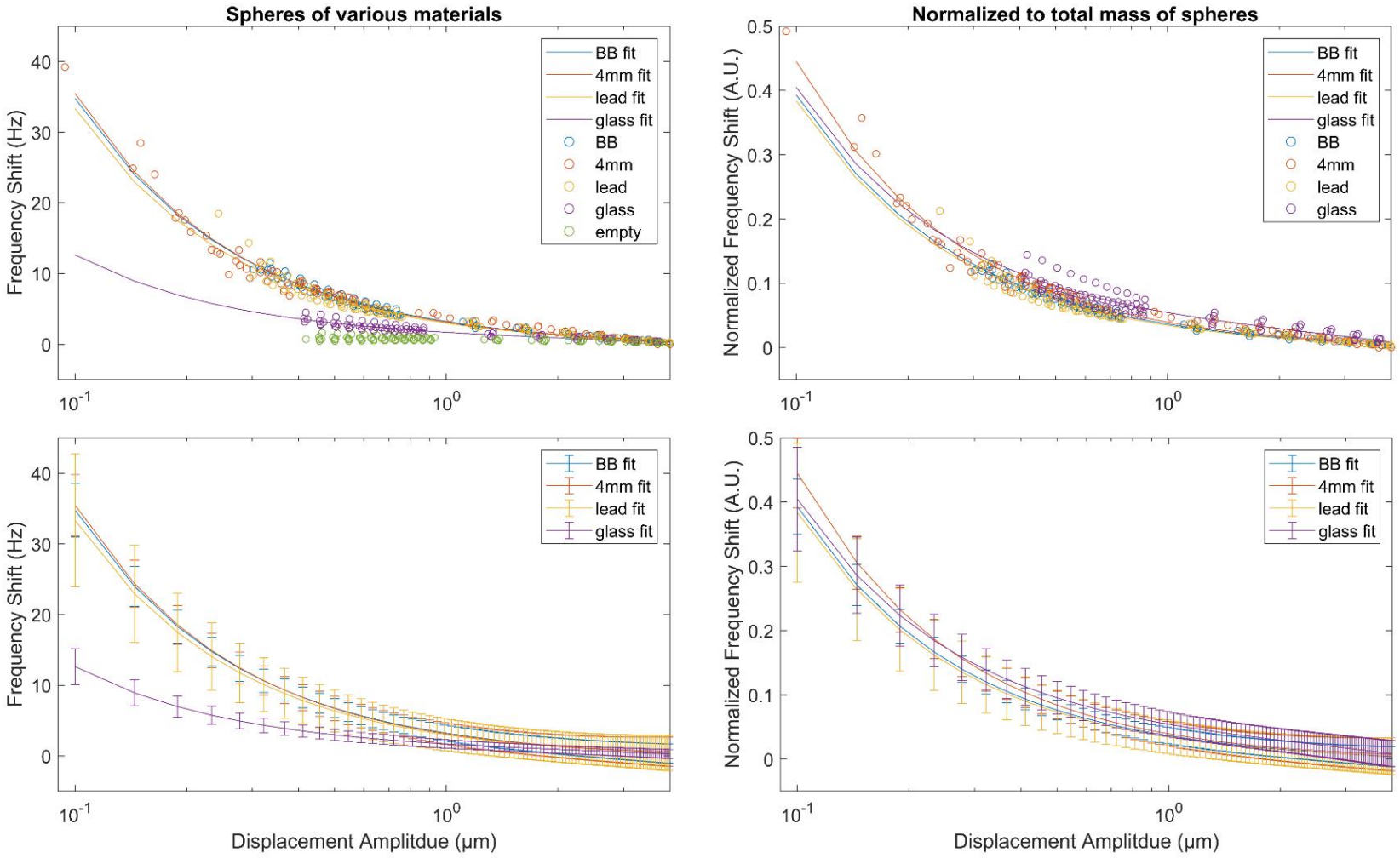

Figure 4.5.3. Comparison of the frequency shift curves between spheres of different materials. The 4 mm data set is the same as in Figure 4.5.2, and the results are presented in the same manner.

4.6. DISCUSSION

The effective critical displacement at the top side surface A_c^{top} in Eq. (4.3.1) was fit by hand to maintain better convergence over all the configurations. On one hand, this can introduce some uncertainties in the results; on the other hand, the uncertainties caused by each repositioning the spheres were much larger than the uncertainty introduced by hand-fitting. Thus, the error from hand-fitting the experimental curves is tolerable until a more consistent repositioning method is applied. The most likely cause of the repositioning uncertainty is the inconsistency in the number of spheres in the area with larger modal displacement. Unlike a piston motion where every location has the same displacement amplitude, in the (1, 2) mode, the bottom of the cylinder vibrates against a nodal line that goes through the diameter perpendicular to the driver-sensor axis. The edges away from the nodal line at the inner bottom reach maximum displacement amplitude while the nodal line exhibits minimum amplitude, so the edges are expected to induce more contact loss. In the same area, the spheres will have the least consistency in position and number, because the hexagonal pattern is difficult to maintain at the edge of circles by manual shaking, especially for spheres with a larger radius. Therefore, the collective acoustic response of the spheres at the inner bottom can result in large errors due to the inconsistency of the effective number of spheres located at the edges. In Figure 4.5.2, the absolute uncertainty increases with the radius of the spheres, which agrees with this conjecture.

Originally, this work began with the aim of studying the perturbative effects on a cylinder mode due to plane-sphere-plane Hertzian contacts. However, the experiment results showed that a different kind of contact nonlinearity than that was reported in the literature was encountered. Another solid aluminum cylinder (diameter $d = 7\ cm$, height $h = 8.5\ cm$ and

polished to 30-µm roughness by South Bay Model 920 polisher) was placed on top of the single layer spheres. The results were very similar to Figures Figure *4.5.2* and Figure *4.5.3* except that there was to much noise in the frequency spectra to be able to identify modes in in higher amplitudes. Removing the spheres such that the solid aluminum cylinder was in direct contact with the container bottom introduced less than half of the frequency shifts in comparison to the 2 mm steel sphere case, and the curve shape was nearly linear. These facts suggest the nonlinearity was mainly contributed from the contact between the spheres and the container. The size of frequency shifts measured for the various sphere were proportional to the total mass M or radius R_s of the sphere, since $M \propto N\frac{4\pi}{3}{R_s}^3 \propto \frac{1}{{R_s}^2}{R_s}^3 = R_s$, where N is the total number of the spheres. However, for the Hertzian model, the plane-sphere contact is expected to introduce a frequency shift curve of negative powers of R as seen from Eq. (4.2.14). This is almost a reciprocal behavior compared with the experimental results in this work. With all the above observations and the fact that rattling noises were observed in the experiments with high amplitudes, the predominating physical mechanism is assumed to be contact loss rather than Hertzian contact. In addition, the frequency shift versus amplitude curve obtained in this work behaves like a hyperbola of positive curvature representative of a contact loss nonlinearity, while the curve for a plane-sphere-plane contact reported in the literature [61] behaves similarly to an even order polynomial with negative curvature. The Hertzian results derived in Section 4.2 also agree with the literature. The main difference between the experiments in this work and the results in the literature lies in the ratio of dynamic-to-static force on the vibrating sphere being comparable in this work but less than 7% in the literature. This suggests the nonlinear behavior

reported in the literature were predominately Hertzian-type with some minor contact loss, while the nonlinear behaviors in this work were almost entirely due to the contact loss effect.

The exact physical picture of this contact loss phenomenon is still unclear. The experimental results suggest that the factors which affect the shape of the mass-independent frequency shift curve could originate from a pure kinematic process, while the size of frequency shift involves a dynamic process and is proportional to the total mass of spheres inside the container. These processes do not seem to depend on the material nor the surface finish of the spheres, nor on the diameter when it is above a certain threshold (i.e. the 2 mm case). The assumption is that a sphere detaches from the container surface once the local downward acceleration is greater than that of gravity (kinematic), and it transfers impact momentum (dynamic) to the container when it lands. The proposed phenomenological model provides a reasonable description of the frequency shift curve from the experimental results. However, the first main discrepancy is that the frequency shift curves of the simulated results had a steeper transition than the experimental ones [Figure 4.5.1(right)]. One possible explanation is due to the mode shape discrepancy between the experiments and simulations. Due to the complex boundary conditions, the experiments may be subject to larger local nonlinear damping at the contact surface, so amplitudes at the bottom may not increase linearly with the ones at the top edge. Thus, the experimental frequency shift curve transitions are shallower. Second, comparing the spectra in Figure 4.3.2(left) with Figure 4.5.1(left), the model does not explain how the shape of the resonance spectra changes with the driving amplitude. Studies with finer control are required to further investigate this mechanism.

The work in the chapter has implications for several NARS applications. First, the unique frequency shift curve for contact loss, which is different from the even order polynomial curve from the Hertzian model and the linear shift from a hysteretic model, implies that NARS has the potential to distinguish different types of nonlinearity inside a system simply by observing the features of the frequency shift curve. The no-contact case is also straightforward to identify because it exhibits a minimum frequency shift. Second, regarding the NDE of solid cargo inside a container, a contact loss model is more appropriate to describe the nonlinear behavior at the contact surface. Even with the spheres loaded by the static pressure of the extra cylinder that filled up to 70% of the container (described earlier in this section), the nonlinear response is still of the contact loss type and far from the Hertzian regime. Practically, it is rare to have a debris-filled container with extremely high static pressure or to apply a very low excitation amplitude to reach the Hertzian regime in a noisy environment. Third, the experimental results suggest that the NARS techniques have the potential to estimate the average debris mass inside the container. Combining with the metrics developed for intact cargo in Chapter 3, the proportion of the intact cargo may be estimated first, and then the rest of the cargo may be differentiated between being absent or decayed. If the rest of it is decayed, the average mass of the decayed debris may be estimated. The work in this chapter is expected to serve as a foundation for further development of the NDE applications on solid cargo inside sealed vessels.

4.7. SUMMARY

This chapter aims to study the contact nonlinearity between a single layer of identical spheres and the inner bottom of an aluminum cylindrical container by using NARS. As a function of driving amplitude, the frequency shift of the (1, 2) global bending mode is significantly larger than the empty case, and its hyperbolic shape is unique compared to the Hertzian model and the hysteretic model found in the literature. The frequency shift curves can be normalized to the total mass of the spheres and collapse into the same curve within the uncertainty limits, regardless of the surface finish, composition and radius (within a certain range) of the spheres. A phenomenological model was developed to describe the experimental results based on a 1-D NRUS formalism with a contact loss model. The contact loss of a sphere was modeled as a nonlinear spring at the contact boundary, which provides a perturbation to a linear resonance mode. The spring constant is proportional to the mass of the sphere, and the value becomes zero when the instantaneous displacement is above a critical value. Next, this boundary condition was applied to the inner bottom of the container cylinder in FEA. The agreement between the experimental and FE results are reasonable considering the simplicity of the model. The proportional constants γ in the spring constant for each type of sphere were estimated, and the error is within 20%. The physical mechanism may be related to the constant detachment of the spheres from the cylinder floor and their impact on reattachment. Studies with finer control are required to confirm this hypothesis. The work in this chapter is expected to provide some basic NDE knowledge for estimating the average mass of decayed solid cargo inside a container, or even further identifying the type of contact nonlinearity that exists inside a system.

5. CONCLUSION

This dissertation demonstrates the potential of applying linear and nonlinear ARS to the NDE of solid cargo inside sealed cylindrical containers of various sizes and complexity. For a cylindrical container as massive and complicated as a TN-32 cask in Chapter 2, ARS is capable of identifying resonance modes with the assistance of FEA. Among these modes, the (1, 2) global bending mode was identified to potentially have a higher sensitivity to internal structural changes because of its large inner bottom surface to external surface amplitude ratio. Further FEA on a TN-32 cask loaded with simulated fuel assemblies supported this result and provided a numerical foundation for the structural health monitoring of these fuel assemblies. The modal correspondence between the storage and transportation scenarios broaden the application range of the ARS technique, especially when the transportation of high burn-up fuel will be required in the foreseeable future. These results are expected to serve as a baseline measurement for future NDE efforts on TN-32 casks.

To study possible damage scenarios inside a nuclear storage cask, a 1:6 scaled lab cask based on a TN-32 cask was manufactured and studied in Chapter 3. Resonance modes were identified both experimentally and numerically. They agreed with the modes measured from the TN-32 cask, suggesting that the lab cask is a reasonable acoustic representation of the TN-32 cask. Thus, the NDE method developed for the lab cask can possibly be applied on a full-scale TN-32 cask. Utilizing the (1, 2) global bending mode and the (2, 1) radial-with-shearing mode, two novel

sets of amplitude and phase metrics based on ARS were developed to quantify the structural integrity of the mock-up fuel assemblies inside. These metrics are sensitive to the complete decay or the absence of 1 of the 32 mock-up assemblies inside the lab cask. This NDE methodology is expected to be applied not only to the spent fuel assemblies inside a full-scale TN-32 cask under both storage and transportation configuration, but also to other types of cylindrical containers with solid cargo inside. However, this method has limited ability to differentiate between an empty and a debris-filled slot as well as the location of these anomalies. The damage localization problem is expected to be solved through high spatial resolution mode shape (phase) measurements, which is possible with more sensors deployed around the cask. The differentiation between an absent and completely decayed cargo can be further improved by resorting to nonlinear acoustic techniques.

To differentiate between an empty and debris-filled container, NARS studies on contact nonlinearity were conducted in Chapter 4. In a simple 20 cm-tall cylinder with an open end, NARS was capable of measuring significant resonance frequency shift as a function of resonance amplitude with a single layer of spheres present on the floor of the cylinder. The characteristics of the frequency shift curves were drastically different from the Hertzian contact model results derived from NARS formalism in Section 4.2. A contact loss phenomenological model was developed and implemented in FEA, and the FEA results agreed with the experiments reasonably. The size of frequency shift measured from NARS can be used to estimate the total mass of the spheres inside the container, regardless of the material and radius (above a certain threshold). These results demonstrated a proof-of-concept of using NARS as a complementary method to the ARS metrics described in Chapter 3.

In order to improve ARS and NARS as novel NDE tools for solid cargo inside a sealed cylindrical container, some future work can be conducted to (1) better understand the physical origin of the contact loss nonlinearity described in Chapter 4, (2) demonstrate the capability of NARS to distinguish different types of nonlinearity (e.g., Hertzian contact vs. contact loss) in the same system, (3) evaluate the feasibility to apply NARS on systems with inherent nonlinearity (e.g., the lab cask), (4) improve the damage localization ability of the ARS metrics in Chapter 3 with high spatial resolution phase/mode shape measurements, and finally with the previous points well-studied, (5) apply the ARS and NRUS methods to a full-scale TN-32 cask.

LIST OF REFERENCES

[1] Introduction to Nondestructive Testing, Am. Soc. Nondestruct. Test. (n.d.). https://asnt.org/MajorSiteSections/Learn/Introduction_to_Nondestructive_Testing.aspx.

[2] S.W.S. Doebling, C.R.C. Farrar, M.B.M. Prime, D.W.D. Shevitz, Damage identification and health monitoring of structural and mechanical systems from changes in their vibration characteristics: a literature review, 1996. doi:10.2172/249299.

[3] E.P. Carden, P. Fanning, Vibration Based Condition Monitoring: A Review, Struct. Heal. Monit. An Int. J. 3 (2004) 355–377. doi:10.1177/1475921704047500.

[4] O.S. Salawu, Detection of structural damage through changes in frequency: a review, Eng. Struct. 19 (1997) 718–723. doi:10.1016/S0141-0296(96)00149-6.

[5] K.L. Rens, P.E. Terry, Review of nondestructive evaluation techniques of civil infrastructure, J. Perform. Contructed Facil. 11 (1997) 152–160.

[6] P.C. Chang, A. Flatau, S.C. Liu, Review Paper: Health Monitoring of Civil Infrastructure, Struct. Heal. Monit. An Int. J. 2 (2003) 257–267. doi:10.1177/1475921703036169.

[7] J.M.W. Brownjohn, Structural health monitoring of civil infrastructure, Philos. Trans. R. Soc. A Math. Phys. Eng. Sci. 365 (2007) 589–622. doi:10.1098/rsta.2006.1925.

[8] M.G. Srinivasan, C.A. Kot, Effect of damage on the modal parameters of a cylindrical shell, in: Int. Modal Anal. Conf., San Diego, CA (United States), 1992. https://www.osti.gov/servlets/purl/10118296.

[9] Y. Zhang, S.T. Lie, Z. Xiang, Q. Lu, A frequency shift curve based damage detection method for cylindrical shell structures, J. Sound Vib. 333 (2014) 1671–1683. doi:10.1016/j.jsv.2013.11.026.

[10] M. Amabili, Theory and experiments for large-amplitude vibrations of empty and fluid-filled circular cylindrical shells with imperfections, J. Sound Vib. 262 (2003) 921–975. doi:10.1016/S0022-460X(02)01051-9.

[11] M.A. Haroun, Vibration studies and tests of liquid storage tanks, Earthq. Eng. Struct. Dyn. 11 (1983) 179–206. doi:10.1002/eqe.4290110204.

[12] M.R. Kruntcheva, Free Vibrations of Cylindrical Storage Tanks : Finite-Element Analysis and

Experiments, J. Eng. Mech. 133 (2007) 728–733.

[13] M. Amiri, Ambient vibration test and finite element modeling of tall liquid storage tanks, Thin Walled Struct. 49 (2011) 974–983. doi:10.1016/j.tws.2011.03.008.

[14] H. Takahara, K. Kimura, Frequency response of sloshing in an annular cylindrical tank subjected to pitching excitation, J. Sound Vib. 331 (2012) 3199–3212. doi:10.1016/j.jsv.2012.02.023.

[15] L. Cheng, J. Nicolas, Free vibration analysis of a cylindrical shell-circular plate system with general coupling and various boundary conditions, J. Sound Vib. 155 (1992) 231–247. doi:10.1016/0022-460X(92)90509-V.

[16] M. Zhao, J. Zhou, Review of seismic studies of liquid storage tanks, 5 (2018) 557–572.

[17] D.N. Sinha, Acoustic resonance spectroscopy (ARS), IEEE Potentials. 11 (1992) 10–13. doi:10.1109/45.127718.

[18] R.S. Roberts, J.T. Chen, O.A. Vela, P.S. Lewis, Munitions classification using an acoustic resonance spectroscopic technique, in: Proc. 27th Asilomar Conf. Signals, Syst. Comput., 1993: pp. 991–995 vol.2. doi:10.1109/ACSSC.1993.342421.

[19] R.S. Roberts, P.S. Lewis, O.A. Vela, A pattern recognition algorithm for the blind discrimination of liquid and solid filled munitions, in: Conf. Rec. Twenty-Ninth Asilomar Conf. Signals, Syst. Comput., 1995: pp. 1310–1314 vol.2. doi:10.1109/ACSSC.1995.540911.

[20] W. Han, D.N. Sinha, K.N. Springer, D.C. Lizon, Noninvasive Measurement of Acoustic Properties of Fluids Using an Ultrasonic Interferometry Technique, in: R.E. Green (Ed.), Nondestruct. Charact. Mater. VIII, Springer, 1998: pp. 393–399. doi:10.1007/978-1-4615-4847-8.

[21] D. Yan, S.A. Neild, B.W. Drinkwater, NDT & E International Modelling and measurement of the nonlinear behaviour of kissing bonds in adhesive joints, NDT E Int. 47 (2012) 18–25. doi:10.1016/j.ndteint.2011.12.003.

[22] O. Buck, W.L. Morris, J.M. Richardson, Acoustic harmonic generation at unbonded interfaces and fatigue cracks, Appl. Phys. Lett. 33 (1978) 371–373. doi:10.1063/1.90399.

[23] C. Payan, T.J. Ulrich, P.Y. Le Bas, T. Saleh, M. Guimaraes, Quantitative linear and nonlinear resonance inspection techniques and analysis for material characterization: Application to concrete thermal damage., J. Acoust. Soc. Am. 136 (2014) 537. doi:10.1121/1.4887451.

[24] D. Dutta, H. Sohn, K. a. Harries, P. Rizzo, A Nonlinear Acoustic Technique for Crack Detection in Metallic Structures, Struct. Heal. Monit. 8 (2009) 251–262. doi:10.1177/1475921709102105.

[25] M. Muller, D. Mitton, M. Talmant, P. Johnson, P. Laugier, Nonlinear ultrasound can detect accumulated damage in human bone, J. Biomech. 41 (2008) 1062–1068. doi:10.1016/j.jbiomech.2007.12.004.

[26] K.Y. Jhang, Nonlinear ultrasonic techniques for non-destructive assessment of micro damage in material: A Review, Int. J. Precis. Eng. Manuf. 10 (2009) 123–135. doi:10.1007/s12541-009-0019-y.

[27] T. Kundu, ed., Nonlinear Ultrasonic and Vibro-Acoustical Techniques for Nondestructive Evaluation, Springer, 2018. doi:10.1007/978-3-319-94476-0.

[28] K.H. Matlack, J.Y. Kim, L.J. Jacobs, J. Qu, Review of Second Harmonic Generation Measurement Techniques for Material State Determination in Metals, J. Nondestruct. Eval. 34 (2015). doi:10.1007/s10921-014-0273-5.

[29] P.A. Johnson, J.A. TenCate, R.A. Guyer, K.E.A. Van Den Abeele, Resonant Nonlinear Ultrasound Spectroscopy, US Patent 6330827, 2001.

[30] L. Pieczonka, A. Klepka, A. Martowicz, W.J. Staszewski, Nonlinear vibroacoustic wave modulations for structural damage detection: an overview, Opt. Eng. 55 (2015) 011005. doi:10.1117/1.OE.55.1.011005.

[31] D. Broda, W.J. Staszewski, A. Martowicz, T. Uhl, V. V. Silberschmidt, Modelling of nonlinear crack-wave interactions for damage detection based on ultrasound - A review, J. Sound Vib. 333 (2014) 1097–1118. doi:10.1016/j.jsv.2013.09.033.

[32] K.E.-A. Van Den Abeele, J. Carmeliet, J.A. Ten Cate, P.A. Johnson, Nonlinear Elastic Wave Spectroscopy (NEWS) Techniques to Discern Material Damage, Part II: Single-Mode Nonlinear Resonance Acoustic Spectroscopy, Res. Nondestruct. Eval. 12 (2000) 31–42. doi:10.1080/09349840009409647.

[33] J. Chen, J.-Y. Kim, K.E. Kurtis, L.J. Jacobs, Theoretical and experimental study of the nonlinear resonance vibration of cementitious materials with an application to damage characterization, J. Acoust. Soc. Am. 130 (2011) 2728. doi:10.1121/1.3647303.

[34] K. Van Den Abeele, P.Y. Le Bas, B. Van Damme, T. Katkowski, Quantification of material nonlinearity in relation to microdamage density using nonlinear reverberation

spectroscopy: Experimental and theoretical study., J. Acoust. Soc. Am. 126 (2009) 963–72. doi:10.1121/1.3184583.

[35] I.T. Perez-Miravete, C. Campos-Pozuelo, A. Perea, Nonlinear nonclassical elasticity applied to the analysis of low frequency flexural vibrations: theory and experiments., J. Acoust. Soc. Am. 125 (2009) 1302–1309. doi:10.1121/1.3075595.

[36] M. Muller, A. Sutin, R. Guyer, M. Talmant, P. Laugier, P.A. Johnson, Nonlinear resonant ultrasound spectroscopy (NRUS) applied to damage assessment in bone, J. Acoust. Soc. Am. 118 (2005) 3946. doi:10.1121/1.2126917.

[37] S. Haupert, S. Guérard, F. Peyrin, D. Mitton, P. Laugier, Non destructive characterization of cortical bone micro-damage by nonlinear resonant ultrasound spectroscopy, PLoS One. 9 (2014). doi:10.1371/journal.pone.0083599.

[38] K. Zacharias, E. Balabanidou, I. Hatzokos, I.T. Rekanos, A. Trochidis, Microdamage evaluation in human trabecular bone based on nonlinear ultrasound vibro-modulation (NUVM), J. Biomech. 42 (2009) 581–586. doi:10.1016/j.jbiomech.2008.12.018.

[39] S.M. Young, B.E. Anderson, S.M. Hogg, P. Le Bas, M.C. Remillieux, Nonlinearity from stress corrosion cracking as a function of chloride exposure time using the time reversed elastic nonlinearity diagnostic, J. Acoust. Soc. Am. 145 (2019). doi:10.1121/1.5087828.

[40] a. Novak, M. Bentahar, V. Tournat, R. El Guerjouma, L. Simon, Nonlinear acoustic characterization of micro-damaged materials through higher harmonic resonance analysis, NDT E Int. 45 (2012) 1–8. doi:10.1016/j.ndteint.2011.09.006.

[41] K. Van Den Abeele, Multi-mode nonlinear resonance ultrasound spectroscopy for defect imaging: an analytical approach for the one-dimensional case., J. Acoust. Soc. Am. 122 (2007) 73–90. doi:10.1121/1.2735807.

[42] X. Teng, X. Guo, L. Luo, D. Zhang, Solutions of Non-Classical Nonlinear Acoustics Wave Equation in a Conical Bar with Micro-Cracks, Acta Acust. United with Acust. 102 (2016) 341–346. doi:10.3813/AAA.918950.

[43] J.U.P.L.E. Bas, P. Johnson, B. Young, L.A. National, P.L.E. Bas, P. Johnson, 複数モード非線形共鳴超音波スペクトロスコピーを 用いた閉じたき裂の位置特定 Localization of Closed Cracks Using Multi-Mode Nonlinear Resonant, (n.d.) 571–578.

[44] X. Liu, Z. Dao, J. Zhu, W. Qu, X. Gong, K. Van Den Abeele, L. Ma, Localization of material defects using nonlinear resonant ultrasound spectroscopy under asymmetric boundary

conditions, Phys. Procedia. 3 (2010) 55–61. doi:10.1016/j.phpro.2010.01.008.

[45] R. a. Guyer, P. a. Johnson, Nonlinear Mesoscopic Elasticity: Evidence for a New Class of Materials, Phys. Today. 52 (1999) 30. doi:10.1063/1.882648.

[46] P.A. Johnson, B. Zinszner, P.N.J. Rasolofosaon, Resonance and elastic nonlinear phenomena in rock, J. Geophys. Res. Solid Earth. 101 (1996) 11553–11564. doi:10.1029/96JB00647.

[47] R.A. Guyer, K.R. McCall, G.N. Boitnott, Hysteresis, discrete memory, and nonlinear wave propagation in rock: A new paradigm, Phys. Rev. Lett. 74 (1995) 3491–3494. doi:10.1103/PhysRevLett.74.3491.

[48] Chapter 3 Basics, in: SR830 Lock-in Amplif. Man., Stanford Research System, 2011.

[49] I.Y. Solodov, N. Krohn, G. Busse, CAN: an example of nonclassical acoustic nonlinearity in solids, Ultrasonics. 40 (2002) 621–625. doi:10.1016/S0041-624X(02)00186-5.

[50] D. Donskoy, A. Sutin, A. Ekimov, Nonlinear acoustic interaction on contact interfaces and its use for nondestructive testing, NDT E Int. 34 (2001) 231–238. doi:10.1016/S0963-8695(00)00063-3.

[51] M.I. Friswell, J.E.T. Penny, Crack Modeling for Structural Health Monitoring, Struct. Heal. Monit. An Int. J. 1 (2002) 139–148. doi:10.1177/1475921702001002002.

[52] J.A. Williams, R.S. Dwyer-Joyce, Contact between surfaces, in: Eng. Tribol., Cambridge University Press, Cambridge, 2005: pp. 73–131. doi:10.1017/CBO9780511805905.004.

[53] J.A. Greenwood, J.B.P. Williamson, Contact of nominally flat surfaces, Proc. R. Soc. London. Ser. A. Math. Phys. Sci. 295 (1966) 300–319. doi:10.1098/rspa.1966.0242.

[54] J. Rivi, G. Renaud, S. Haupert, M. Talmant, P. Laugier, Probing Interface Elastic Nonlinearity Applying Nonlinear Resonance Ultrasound Spectroscopy: The Case of Screw Tightness-of-fit, (2009).

[55] C. Inserra, V. Tournat, V. Gusev, Characterization of granular compaction by nonlinear acoustic resonance method Characterization of granular compaction by nonlinear acoustic, (2008). doi:10.1063/1.2931088.

[56] I.Y. Belyaeva, V.Y. Zajtsev, L.A. Ostrovskij, Nonlinear acousto-elastic properties of granular media, Akust. Zhurnal. 39 (1993) 25–32. https://www.scopus.com/inward/record.uri?eid=2-s2.0-

0027259813&partnerID=40&md5=4127587c3762ec1bba3125a73a908aa2.

[57] I.Y. Belyaeva, L.A. Ostrovsky, E.M. Timanin, Experiments on harmonic generation in grainy media, Acoust. Res. Lett. 15 (1992) 221–224.

[58] I.Y. Belyaeva, V.Y. Zaitsev, E.M. Timanin, Experimental Study of Nonlinear Elastic Properties of Grainy media with Nonideal Packing, Acoust. Phys. 40 (1994) 789–793.

[59] D. Sun, C. Daraio, S. Sen, Nonlinear repulsive force between two solids with axial symmetry, 066605 (2011) 1–5. doi:10.1103/PhysRevE.83.066605.

[60] J. Sabot, P. Krempf, C. Janolin, Non-linear vibrations of a sphere-plane contact excited by a normal load, J. Sound Vib. 214 (1998) 359–375. doi:10.1006/jsvi.1998.1582.

[61] E. Rigaud, J. Perret-Liaudet, Experiments and numerical results on non-linear vibrations of an impacting Hertzian contact. Part 1: Harmonic excitation, J. Sound Vib. 265 (2003) 289–307. doi:10.1016/S0022-460X(02)01262-2.

[62] D. Kook, J. Choi, J. Kim, Y. Kim, Review of spent fuel integrity evaluation for dry storage, Nucl. Eng. Technol. 45 (2013) 115–124. doi:10.5516/NET.06.2012.016.

[63] W.C. Bare, L.D. Torgerson, Dry Cask Storage Characterization CASTOR V / 21 Cask Opening and Examination, (2001) 1–68.

[64] J.D. Lambert, S. Bakhtiari, I. Bodnar, C. Kot, J. Pence, NRC Job Code V6060: Extended In-Situ and Real Time Monitoring Task 3: Long-Term Dry Cask Storage of Spent Nuclear Fuel, U.S. Nuclear Regulatory Commission, 2012.

[65] R.M. Meyer, A.F. Pardini, J.M. Cuta, H.E. Adkins, A.M. Casella, A. Qiao, M. Larche, A.A. Diaz, S.R. Doctor, NDE to Manage Atmospheric SCC in Canisters for Dry Storage of Spent Fuel: An Assessment, 2013.

[66] R.M. Meyer, A.F. Pardini, B.D. Hanson, Review of NDE Methods for Detection and Monitoring of Atmospheric SCC in Welded Canisters for the Storage of Used Nuclear Fuel Prepared for, (2013).

[67] G. Kim, S. Park, J. Kim, K.E. Kurtis, N.W. Hayes, L.J. Jacobs, Nonlinear Rayleigh surface waves to characterize microscale damage due to alkali-silica reaction (ASR) in full-scale , nuclear concrete specimens, Constr. Build. Mater. 186 (2018) 1114–1118. doi:10.1016/j.conbuildmat.2018.08.022.

[68] K.H. Matlack, J.J. Wall, J.-Y. Kim, J. Qu, L.J. Jacobs, H.-W. Viehrig, Evaluation of radiation

damage using nonlinear ultrasound, J. Appl. Phys. 111 (2012) 054911. doi:10.1063/1.3692086.

[69] K.H. Matlack, J. Kim, J.J. Wall, J. Qu, L.J. Jacobs, M.A. Sokolov, Sensitivity of ultrasonic nonlinearity to irradiated , annealed , and re-irradiated microstructure changes in RPV steels, J. Nucl. Mater. 448 (2014) 26–32. doi:10.1016/j.jnucmat.2014.01.038.

[70] J.-I. Tani, M. Mayuzumi, N. Hara, Initiation and Propagation of Stress Corrosion Cracking of Stainless Steel Canister for Concrete Cask Storage of Spent Nuclear Fuel, CORROSION. 65 (2009) 187–194.

[71] S. Choi, H. Cho, C.J. Lissenden, Selection of Shear Horizontal Wave Transducers for Robotic Nondestructive Inspection in Harsh Environments, Sensors. 17 (2017). doi:10.3390/s17010005.

[72] C.J. Lissenden, S. Choi, H. Cho, A.T. Motta, K. Hartig, X. Xiao, S. Le Berre, S.N. Brennan, K.M. Reichard, R. Leary, B. McNelly, I. Jovanovic, Toward Robotic Inspection of Dry Storage Casks for Spent Nuclear Fuel, J. Press. Vessel Technol. Trans. ASME. 139 (2017). doi:10.1115/1.4035788.

[73] S. Choi, H. Cho, M.S. Lindsey, C.J. Lissenden, Electromagnetic Acoustic Transducers for Robotic Nondestructive Inspection in Harsh Environments, Sensors. 18 (2018) 1–13. doi:10.3390/s18010193.

[74] S. Choi, H. Cho, C.J. Lissenden, Nondestructive inspection of spent nuclear fuel storage canisters using shear horizontal guided waves, Nucl. Eng. Technol. 50 (2018) 890–898. doi:10.1016/j.net.2018.04.011.

[75] Z. Shayer, Z. Yu, D.L. Olson, S. Liu, S. Gordon, K.L. Murty, N. Kumar, D. Kaoumi, B. Anderson, M. Remillieus, T.J. Ulrich, C. Bryan, D. Enos, J.D. Almer, J.R. Johns, D. Lewis, Integrated Research Program Overview on the “Innovative Approaches to Marine Atmospheric Stress Corrosion Cracking Inspection, Evaluation And Modeling in Used-Fuel Dry Storage Canisters,” in: T. Ohji, J. Matyas, H. Colorado, R. Kanakala (Eds.), Adv. Mater. Sci. Environ. Energy Technol. VI, 2017. doi:doi:10.1002/9781119423799.ch15.

[76] M. Remillieux, P. Le Bas, L. Pieczonka, B.E. Anderson, Estimating the Penetration Depth and Orientation of Stress Corrosion Cracks Using Time-Reversal Acoustics, in: Trans. Am. Nucl. Soc., 2016: pp. 217–220.

[77] B.E. Anderson, L. Pieczonka, M.C. Remillieux, T.J. Ulrich, P.-Y. Le Bas, Stress corrosion crack depth investigation using the time reversed elastic nonlinearity diagnostic, J. Acoust. Soc.

Am. 141 (2017) 76–81. doi:10.1121/1.4974760.

[78] S.M. Hogg, B.E. Anderson, P. Le Bas, M.C. Remillieux, Nonlinear resonant ultrasound spectroscopy of stress corrosion cracking in stainless steel rods, NDT&E Int. (2018). doi:10.1016/j.ndteint.2018.12.007.

[79] Y. Salchak, A. Bulavinov, R. Pinchuk, A. Lider, I. Bolotina, D. Sednev, Dry Storage Casks Monitoring by Means of Ultrasonic Tomography, Phys. Procedia. 70 (2015) 484–487. doi:10.1016/j.phpro.2015.08.291.

[80] S. Howden, B. Lin, L. Yu, V. Giurgiutiu, Acoustic emission and active sensing capabilities on full-scale nuclear dry cask storage structures, in: Proc. SPIE - Int. Soc. Opt. Eng., 2018.

[81] S. Chen, Vibration of Nuclear Fuel Bundles, Nucl. Eng. Des. 35 (1975) 399–422.

[82] V. Zeman, Z. Hlaváč, Mathematical modelling of friction-vibration interactions of nuclear fuel rods, Appl. Comput. Mech. 10 (2016) 57–70.

[83] H.S. Kang, K.N. Song, H.K. Kim, K.H. Yoon, Y.H. Jung, Verification test and model updating for a nuclear fuel rod with its supporting Structure, J. Korean Nucl. Soc. 33 (2001) 73–82.

[84] C.T. Olinger, D.N. Sinha, Acoustic techniques in nuclear safeguards, in: 17th Annu. ESARDA Symp. Safeguards Nucl. Mater. Manag., Aachen, Germany, 1995.

[85] C. Olinger, Acoustic resonance spectroscopy for safeguards, in: Trans. Am. Nucl. Soc., 1994.

[86] W. Ren, Structural damage identification using modal data. II: Test verification, J. Struct. Eng. 128 (2002) 96–104. http://link.aip.org/link/?JSENDH/128/96/1.

[87] D.B. Rigby, Evaluation of the Technical Basis for Extended Dry Storage and Transportation of Used Nuclear Fuel, 2010.

[88] J. Kessler, R.E. Einziger, Technical Bases for Extended Dry Storage of Spent Nuclear Fuel, Palo Alto, CA, 2002.

[89] K. Waldrop, Extended Storage Collaboration Program International Subcommittee Report, 2012.

[90] B. Hanson, H. Alsaed, C. Stockman, D. Enos, R. Meyer, K. Sorenson, Gap Analysis to Support Extended Storage of Used Nuclear Fuel, U.S. Department of Energy, 2013. http://energy.gov/ne/downloads/gap-analysis-support-extended-storage-used-nuclear-fuel-0%5Cnhttp://energy.gov/sites/prod/files/Gap Analysis Rev 0 Final.pdf.

[91] R. Benke, H. Jung, A. Ghosh, Y. Pan, J.C. Tait, Potential Releases inside a Spent Nuclear Fuel Dry Storage Cask due to Impacts: Relevant Information and Data Needs, 2012.

[92] T.Y. Wu, H.Y. Lee, L.C. Kang, Dynamic response analysis of a spent-fuel dry storage cask under vertical drop accident, Ann. Nucl. Energy. 42 (2012) 18–29. doi:10.1016/j.anucene.2011.12.016.

[93] T. Saegusa, K. Shirai, T. Arai, J. Tani, H. Takeda, M. Wataru, A. Sasahara, P.L. Winston, I.S. Agency, Review and Future Issues on Spent Nuclear, Nucl. Eng. Technol. 42 (2012) 237–248.

[94] K.J. Connolly, R.B. Pope, A Historical Review of the Safe Transport of Spent Nuclear Fuel, 2016.

[95] C.H. Yang, M.F. Huang, Non-Destructive Characterization of Hydrogen Concentration in Zircalloy, Key Eng. Mater. 270–273 (2004) 89–95. doi:10.4028/www.scientific.net/kem.270-273.89.

[96] M. Nakatsuka, S. Ishimoto, Y. Ishii, A. Miyazaki, A new non-destructive technique for hydrogen level assessment in zirconium alloys using EMAR method, J. Nucl. Sci. Technol. 43 (2006) 1142–1148. doi:10.1080/18811248.2006.9711206.

[97] S.A. Nikulin, V.G. Khanzhin, A.B. Rojnov, Application of an Acoustic Emission Method for SCC Testing of Zirconium Cladding Tubes, in: Corros. 2002, NACE International, 2002. https://www.onepetro.org/conference-paper/NACE-02437.

[98] H.A.H. Al-khazali, M.R. Askari, Geometrical and Graphical Representations Analysis of Lissajous Figures in Rotor Dynamic System, IOSR J. Eng. 2 (2012) 971–978.

[99] D.P. Hess, Normal Vibrations and Friction at a Hertzian Contact under Random Excitation: Theory and Experiments, J. Sound Vib. 153 (1992) 491–508.

[100] K.Y. Lin, J. Mobley, W.E. Prather, Z. Lu, G. Priyadarshan, J.R. Gladden, Vibrational modes for the internal characterization of a full- scale Transnuclear-32 dry storage cask for spent nuclear fuel assemblies, J. Sound Vib. 460 (2019) 114881. doi:10.1016/j.jsv.2019.114881.

VITA

Kevin Yi-Wei Lin

EDUCATION

- University of Mississippi (UM), Oxford, MS, US — Aug 2015 – May 2020
  National Center for Physical Acoustics (NCPA)
  Doctor of Philosophy, Physics (Advisor: Dr. Joel Mobley)
- National Taiwan University, Taipei, Taiwan — Sep 2009 – June 2013
  Bachelor of Science, Physics

ACADEMIC EXPERIENCE

Graduate Research Assistant at the NCPA, MS, US — Dec 2015 – Present

- Characterization of Contact Loss with Nonlinear Acoustic Resonance Spectroscopy
  - Successfully identified the total mass of spheres inside a cylindrical container with external sensors and modeled the contact nonlinearity with Finite Element Analysis (FEA).
- Damping of Helical Antenna of Low Earth Orbiting Satellite (DoD)
  - Propose a novel damping mechanism and study it on FEA and a scaled down lab model.
  - In charge of setting up an Unclassified Controlled Information working environment.
- Hostile Fire detection with Deployable Acoustic Sensors on Drones (Army)
  - Integrate a data collection system plus a camera on a drone for real-time gunshot detection.
- Femur Implant Removal Using Acoustics Methods (UM Medical Center)
  - Resonance and surface wave methods with FE simulations and lab experiments.
- Passive Acoustic Technique for Detecting, Locating, and Characterizing Hydrocarbon Leakages
  - Developed a LabVIEW program to control syringe pump integrated with hydrophone data acquisition.
- Optical Guidance and Suppression of Acoustic Signals in Air (ARL)
  - Performed FEA to investigate laser-heated air layers as an acoustic waveguide and

reflection barrier.

- Multimodal Nondestructive Dry Cask Basket Structure and Spent Fuel Evaluation (DOE)
  - Developed a method to detect failure in 1 of 32 spent fuel assemblies inside a lab-scale nuclear cask based on measurements and FEA from a full-scale one.

Teaching Assistant at the Department of Physics and Astronomy at UM 2015 – 2016 & Fall 2018

- Laboratory for Science and Engineering (Phys221, 222)

Undergraduate Research Assistant Jul 2012 – Jun 2013

Bio-Polymer Laboratory, Institute of Physics, Academia Sinica, Taipei, Taiwan.

(Advisor: Dr. Wen-Tau Juan)

- Anisotropic Spreading of DNA on a Supported Cationic Lipid Membrane
  - Plasmid DNA serves as a probe and an indicator of heterogeneity on the 2D cationic supported membrane and the spatial series relation between plasmid and the spreading of lambda DNA is investigated. Preliminarily showed the spreading is correlated with the heterogeneity.

PUBLICATIONS

K. Y. Lin, W. E. Prather and J. Mobley (in preparation). Characterization of Sphere-Plane Contact Loss Nonlinearity inside a Cylindrical Container Using Nonlinear Acoustic Resonance Spectroscopy

K. Y. Lin, J. Mobley, W. E. Prather, Z. Lu, G. Priyadarshan and J. R. Gladden (under review). Vibrational Metrics for the Evaluation of Internal Conditions in a Scaled Nuclear Dry Storage Cask. Applied Acoustics

K. Y. Lin, J. Mobley, W. E. Prather, Z. Lu, G. Priyadarshan and J. R. Gladden. Vibrational modes for the internal characterization of a full-scale Transnuclear-32 dry storage cask for spent nuclear fuel assemblies. Journal of Sound and Vibration, 460 (2019), 114881, https://doi.org/10.1016/j.jsv.2019.114881

J. R. Gladden, J. Tulenko, L. Yu and H. Yang. Multimodal Nondestructive Dry Cask Basket Structure and Spent Fuel Evaluation. United States, 2018, https://doi:10.2172/1492003. (K. Y. Lin prepared the UM part of this NEUP-IRP final report)

K. Y. Lin, W. E. Prather, J. Mobley, Z. Lu, G. Priyadarshan and J. R. Gladden. Vibrometric characterization of an unloaded full-scale TN-32 dry storage cask for spent nuclear fuel. Proceedings of Meetings on Acoustics, 31(1), 2017, https://doi.org/10.1121/2.0000678

K. Y. Lin, W. E. Prather, J. Mobley, Z. Lu, G. Priyadarshan and J. R. Gladden. Vibrometric characterization of an intact and unloaded scaled model TN-32 dry storage cask for spent nuclear fuel, Proceedings of Meetings on Acoustics, 31(1), 2017 https://doi.org/10.1121/2.0000754

SELECTED PRESENTATIONS

K. Y. Lin, J. Mobley, W. E. Prather, Z. Lu, G. Priyadarshan and J. R. Gladden. Development of vibrational metrics for internal damage scenarios of a scaled Transnuclear-32 dry storage cask for spent nuclear fuel. 177th Meeting of the Acoustical Society of America in Louisville, Kentucky, May 2019

K. Y. Lin. Examination of spent nuclear fuels inside dry storage casks. Three Minute Thesis Competition at the University of Mississippi (Final Round), Oct 2018

K. Y. Lin, W. E. Prather, J. Mobley, Z. Lu, G. Priyadarshan and J. R. Gladden. Vibrometric characterization of a full-scaled and a scaled model TN-32 dry storage cask for spent nuclear fuel. The Mississippi Academy of Sciences 82nd Annual Meeting, U. of Southern Mississippi, Hattiesburg, MS, Feb 2018

K. Y. Lin, W. E. Prather, J. Mobley, Z. Lu, G. Priyadarshan and J. R. Gladden. Vibrometric characterization of a TN-32 dry storage cask for spent nuclear fuel. 171st Meeting of the Acoustical Society of America, New Orleans, Louisiana, Dec 2017

K. Y. Lin, W. E. Prather, J. Mobley, Z. Lu, G. Priyadarshan and J. R. Gladden. The determination of mode shapes of a scaled model TN-32 spent nuclear fuel dry storage cask. 171st Meeting of the Acoustical Society of America, New Orleans, Louisiana, Dec 2017

HONORS AND AWARDS

- Graduate Student Achievement Award
- UM 9th Research Symposium: 1st place
- 4th UM-MSU Physics Symposium: Best talk
- Jazz Alumni Endowment Scholarship
- 2019-20 Who's Who at UM
- 3-min Thesis Competition at UM - final round
- Honors Fellowship

LEADERSHIP AND SERVICES

- VP of UM Physics Graduate Student Assoc.
- Student tour guide for NCPA
- Various physics outreach event
- President of UM Taiwanese Student Assoc.